Micro-Structure and Molecular-Vibration Analysis of Paramylon and Paramylon Ester by Terahertz (THz) Spectroscopy

February 2020

Junlan Zhong

Micro-Structure and Molecular-Vibration Analysis of Paramylon and Paramylon Ester by Terahertz (THz) Spectroscopy

A Dissertation Submitted to
the Graduate School of Life and Environmental Sciences,
the University of Tsukuba
in Partial Fulfillment of the Requirements
for the Degree of Doctor of Philosophy in Environmental Studies
(Doctoral Program in Sustainable Environmental Studies)

Junlan Zhong

Abstract

The *terahertz* (THz) radiation consists of electromagnetic waves with frequencies in the range of approximately 0.1-10 THz (1 THz = 10^{12} Hz, corresponding wavelengths from 30 μm-3 mm), which lies between microwave and infrared light. It is widely known that the THz spectroscopy involves the uniquely rotational and vibrational modes of the intermolecular bonding and the hydrogen-bonding networks, which provide us with valuable information on the molecular structures and functions in the materials, especially the hydrogen-bonding network is ubiquitous in polysaccharide compounds.

In this thesis, several glucose polymers, including cellulose, sodium carboxymethyl starch (CM-starch), paramylons and paramylon esters have been focused on studying using Fourier-Transform InfraRed-THz (FT-IR-THz) spectroscopy and THz Time-Domain spectroscopy (THz-TDS). The main contents and innovations of this study are as follows:

(1) The low-frequency optical spectra of paramylons and paramylon esters were measured by FT-IR-THz spectroscopy in the range of 0.3-8 THz for the first time. The spectral features of glucose and cellulose also measured and compared with those of paramylon and paramylon ester. The results show the characteristic fingerprint absorption peaks existing both in paramylon and paramylon esters. The spectrum of paramylon shows broad peaks around 4, 6, and 8 THz and a shoulder-like peak around 2 THz, while the spectrum of paramylon ester shows two broad peaks at 2.7 and 5.0 THz. The peaks observed in paramylon ester are speculated to be caused by the redshift of peaks of 4 and 6 THz observed in paramylon. The characteristic absorption features of paramylon and paramylon ester in the THz region are observed for the first time, which provides with the spectral fingerprint to identify the paramylon and paramylon ester from other saccharides.

(2) The particular absorption features of paramylons with different molecular weights (MW) and paramylon esters with different degrees of substitution (DS) were compared and analyzed. All paramylons have a broad absorption peak at around 4 and 6 THz, demonstrating that the absorption is independent of the size of the polymer molecules. Therefore, we conclude that the absorption features may be originated from a typical characteristic feature of paramylon, such as vibration modes originated from hydrogen bonding modes of -OH group. The paramylon esters show similar broad spectral features around 2.5 and 5 THz. The linear relationship between the

peak intensities and DS was found with reasonable accuracy. The DS-intensity change of the peak also demonstrated that the peak at 2.7 is partially relative to the vibrational modes of sidechains, and the peak around 5 THz is partially attributed to the networks of hydrate bondings.

(3) The temperature-dependent THz spectroscopy is also performed on cellulose, paramylon, paramylon ester and CM-starch to analyze the vibrational density of states (VDOS) and the boson peak (BP) is determined. The complex dielectric constants ($\varepsilon(\nu) = \varepsilon'(\nu)+\varepsilon''(\nu)$) observed below 2 THz frequency were analyzed. For cellulose, paramylon, and CM-starch, the values of both the real part $\varepsilon'(\nu)$ and imaginary part $\varepsilon''(\nu)$ of the ε decrease with the decrease temperature. The behavior is attributed to the redshift of vibration frequency of the excess wing owing to the freezing of fast relaxation modes in the low temperatures, which exists in the THz region. The complex dielectric constant of paramylon ester is very different from others. The value of $\varepsilon'(\nu)$ of paramylon ester increases as the temperature decreases. The origin of the behavior mainly can be attributed to the blueshift of the VDOS peak toward low temperature observed in the $\varepsilon''(\nu)$ spectrum, where a clear broad peak is observed around 2 THz. Comparing the spectra of starch and CM-starch, and paramylon and paramylon ester, we concluded that the substitution of -OH groups causes a significant difference in the shapes and values to the real part of the complex dielectric constant.

(4) The BP behaviors of the mentioned above glucose polymers were compared and discussed with the $\alpha(\nu)/\nu^2$ spectra. Cellulose, CM-starch and paramylon ester show BP at 0.92, 1.16, and 0.75 THz, respectively. As the temperature increased, the shape of the boson peak became broader. This phenomenon is in good agreement with the change in the spectra of complex dielectric constant, which are caused by the excess wing vibration of the fast relaxation mode seen in the THz region. There is no peak observed in the $\alpha(\nu)/\nu^2$ spectrum of paramylon because paramylon had a high degree of crystallinity. We also compared those BPs to the BPs of glucose and starch which were studied in the previous studies, and we conclude that the hydrogen bond network may be the dominant factor of BP frequency in glucose and glucose polymer glasses. On the other hand, in paramylon ester, the disappearance of -OH groups may reduce the BP frequency, where the weak van der Waals force may be responsible for the observed BP frequency.

Key words： Glucose polymers, Paramylon, Paramylon-ester, Terahertz spectroscopy, Far-infrared spectroscopy, Boson peak.

Acknowledgment

First of all, I would like to express my sincere gratitude to my academic supervisor, Prof. Kazuo Kadowaki, for his valuable advice and discussion through this research, for his helpful comments on the draft of this dissertation.

I would also like to express my sincere gratitude to my supervisor, Prof. Iwane Suzuki, for his advice, patience, and support throughout this study. I am proud of having worked on this dissertation under his guidance.

I would also like to express my gratitude to the cooperative partner, Assistant Prof. Tatsuya Mori, for instructing in preparation and characterization for glass samples, and his helpful comments on the draft of the published papers.

I would also like to extend my gratitude to the reviewers of this thesis, Prof. Kazuo Kadowaki, Prof. Iwane Suzuki, Prof. Zhenya Zhang, Prof. Maki Tsujimura, and Assistant Professor Tatsuya Mori, for their constructive comments to this thesis.

I would also like to express my sincere gratitude to Prof. Makoto M. Watanabe and Dr. Masatoshi Iji for allowing me to work in the Algae Biomass Energy System (ABES) Research center.

The experiments in this thesis were performed with the constructive help of many people. Without their cooperation, this thesis would not be completed. I would like to show my gratitude to Assistant Prof. Takanari Kashiwagi, Assistant Prof. Hidotoshi Minami, Assistant Prof. Goto Hiromasa and Assistant Prof. Manabu Tsujimoto for FTIR experiments; Dr. Midori Yamashiro, Dr. Teruhiko Tanaka for sample support, Mr. Leona Motoji and Ms. Wakana Terao for low-temperature THz-TDS measurement, Dr. Andreas Isdepsky for algea growth and extraction of oil, *etc*.

I would like to show my gratitude to the laboratory members, Mr. Shin Nakagawa, Mr. Kim Jeonghyuk, Mr. Yu Duan, Mr. Zhitai Huang, Ms. Ono Yukino, Mr. Imai Takayuki, Mr. Shinji Kusunose, Mr. Yuki Tanabe, and Mr. Takumi Yuasa.

I would also like to express my sincere gratitude to my family, Tianjun Zhong, Chunjuan

Liu and Ping Zhong, for their moral support and warm encouragement.

Finally, I would like to appreciate the Chain Scholarship Council (CSC) for financial support.

Content

Chapter 1 Introduction

1.1. General description of Microalgae

(From Chapter 1 of *Phycology*, Fourth Edition, Robert Edward Lee)

Microalgae are photosynthetic microorganisms, mainly living in freshwater, seawater, or brackish water. Microalgae have a single cell or simple multicellular structure, and they can grow fast and survive even under harsh conditions. Therefore, microalgae exist almost all over the world (Khan et al., 2018; Lee, 2018). There are about 500,000 species of microalgae in the world, far more than terrestrial plant species, but only 300,000 of them have been studied (Guiry, 2012). The classification of microalgae relies on pigmentation, life cycle, or basic cellular structure. According to the pigmentation, microalgae can be classified into three groups: Rhodophyta (red algae), Phaeophyta (brown algae), and Chlorophyta (green algae) (Khan et al., 2018).

1.2 Cell structure

Most cells in microalgae are eukaryotic cells expect cyanobacteria. A eukaryotic cell is surrounded by a cell wall composed of polysaccharides (Lee, 2018). Figure 1-1 shows the typical eukaryotic cell structure of the microalgae of *Chlamydomonas*. As shown in the figure, the visible nucleus is located in the center of the cell responsible for reproduction. Other cell organelles, including endoplasmic reticulum, Golgi, mitochondria, and lysosomes, are well developed in the endoplasmic reticulum system, performing specific functions separately. Photosynthesis and oxidative phosphorylation are carried out by chloroplasts and mitochondria, respectively.

1.3 Photosynthesis

Microalgae can convert solar energy into chemical energy through photosynthesis and store the chemical energy in cells as biomass. Photosynthesis is a process of carbon fixation by absorbing light energy and converting the light energy into chemical energy as sugars. This process can be expressed by the following chemical relation:

$$CO_2 + H_2O + \text{photons} \rightarrow [CH_2O] + O_2. \quad (1\text{-}1\text{-}1)$$

Figure 1-2 shows the overview of the photosynthesis process, including two reactions: the light-dependent pathway and the light-independent pathway (the Calvin cycle). In the light-dependent pathway, showing in the left part of Figure 1-2, light energy is absorbed

by green chlorophyll pigments and used to produce adenosine triphosphate (ATP) and nicotinamide adenine dinucleotide phosphate (NADPH). At the same time, the O_2 is released in this process. In the Calvin cycle, CO_2 is captured by ribulose bisphosphate (RuBP). With the help of ATP and NADPH, the carbon in CO2 is fixed in the form of sugar.

1.3.1 Nutrition

Microalgae are photosynthetic organisms, and the growth requirements are relatively simple. The primary nutritions necessary for almost all the microalgae culture are CO_2, light, and water. Some essential nutrients like nitrogen, phosphorus, magnesium, and other metal irons are varying with the microalgae specials (Khan et al., 2018; Guiry, 2012; Chisti, 2007).

Water: In the case of open pond culture microalgae, to obtain 1 ton (t) of microalgae dry biomass, about 2000-3000 t water is necessary, and more than 1000 t is required for a water-recyclable system (Lee & Choi, et al., 2018). Therefore, low-cost water resources and water recycling are issues that must be addressed in the commercialization of microalgae products.

Carbon: More than 60% of the total nutrient cost for algae cultivation is paid on carbon sources. To producing 100 t of algal biomass, about 183 t of carbon dioxide will be fixed (Chisti, 2007). The most widely used carbon sources include: (i) CO_2 in the atmosphere; (ii) CO_2 derived from industrial waste gases (e.g., flue gas and combustion gases); and (iii) chemically fixed CO_2 in the form of soluble carbonates (Markou et al., 2014). The CO_2 absorption speed of microalgae is 10-50 times faster than that of terrestrial plants, and increasing CO_2 intensive culture can increase the yield. In the environment with a high concentration of CO_2 (12%), the well tolerates chlorella has the maximum growth rate and biomass yield of 0.267 /d and 0.087 g/L/d, respectively (Cho et al, 2016). In 2010, Ho *et al.* isolated 22 strains of *Scenedesmus obliquus* CNW-N and found the two plants had a higher growth rate up to 390.2 mg/L/d at a concentration of 20% CO_2 (Ho et al., 2010).

Light: In the photosynthetic process, to fix a CO_2 molecule requires 8 photons of photosynthetically active radiation (Amaro et al., 2011). The growth of microalgae is related to the efficiency of light utilization. Darzin and his coworkers have reported that the minimum amount of radiation for microalgal cultivation is 1500 $kWh \cdot m^2 \cdot yr^{-1}$ (2010). The amount of light absorption depends on many factors, including the specific location,

concentration, and pigment of the cells in the bioreactor at a particular time. The condition of light intensity on the growth of microalgae can be divided into light limitation, light saturation, and light suppression (Chisti, 2007). Although the degree of light intensity affecting the growth of microalgae varies from species to species, the growth rate of microalgae increases with increasing light intensity before reaching light saturation.

Other nutrients: Nitrogen (N) and phosphorus (P) are essential nutrients for microalgae culture. The required amount can be calculated by the approximate molecular formula of the microalgal biomass, $CO_{0.48}H_{1.83}N_{0.11}P_{0.01}$(Chisti, 2007). Nitrogen is directly related to the primary metabolism of microalgae because it is a significant component of nucleic acids and proteins. Microalgae can use nitric acid, urea, ammonia, and organic matter as nitrogen sources. Phosphorus is usually supplied in the form of phosphate, but microalgae can also utilize organic or inorganic forms of phosphorus by self-absorption or intracellular phosphatases (Markou et al., 2014). When the intracellular phosphate content is excessive, the microalgae can store the diacid salt in the form of polyphosphate. During the cultivation process, when the phosphorus source in the medium is sufficient, the microalgae preferentially use the phosphorus in the medium instead of using the phosphorus stored in the medium; when the medium has less pity or phosphorus deficiency stress, the microalgae starts to use the storage. In addition to N and P, microalgae also need trace elements such as metal ions (sodium, magnesium, calcium, manganese, zinc, copper, iron, molybdenum) and vitamins to achieve adequate growth (Markou et al., 2014).

1.3.2 Large-scale culture of microalgae

In order to increase the potential gains of microalgae with the minimimum expense, the cultivation environment is vital, such as pH, temperature, agitation, and daylight hours (Chacón-Lee & González-Mariño, 2010). Therefore, a suitable cultivation system is a crucial determinant to make full use of sunlight and nutritions. At present, two methods are practicable in the large-scale culture of microalgae, including the raceway pond system and closed photobioreactor, as described follows.

(1) Open raceway pond

Raceway ponds are growth in the open air and are the most common methods of large-scale cultivation of microalgae. The structure and the photo of a typical system are shown in Figure 1-3 and Figure 1-4. The actual land area is about 1000-440,000 m^2 (Spolaore et al., 2006), and there are usually a large number of power plants or heavy industries that emit CO_2. Microalgae absorb nitrogen from the atmosphere in the form of NO_X. In order to make the microalgae in contact with sunlight, the optimal liquid pool depth is 15-50

cm. The structure is simple, the construction cost is low, and the operation is simple. However, there are several disadvantages to the open raceway pond. For example, bacterias and other microalgae easily invade the culture, and the water is natural to evaporate. Also, because the temperature is not easy to control due to seasonal changes, and the efficiency of the utilization of light energy and CO_2 is lower than that of photobioreactors, leading to lower biomass productivity of open pond system than that of photobioreactors (Chisti, 2007).

(2) Closed photobioreactor

The system overcomes some of the significant constraints of the open pond system, enabling microalgae to grow in a restricted environment (pH value, light intensity, temperature, CO_2 concentration) to obtain high biomass concentration and functional products, such as lipid, protein and carbohydrates. Also, the system is more suitable for sensitive strains that are not competitive and cannot grow in harsh environments. The basic structure and the photo of the closed photobioreactor are shown in Figure 1-5 and Figure 1-6. Typically, the CO_2 is provided by a bubble tube with a diameter is 20 cm or less, and the light that improves the light utilization efficiency is adjusted by fluorescent lamps. Although the photobioreactor has many merits by comparison with open pond, the closed photobioreactor system has much higher costs, a more complicated structure, and a smaller illumination area than those of open raceway pond systems. In addition, as the cell density increases, the light transmittance is deteriorated, which affects the growth of microalgae (Singh & Sharma, 2012).

1.4 Advantageous features of microalgae

Microalgae have many beneficial features as a new biomass source:

(1) High photosynthetic efficiency and fast growth. The photosynthetic efficiency (PE) of microalgae is up to 9 %, which is much higher than that of most crops (only 0.5-1 %) (Redwood et al., 2012). Microalgae have no complicated reproductive organs, most of them reproduce by binary cell division, with a short cycle. Usually, microalgae cells can proliferate 1-4 times per day and can reach the exponential growth phase in a short time in which the biomass doubles every 3.5 hours (Chisti, 2007). Compared to traditional crops which can only harvest 1-2 times a year, the harvest cycle of microalgae is short. The continuous or semi-continuous cultures can achieve higher yields. For example, microalgae have a higher theoretical energy yield than terrestrial plants, which up to 77 g/biomass/m^2/day, which is about 280 tons/ha/year (Formighieri et al., 2012; Melis, 2009).

(2) Environmental friendly. Microalgae can fix carbon dioxide (CO_2) during

photosynthesis, which can achieve the dual purpose of CO_2 emission reduction and microalgae production (Khan et al., 2018; De Morais, & Costa, 2007). The potential capture efficiency of CO_2 in extensive microalgae culture system can be as high as 99% (Zeiler et al.,1995). Theoretically, for each 1kg microalgae biomass, 1.83 kg of CO_2 should be fixed to generate sugar (Chisti, 2007; Khan et al., 2018). Besides, the microalgae can absorb nitrogen and phosphorus and can grow in wastewater containing nutrients and metal ions (Rawat et al., 2011; Gonçalves et al., 2014). Therefore, microalgae can also play an essential role in wastewater treatment.

(3) Non-cultivable land and non-agricultural waters culture. According to reports, in order to meet the demand for biodiesel for transportation in the United States, it is necessary to use arable land to cultivate oil crops that exceed 50% of the total area of cultivated land, which will lead to a severe global food crisis. However, if the microalgae production of biodiesel requires only 7–13% of the total farmland (Odlare et al., 2011), they will not cause land tense and damage biodiversity. Microalgae do not require high water quality and can grow continuously in water with various salinities and chemical compositions. Therefore, it can maximize the use of marginal lands such as tidal flats, saline-alkali land, deserts, and mountainous hills to reduce the occupation of cultivated land. The scale cultivation of non-agricultural water, such as salty water and municipal engineering wastewater, can reduce the demand for freshwater. Therefore, it is a crucial way to obtain microalgae biological resources in the shortage of freshwater and cultivable land (Chisti, 2007).

(4) High productivity and multi-products. Microalgae are rich in various commercially valuable compounds such as polysaccharides, lipids, pigments, proteins, vitamins, and other bioactive compounds (Khan et al., 2018), leading microalgae have enormous economic potential in biofuels, biopharmaceutical, cosmetics, and bioplastic industries (Khan et al., 2018; Das et al., 2011), as shown in Figure 1-7. As reported, microalgae are capable of producing algal oil 58,700 L/ha, which can produce 121,104 L/ha biodiesels (Khan et al., 2018).

1.5 Microalga of *Euglena*

Euglena was first named by Christian G. Ehrenberg (1795-1876), and its characteristics were described before 1838. The word “Euglena” consists of two Greek words, “eu” and “glene.” The composition, meaning "good" and "eyeball," respectively, describing the photosensitive organ of eyespots are visible under the microscope. *Euglena* can grow in a wide range of pH values ranging from 3 to 9 of pH, especially, *Euglena* can survive under acidic conditions with a pH of 3.0 (Hargreaves et al., 1976), which can significantly

reduce pollution in open culture systems. Therefore, the growth of *Euglena* not only can produce biomass but also can purify water. The remained biomass is used as nutritional supplements in animal feed and as sources in aquaculture.
Euglena can feed it by photosynthesis (plant-like), when there is no light, they can survive even by heterotrophic metabolism (animal-like) (Inwongwan et al., 2019). All *Euglena* have two flagella located in a small cavity (reservoir) at the front end of the cell body. One flagellum is short, which cannot protrude beyond the cavity, while the other flagellum is very long, can be observed under the light microscope. In many species, the long flagellum plays a role in helping the cells move.

E*uglena gracilis* is mainly distributed in freshwater and is a highly adaptable organism that can survive under harsh environmental conditions, such as low pH, high salt, and high-energy radiation. E*uglena gracilis* has a long history as a biological research object since 1990 (Rosati et al., 1991). *Euglena gracilis* is a single-cell photosynthesis green algae. It is a spindle-to-needle shape with a length range of 20 to 100 μm (Schaechter, 2012), as shown in Figure 1-8, consisted of the photosynthesis of chloroplasts which giving them the ability to photoautotrophic and heterotrophic photosynthesis. The chloroplast of the *Euglena* contains chlorophyll a and chlorophyll b.
The E*uglena gracilis* cells are abundant in biologically active substances such as *β*-carotene, vitamin C, vitamin E, *β*-1,3-glucan, and polyunsaturated fatty acid (PUFA). Although Euglena is a photosynthetic organism, it does not produce a typical *α*-1,4/6-glucan, like starch. Conversely, when aerobic growth, it provides insoluble *β*-1,3-glucan (paramylon), with the weight ratio up to 25% of its dry cell weight (Marchessault & Deslandes, 1979). The E*uglena gracilis* consumes paramylon when the ambient carbon source is exhausted, as the same biological functions of starch. The paramylon has potential properties as an immunostimulant and an immunopotentiator. Its sulfated derivatives also exhibit anti-HIV activity and also have antioxidant effects. Paramylon also shows excellent potential in bioplastic industries.

1.6 Paramylon and paramylon ester

When *Euglena* is growing under heterotrophic growth conditions, a large amount of paramylon, which up to 25% of the total weight of the cell (Marchessault & Deslandes, 1979), will be accumulated. The first mention of this *β*-1,3-glucan by Gottlieb was in 1850 (Gottlieb). In the 1970s, the triple helix structure linking by *β*-1,3-glucosidic bonds were identified as the structural basis for paramylon by using X-ray diffraction spectroscopy (Marchessault & Deslandes, 1979). Paramylon is synthesized in pyrenoids

and stored throughout the cytoplasm, called paramylon bodies, which are often visible as colorless or white particles in light microscopy. Paramylon bodies are consisting of microfibers with a triple-helical structure and show different shapes, sizes, and locations in cells in different *Euglena* specials, as shown in Figure 1-9.

The structural investigations by X-ray diffraction and NMR spectrum revealed that paramylon has a triple helical structure with a hexagonal unit cell (showing in Figure 1-10) and has a very high level of crystallinity about 90% in the native state (Chuah et al., 1983; Kreger & Meeuse, 1952; Kiss et al., 1988). Such a helical structure makes paramylon a very tightly cell package, attractive thermal, and mechanical characteristics by comparing with other polymers. Paramylon has a molecular size of approximately 500 kDa (Barsanti et al., 2011). On the country, curdlan shows a much lower degree of crystallinity, with only 30-40%, even it shares a very similar structure with paramylon. The molecular weight of paramylon is about one-fifth of curdlan (Gan et al., 2019).

Generally, polysaccharides do not show good thermoplasticity, which is necessary for plastic manufacturers, because of their strong inter- and intra-molecular hydrogen bonding. Several kinds of research have demonstrated that polysaccharides can obtain the thermoplasticity by introducing long-chain acid into those polysaccharides (Peydecastaing et al., 2011; Gan et al., 2017). Therefore, before applying paramylon to plastic industries, the esterification is essential to get excellent thermoplastic properties. Derivatives based on paramylons has been proved to have characteristics of high thermal degradation temperature, excellent thermoplastics features, and transparency to visible light, high thermal stability (Gan et al., 2017). Gan et al. also demonstrated that the pure paramylon is a highly crystalline material and becomes amorphous material when suitable side alkyl chains are introduced into paramylon. This phenomenon is a point of departure for our investigation. A fundamental understanding of micro-structures of paramylons and paramylon esters with different degrees of esterification would lead to a better understanding of the properties which are significant for practical application in bio-plastics industries.

1.7 The main content of this work

In this work, cellulose, paramylons, and paramylon esters have been focused on studying the infrared and THz absorption properties using Fourier-transform infrared-THz (FT-IR-THz) spectroscopy. The spectral characteristics of paramylons with different molecular weight (MW) and paramylon-esters with different degrees of substitution (DS) were

studied by THz spectroscopy. The temperature-dependent THz spectroscopy is also performed on cellulose, CM-starch, paramylon, and paramylon ester to investigate the origin of boson peaks and the fractal dynamics. Lastly, the dominant factors that determined the BP frequency for said polymers also be discussed.

This thesis is organized as follows:

In chapter 1, the background and relationship of microalgae and bio-polymers will be presented, including the introduction of microalgae of *Euglena gracilis* and the synthesis process of paramylon in *Euglena gracilis*, the unique features of paramylon and paramylon ester, and development and the challenge to develop paramylon to commercial industry products. Lastly, the motivation and main content of my thesis will be introduced.

In chapter 2, the basic knowledge of crystalline and amorphous (glassy) materials is introduced. The concept of vibrational density of states and boson peak will be presented to analyze the theme-properties of carbohydrate polymers.

In chapter 3, the theory of electromagnetism, quantum mechanics, and solid-state physics related to terahertz science and technology are elaborated in detail. The technologies of THz generation and detection are introduced subsequently. The applications of THz spectroscopy are reviewed. Finally, the transmission terahertz time-domain spectroscopy and the extraction method of related material parameters are introduced.

Chapter 4 will outline the methodology used in this research. Necessary information about the sample preparation will be described first, including the algae culture, extraction of paramylon from *Euglena gracilis*, and the synthesis of the paramylon ester and CM-starch. Second, all the necessary steps used to THz spectroscopy measurement and analysis will be presented. Third, the details of the experimental setup and measurement parameters are presented.

In chapter 5, the THz spectra of paramylons, paramylon esters, cellulose with similar polysaccharides will be measured by Fourier-Transform InfraRed-THz (FT-IR-THz) spectroscopy in the range of 0.3-8 THz. The THz spectrum of glucose also measured and compared with the spectra of mentioned glucose polymers because glucose is the unit of these polysaccharides. The particular absorption features of paramylons with different molecular weight (MW) and paramylon esters with different degrees of substitution (DS)

will be compared and analyzed.

In chapter 6, Terahertz Time-Domain Spectroscopy (THz-TDS) is performed on cellulose, paramylon, CM-starch, and paramylon ester in the range of 0.2-4 THz to investigate the origin of boson peaks and fractal dynamics. The complex dielectric constants observed below 2 THz frequency are analyzed, and the BP behaviors are discussed.

Finally, in chapter 7, the conclusion of this thesis will be summarized, and further research and improvement of the THz spectroscopy analysis of polymers are discussed.

Figures

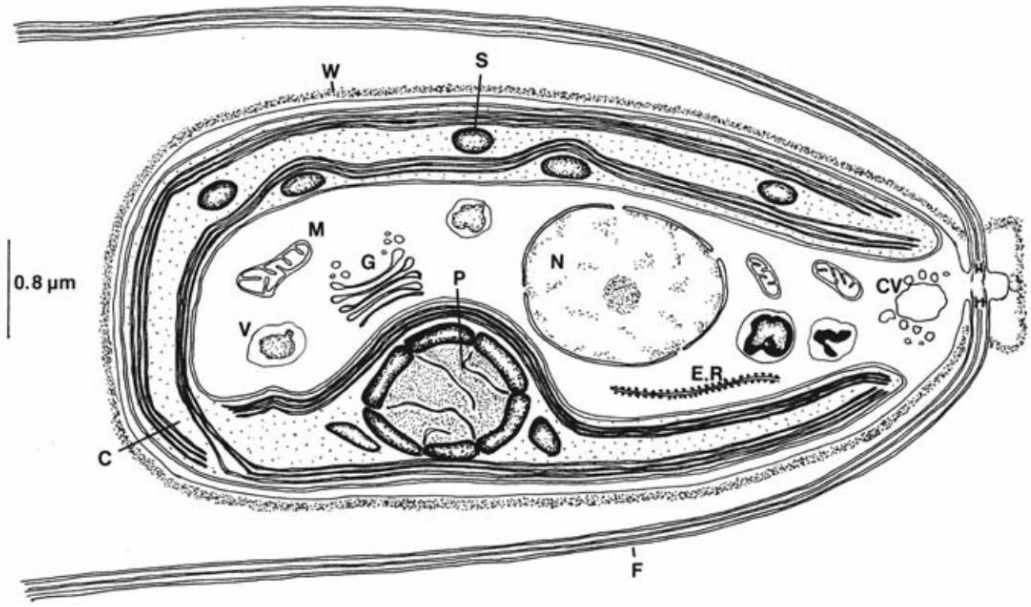

Figure 1-1 Eukaryotic cell structure of green alga Chlamydomonas. The main organelle includes (C) chloroplast; (CV) contractile vacuole; (E.R.) endoplasmic reticulum; (F) flagella; (G) Golgi body; (M) mitochondrion; (N) nucleus; (P) pyrenoid; (S) starch; (V) vacuole; (W) cell wall (Lee, 2018).

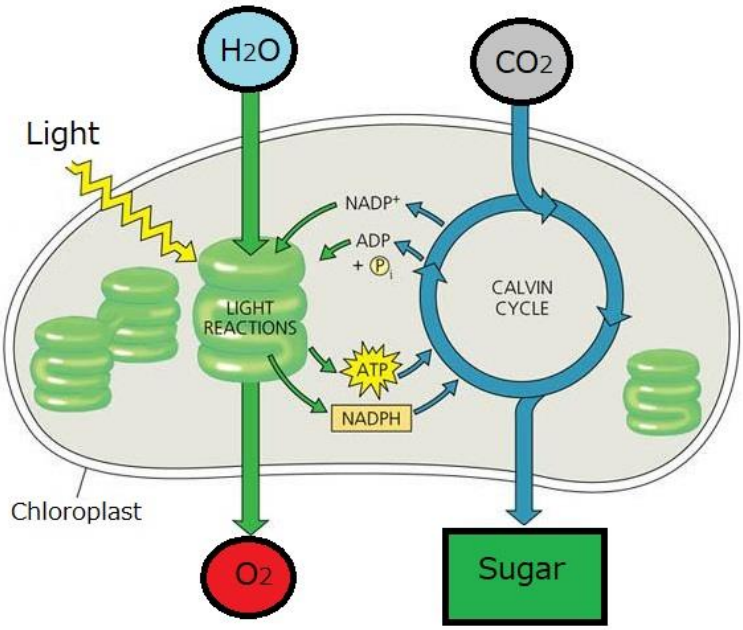

Figure 1-2 Outlook process of photosynthesis.

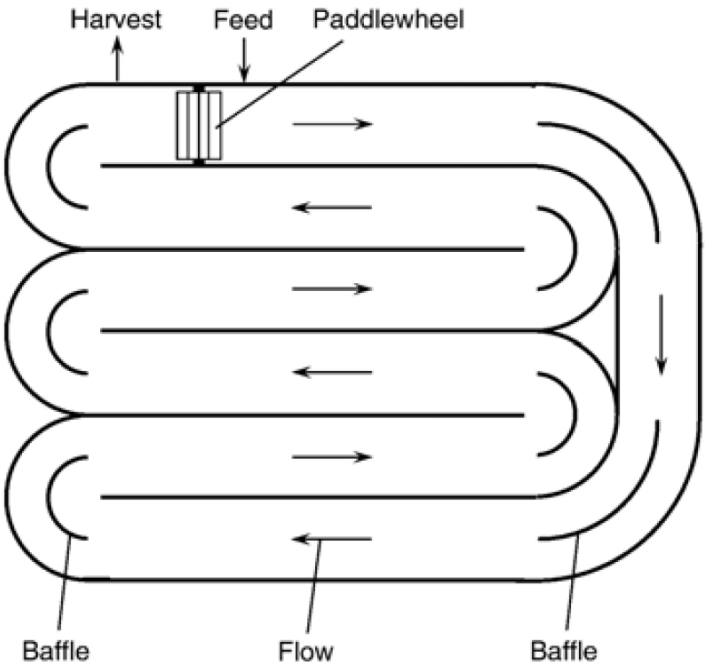

Figure 1-3 The structure of the raceway pond (Chisti, 2007).

Figure 1-4 The photo of the open raceway pond [Source： Algae biomass and Energy System R&D Center (ABES)].

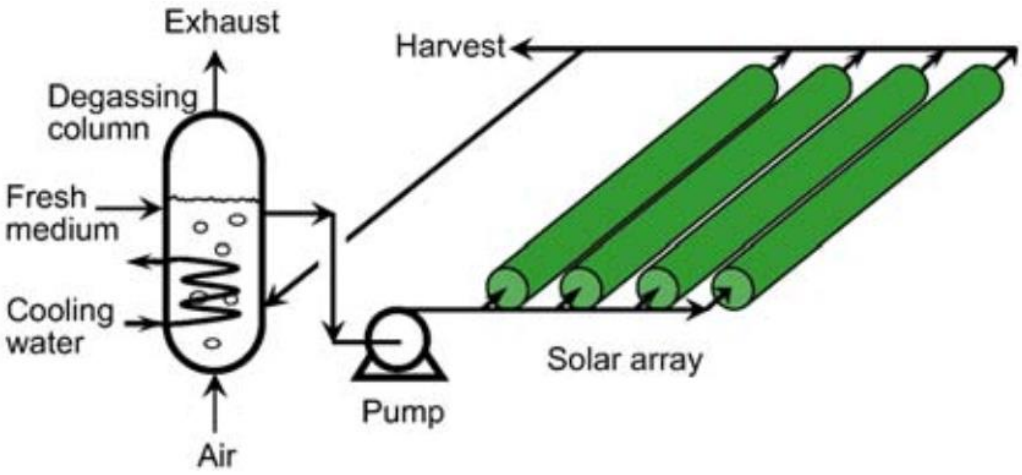

Figure 1-5 A tubular photobioreactor with parallel run horizontal tubes (Singh & Sharma, 2014).

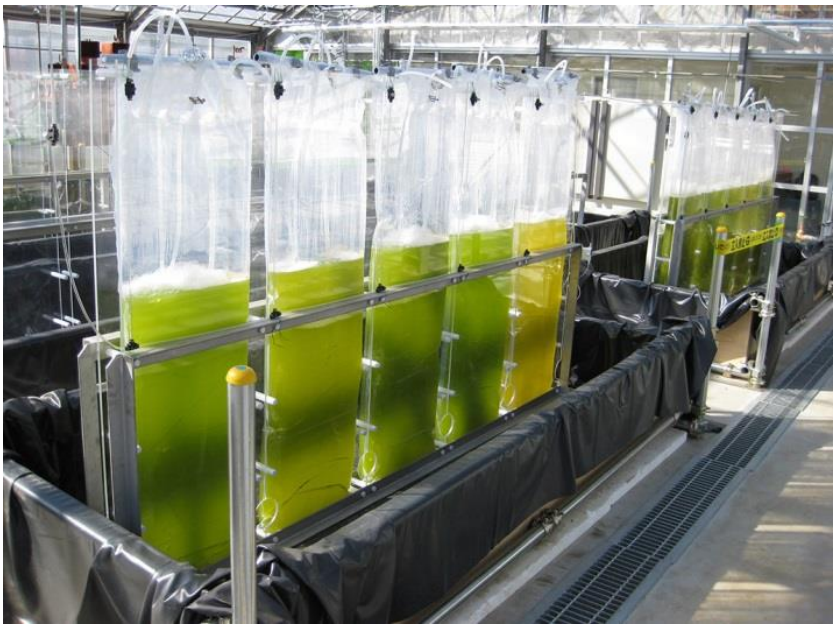

Figure 1-6 The photo of the closed photobioreactor [Source: Algae biomass and Energy System R&D Center (ABES)].

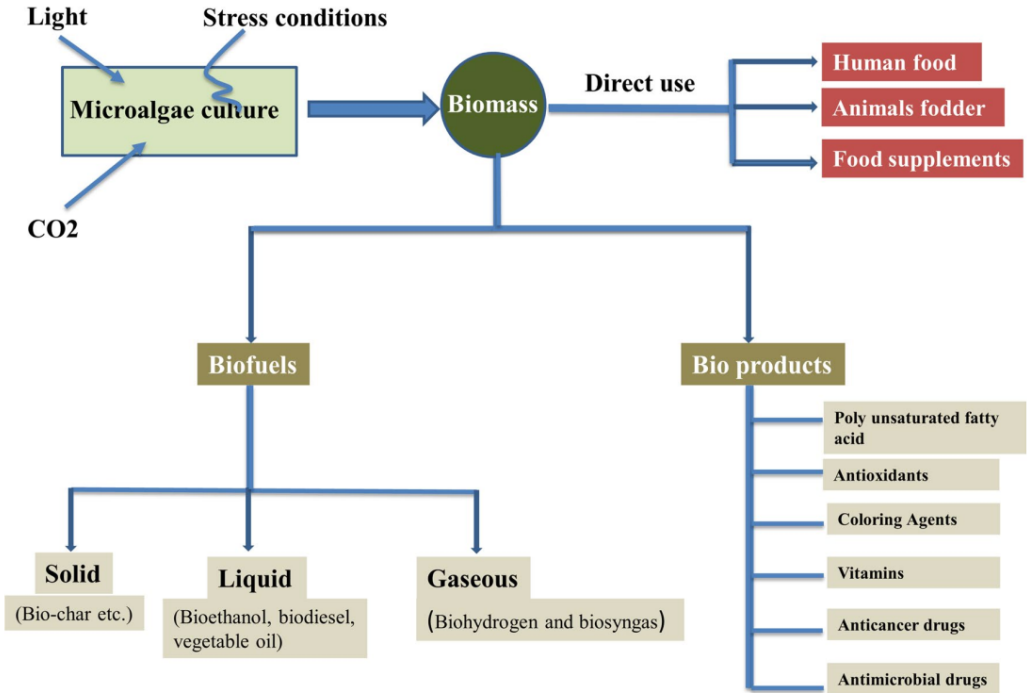

Figure 1-7 Multi-products of Microalgae (Khan et al., 2018).

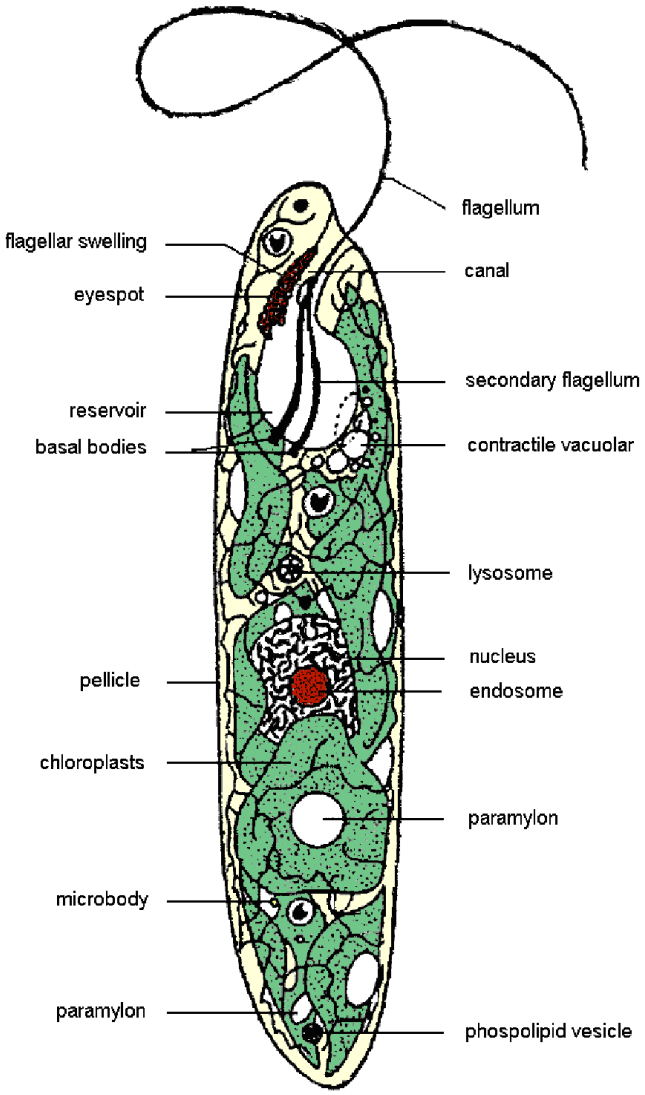

Figure 1-8 Typical morphology of *Euglena gracilis* (Van der Merwe, 2007).

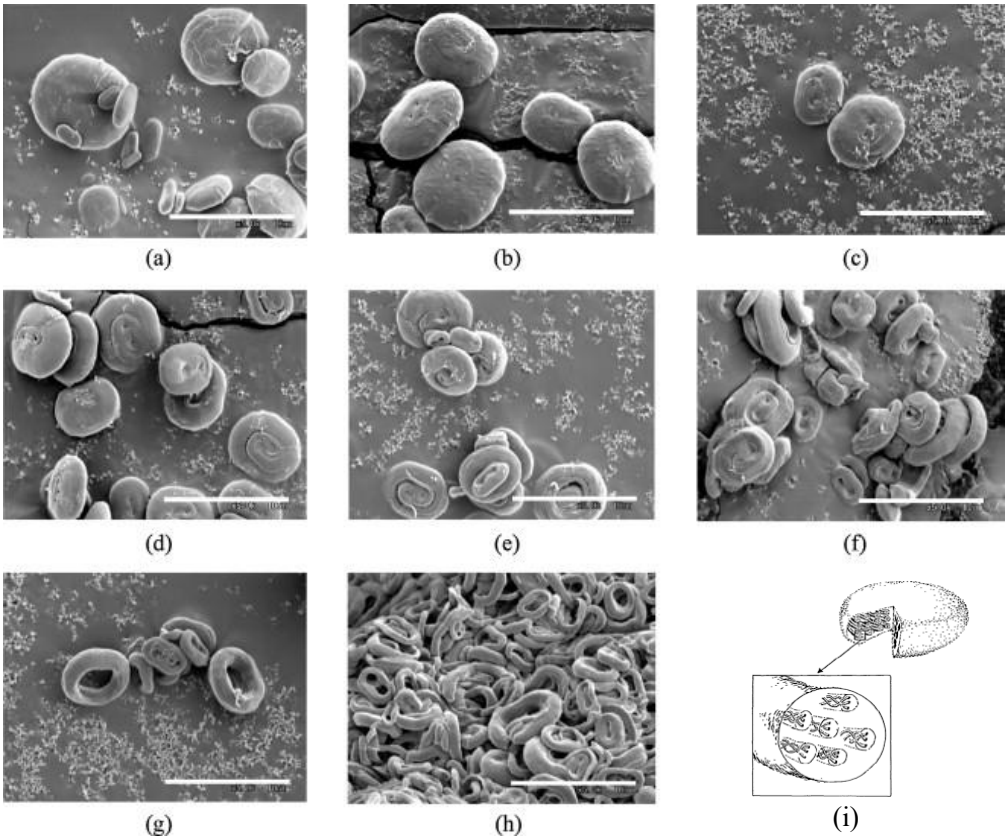

Figure 1-9 (a)-(h) Electron micrographs of paramylon body in different Microalgae (Shibakami et al., 2012). (i) Schematic representation of microfibrils of a paramylon body (Marchessault & Deslandes, 1979).

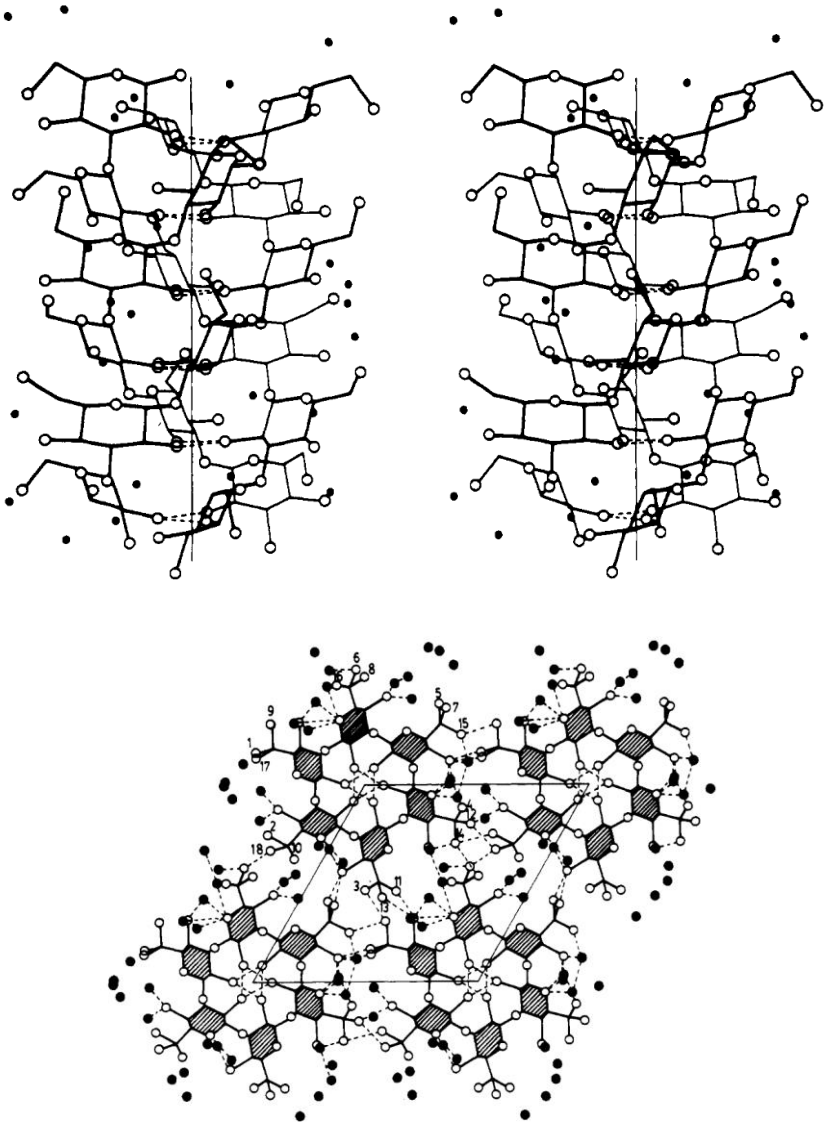

Figure 1-10 Top: stereoviews of the triplex. Bottom: projection of the crystal structure in the a-b plane. Hydrogen atoms are not shown, and water molecules are indicated by filled circles. Hydrogen bonds are drawn with dashed lines(Chuah et al., 1983).

Chapter 2 Crystals and Glassy systems

2.1 Crystal bonding

(From Chapter 3 of *Introduction to Solid State Physics*, Charles Kittel, 7th edition, 1976) Crystals hold atoms, molecules, ions, or assemblies with a periodic symmetry by interaction forces. The energy required to pull the atoms to the infinity distance is called the cohesive energy, which is mainly contributed by the attractive electrostatic interactions between the negative charges of electrons and the positive charges of nuclei. The cohesive energy in crystals ranges from 1 to 10 eV/atom, except inert gases with cohesive energy in the order of 0.1 eV/atom. The interaction forces between the atoms constituting the solid due to the van der Waals forces, ionic bonding force, covalent bonding force, and metallic bonding force. According to different combing forces, crystals can be classified into four types as follows:

2.1.1 Molecular crystals

Inert gases form the simplest crystals in the solid state, such as He, Ne, Ar, Kr and Xe (Kittel, 1976). The constituent atoms of these crystals have a very similar the electron distributions with the ones in free atoms. For inert gas atoms, the ionization energies are very high, and their outermost electron shell is completely filled, leading symmetric distribution of electron charges (Kittel, 1976). The cohesive energy of an atom in such a crystal is only one hundredth or less of the ionization energy of an electron in an atom. Therefore, the atom and the atom are combined into a crystal by a weak van der Waals force. The Van der Waals force is the force between the molecular dipole moments, and also includes the instantaneous dipole of the non-polar molecules and the force between the induced dipoles, also called the London interaction, or the induced dipole-dipole interaction. This force can be calculated by Equation (2-1-1):

$$\Delta U = -\hbar\omega_0 \cdot \frac{1}{8}\left(\frac{2e^2}{CR^3}\right)^2 = -\frac{A}{R^6}, \tag{2-1-1}$$

where R is the distance between two atoms, A (= $4\varepsilon\sigma^6$) is the force constant, ω_0 is the resonance frequency when the induction happened, σ and ϵ are parameters that related to the gas-phase state.

When the distance between two atoms is small, there is a repulsive force acting between

the two atoms. Combining this repulsive energy with van der Waals force, we can get an equation for the total potential energy—the Lennard-Jones potential.

$$U(R) = 4\epsilon\left[\left(\frac{\sigma}{R}\right)^{12} - \left(\frac{\sigma}{R}\right)^{6}\right] = \frac{B}{R^{12}} - \frac{A}{R^{6}}. \quad (2\text{-}1\text{-}2)$$

B (= $4\varepsilon\sigma^{12}$) is a positive constant. The relation between *Lennard-Jones potential* and distance of two atoms is showing in Figure 2-1.

The van der Waals is quite weak, leading the small binding energy. Therefore, the melting point of such molecular crystals is relatively low (Kr: 117 K; Ar: 84 K). They are soft, compressible, and non-conductive.

2.1.2 Ionic crystals

Ionic crystals are generally formed by the electrostatic interacting forces between atoms or molecules, which charge positively or negatively depending on the electronegativity. The electronegativity makes the outer valence electron of the small electronegative atom to a large electronegative atom, forming positive and negative ions. The total charge in the structural unit is zero, and no free electrons exist in ionic crystals, they are insulators. There are two typical structures: as for example, sodium chloride (NaCl) type (6 coordination) and cesium chloride (CsCl) type (8 coordination), as shown in Figure 2-2.

The main force combining the ion crystal is the electrostatic or Madelung energy. Assuming there are 2N atoms in the crystalline system, the total energy can be calculated by the following equation:

$$U_{tot} = -\frac{N\alpha q^2}{R_0}\left(1 - \frac{\rho}{R_0}\right), \quad (2\text{-}1\text{-}3)$$

where α is Madelung constant. The relationship between the total energy per molecule of ion crystal and internuclear distance is showing in Figure 2-3.

Due to the strong interaction between positive and negative ions in the ionic crystal, the binding energy of ionic crystals is generally considerable. Generally, ionic crystals have a high melting point, high strength and high hardness.

2.1.3 Covalent crystal

Covalent crystals are crystals formed by covalent bonding. The covalent bond is formed by electrons sharing two different atoms. Figure 2-4 shows the schemes of the covalent bond between two atoms sharing electrons with the wave function Ψ_1 of the atom 1 and

the wave function Ψ_2 of the atom 2, respectively. The combination of these two orbitals has two possibilities, one is the bonding orbital and another one is the antibonding orbital as showing in Figures 2-4(a) and 2-4(b):

$$\Psi_a = \Psi_1 + \Psi_2, \tag{2-1-4}$$

and

$$\Psi_b = \Psi_1 - \Psi_2. \tag{2-1-5}$$

These two orbitals have different energies, as shown in Figure 2-5.

Typical covalent bond crystals are, for example, Si, Ge, SiC, ZnS, *etc.* The covalent bond between atoms depends on the overlap of the adjacent atomic electron clouds (orbitals). The covalent bond between atoms has a specific directionality and saturation, which defines the orientation and coordination of the bonds between atoms. Covalent crystals are structurally stable, and the energy of the covalent bonding ranges from intermediate to high. Therefore, the melting point, hardness, and strength of covalent crystals range from intermediate to high. Because the bonding electrons are bound between the atoms and cannot move freely, the covalent bond crystals have poor conductivity.

2.1.4 Metal crystals

Metal crystals are formed by sharing outer electrons of the constituent atoms in a whole crystal. Therefore, these shared electrons can move around in a whole crystal as conduction electrons. This happens because the electronegativity of these constituent atoms is small. Therefore, they easily lose their valence electrons and leave positive-charged ions behind. These lost valence electrons become conduction electrons, which are shared by the whole metal and free to move in the crystal.

2.2 Thermal Properties of Crystals

Lattice heat capacity is an essential physical quantity reflecting the thermal properties of the crystal. The specific solution of lattice specific heat is a rather complicated problem. In general discussion, the Einstein model and the Debye model are often used. T internal energy of a solid matter includes the lattice vibration energy and the energy of the electron movement. In an ordinary condition expect for the very low temperature region, the energy of electron movement can generally be omitted because its contribution to the specific heat is much smaller than that of the lattice vibration energy. Here, I only discuss the contribution of lattice vibrations to the heat capacity are discussed.

2.2.1 Classical theory

In 1819, the French scientists Dulong and Petit discovered that most of the elemental solids have nearly the same specific heat capacity regardless of the element near room temperature. This finding is called the Dulong-Petit Law after their names. In physics, the Dulong-Petit Law reveals the direct relationship between the specific heat of the macroscopic physical quantities and the number of microscopic particles for the first time.

According to the classical law of equipartition of energy, atoms subjected to simple harmonic forces can be regarded as an ensemble of harmonic oscillators. This law distributes the energy of $\frac{1}{2}k_BT$ to one degree of freedom. Since there are N_A atoms a solid matter per mole, therefore, the average internal energy of the solid matter holds

$$\bar{E} = 3N_Ak_BT, \tag{2-2-1}$$

where k_B is the Boltzmann's constant.

Then, the specific heat at a constant volume C_V can be obtained as:

$$C_V = (\frac{\partial \bar{E}}{\partial T})_V = 3N_Ak_B = const = 5.96\,\text{cal/mol K}. \tag{2-2-2}$$

2.2.2 Einstein model

In 1907, Einstein used the quantum theory to explain how the specific heat of a solid decreases with temperature. Einstein retained the idea that the thermal vibration of atoms could be described by harmonic oscillators, but abandoned the classical idea and assumed that the energy of the harmonic oscillator was quantized by

$$\varepsilon_i = \left(n + \frac{1}{2}\right)\hbar\omega_i, \tag{2-2-3}$$

where ω_i is the frequency of the i vibration mode.

In a state of thermal equilibrium with the ambient temperature, the average energy of the harmonic oscillator holds

$$\overline{\varepsilon_i} = (\frac{1}{2} + \frac{1}{\exp\left(\hbar\frac{\omega_i}{k_BT}\right)-1})\hbar\omega_i. \tag{2-2-4}$$

To determine the average energy of a harmonic oscillator, Einstein made the straightforward assumption that all the atoms in the crystal were vibrating at the same frequency ω_E. Therefore, at a specific temperature, the total vibration energy (ignoring

the zero-point energy $\frac{1}{2}\hbar\omega_i$) of a crystal composed of N atoms is

$$\bar{E} = \sum_{i=0}^{3N} \varepsilon_i = \sum_{i=0}^{3N} \frac{\hbar\omega_i}{\exp\left(\hbar\frac{\omega_i}{k_B\mathrm{T}}\right)-1} = 3N\frac{\hbar\omega_E}{\exp\left(\hbar\frac{\omega_E}{k_B\mathrm{T}}\right)-1}. \quad (2\text{-}2\text{-}5)$$

Therefore, the specific heat follows that:

$$C_V = \frac{\partial\bar{E}}{\partial T} = 3Nk_B\frac{(\frac{\hbar\omega_E}{k_B\mathrm{T}})^2 exp\frac{\hbar\omega_E}{k_B\mathrm{T}}}{[exp\,(\frac{\hbar\omega_E}{k_B\mathrm{T}})-1]^2}. \quad (2\text{-}2\text{-}6)$$

The Einstein temperature is defined as

$$T_E = \frac{\hbar\omega_E}{k_B}. \quad (2\text{-}2\text{-}7)$$

Then the specific heat can be rewritten as

$$C_V = 3Nk_B\frac{(\frac{T_E}{T})^2 exp\frac{\mathrm{T}_E}{T}}{[exp\,(\frac{T_E}{T})-1]^2} = 3Nk_B f_E(\frac{\mathrm{T}_E}{T}). \quad (2\text{-}2\text{-}8)$$

where $f_E(\frac{\mathrm{T}_E}{T})=\frac{(\frac{T_E}{T})^2 exp\frac{\mathrm{T}_E}{T}}{[exp\,(\frac{T_E}{T})-1]^2}$, is called Einstein heat capacity function, which is a function of temperature.

The above discussion is based on the fact that a crystal has N primitive cells, and each primitive cell has only one atom. For the case that the crystal has N primitive cells and each protocell has n atoms, then:

$$C_V = 3nNk_B\frac{(\frac{T_E}{T})^2 exp\frac{\mathrm{T}_E}{T}}{[exp\,(\frac{T_E}{T})-1]^2} = 3nNk_B f_E(\frac{\mathrm{T}_E}{T}). \quad (2\text{-}2\text{-}9)$$

At high temperatures, $T >> T_E$, and $f_E(\frac{\mathrm{T}_E}{T}) \approx 1$, then

$$C_V = 3Nnk_B. \quad (2\text{-}2\text{-}10)$$

This is the same result as *Dulong-Petit Law.* Because at high temperature, the harmonic oscillator is in a highly excited state, k_BT is much larger than $\hbar\omega_i$, the quantum nature of the vibration becomes less critical, resulting in the classical theory.

At low temperature region, $T << T_E$, the condition is satisfied $e^{\left(\frac{T_E}{T}\right)} \gg 1$. Then

$$C_V = 3Nk_B(\frac{T_E}{T})^2 e^{-\left(\frac{T_E}{T}\right)}. \quad (2\text{-}2\text{-}11)$$

Obviously, the exponential term in the expression of the specific heat plays a significant

role as the temperature goes to zero. Accordingly, the specific heat goes zero.

When $T \rightarrow 0$, $C_V \rightarrow 0$, this is qualitatively consistent with the experimental results. However, the more detailed experimental results show that C_V is proportion to T^3 when the temperature is accordingly to zero. This fact indicates that the model used in the Einstein theory is too simple because the only one single frequency was used in the Einstein model. This does not describe well the reality of the phonons in the real crystals. The Einstein model actually ignores the contribution of acoustic branches to the specific heat in lower-frequency conditions. At low temperatures, however, the contribution of acoustic branches to the heat capacity is the dominant one. Therefore, the heat capacity shown in the above the Einstein model cannot describe the experimental results correctly.

2.2.3 Debye model

Einstein considered the vibrations of the atoms in a solid to be independent of each other so that all 3N oscillations are of the same frequency. In fact, there are powerful interactions between those atoms, and the frequency of the vibrational lattice wave is not fixed, but there is a distribution.

In 1912, Debye modified the concept that atoms behave as independent harmonic oscillators. He considered the collective vibrational mode of the lattice and assumes that the crystal is a continuous elastic medium and the thermal motion of atoms in the form of elastic waves. Each elastic wave vibration mode is equivalent to a harmonic oscillator, and the energy is quantized.

The Debye model regards Bragg lattice as an isotropic continuous medium, *i.e.*, the lattice wave is regarded as an elastic wave. The velocities of the longitudinal and transverse elastic waves are assumed to be same. Therefore, all phonons have the same linear dispersion relation with frequency:

$$\omega = ck, \tag{2-2-12}$$

here k is the wavenumber, c is the sound velocity.

In the three-dimensional space with a given volume V, the number of vibrational modes per unit volume is given by $\frac{V}{(2\pi)^3}$. The Debye model also assumes that the *first Brillouin zone* is a sphere with a radius of k_D. Then the total number of modes M holds:

$$M = \frac{V}{(2\pi)^3}\left(\frac{4\pi k^3}{3}\right). \tag{2-2-13}$$

Hence, we can obtain the vibrational density of states (VDOS) $g(\omega)$ as,

$$g(\omega) = \frac{dM}{d\omega} = \left(\frac{Vk^2}{2\pi^2}\right)\left(\frac{dk}{d\omega}\right). \tag{2-2-14}$$

Combining the equation (2-2-12) and (2-2-14), $g(\omega)$ can be rewritten as

$$g(\omega) = \frac{V\omega^2}{2\pi^2 c^3}. \tag{2-2-15}$$

With the limitation of the radius of the first Brillouin zone, a particular maximum angular frequency is defined as the Debye frequency. Assume the crystal has N atoms in and 3N degrees of freedom, and it can only have 3N modes of vibration, as follows

$$\int_0^{\omega_D} g(\omega)d\omega = 3N. \tag{2-2-16}$$

Thus,

$$\omega_D = \left(\frac{6\pi^2 N}{V}\right)^{1/3} c_D. \tag{2-2-17}$$

here c_D is the Debye sound velocity.

Then the Debye temperature follows as

$$T_D = \frac{\hbar\omega_D}{k_B}. \tag{2-2-18}$$

With the assumption of $g(\omega)$

$$\bar{E} = \int_0^{\omega_D} d\omega g(\omega) \frac{\hbar\omega}{\exp\left(\frac{\hbar\omega}{k_B \mathrm{T}}\right)-1}. \tag{2-2-19}$$

By setting $\frac{\hbar\omega}{k_B \mathrm{T}} = x$, equation (2-2-19) can be rewritten as

$$\bar{E} = 9Nk_B T\left(\frac{T}{T_D}\right)^3 \int_0^{\frac{T}{T_D}} \frac{x^3}{e^x - 1} dx. \tag{2-2-20}$$

By substituting equation (2-2-15) into equation (2-2-20), the specific heat at constant volume can be obtained as:

$$C_V = \left(\frac{\partial \bar{E}}{\partial T}\right)_V = 9Nk_B T\left(\frac{T}{T_D}\right)^3 \int_0^{\frac{T}{T_D}} \frac{x^4 e^x}{(e^x - 1)^2} dx. \tag{2-2-21}$$

At high temperature condition, $T >> T_D$ and $x << 1$. Therefore,

$$\bar{E} = 9Nk_BT(\frac{T}{T_D})^3 \int_0^{\frac{T}{T_D}} x^2 dx = 3Nk_BT. \quad (2\text{-}2\text{-}22a)$$

and

$$C_V = 3Nk_B.$$

This is the same result as the Dulong-Petit Law and the Einstein model. This is equivalent to the classical case where all elastic wave modes are excited, and quantum effects can be ignored here.

At low temperatures, $T << T_D$ and $x << 1$. Hence,

$$\bar{E} = 9Nk_BT(\frac{T}{T_D})^3 \int_0^{\frac{T}{T_D}} \frac{x^3}{(e^x-1)^2} dx = \frac{3}{5}\pi^4. \quad (2\text{-}2\text{-}22b)$$

$$C_V = \frac{12}{5}\pi^4 Nk_B \left(\frac{T}{T_D}\right)^3.$$

This result is different from that of Einstein model and is called the Debye's Law of the specific heat. As long as the appropriate Debye temperature is selected, the results calculated by this expression can well fit the experimental results. Because at low temperatures, only long-wavelength phonon modes are activated. The Debye model correctly predicts the specific heat of solids at low temperatures, which is proportional to T^3. Therefore, the Debye model is also called the Debye T^3 law.

2.3 The glass system

(From Chapter 3 of *Glassy materials and disordered solids: An introduction to their statistical mechanics*, Binder, K., & Kob, W. 2011)

Amorphous solids, also named as non-crystalline solids or glasses, are materials that have random structures without having a periodic structure. This means atoms in amorphous materials do not have any translational symmetry as crystals do. Figure 2-6 shows the "Continues Random Network" (CNR) models of crystalline SiO_2 and amorphous SiO_2, which proposed by Zachariasen (Shibata, 2015). As compared with the crystal silica of Figure 2-6(a), the glass has an irregularly atomic arrangement, as shown in Figure 2-6(b).

(1) Short-range order

The short-range order refers to the arrangement of atoms or structural units over a short distance, usually with one or two atom spacings. For example, in silica glass, the unit structure is SiO_2 tetrahedra, which is the same as silica crystals (orange circle in Figure 2-6).

(2) Medium-range order

The order is realized at least several structural units that are regularly connected. For example, in the case of silica crystals, two Si atoms share one O atom and constitute only a ring consisting of six structural units (six-membered ring). While in glass, it is composed of a four- to eight-membered ring. It is the origin of the irregular structure (blue circle in Figure 2-6). It can not be called long-range order because it has distribution in bond angles and bond lengths and a significant degree of freedom.

(3) Long-range order

The long-range order occurs in the periodic arrangement of unit structures over long distances. In crystals, a unit structure arrangement has a translational symmetry. In glasses, medium-range order exists, but they are randomly placed and do not have the long-range order (red circle in Figure 2-6(a)). That is, amorphous is defined as a state with short/medium-range order only but no long-range order.

2.3.1 Glass transition

The glass transition is a peculiar phenomenon that distinguishes an amorphous material or glass. Figure 2-6 shows a schematic diagram of the temperature dependence of enthalpy in the process of liquid cooling at constant pressure. When a liquid cools down to the temperature below the melting point, T_m, two possible processes may occur. First, the liquid may crystalize to the crystalline structure, and the enthalpy decrease discontinuously. If there are multiple crystalline states, namely, multiple minima of energy, it may have multiple melting points. This process is called the phase transition. Second, when the liquid cools down to T_m with fast speed, it will deviate from thermodynamical equilibrium and become a metastable supercooled liquid with the enthalpy decrease continually. It involves two thermodynamical nonequilibrium states: supercooled fluid and glass. As the supercooled liquid further cools down, the viscosity of the substance increases, and at a specific temperature, the system can be regarded as a frozen solid. Frozen solid is a glassy state, and the process of the supercooled liquid reaching glass is called glass transition. The specific temperature is called the glass transition temperature, T_g. There are various methods to determine T_g. For example, as shown in Figure 2-7, T_g is defined as the temperature point at the intersection of the liquid phase and glass phase lines. The T_g depends on the cooling rate and decreases as the cooling rate decreases.

Crystallization is a phase transition in an equilibrium state that occurs at the melting point, whereas glass transition is a transition to a non-equilibrium state and is not a phase transition. That is, the glass transition depends on the heat application (heat history) and the cooling rate. When the cooling rate increases, the glass has a structure closer to the equilibrium liquid rather than a glass, and the glass transition temperature also increases.

The glass transition is characterized by the dynamic performances of the supercooled liquid that significantly changes with temperature. The viscosity η is a vital characteristic parameter of the fluid dynamics. As the temperature reduces, η increases dramatically. Usually, when η equals $10^{13.5}$ poise (poise for the viscosity unit, usually expressed in P, where 1P = 10^{-1} Pa•s) where liquid transfer into the glass, the corresponding temperature is called the glass transition temperature T_g.

Complex liquid makes the relationship between viscosity and temperature is very complicated. For example, the viscosity of SiO_2 liquid with the temperature well conforms to the simple exponential relationship of the Arrhenius relationship:

$$\eta = \eta_0 e^{E/kT}, \tag{2-3-1}$$

where E is the relevant activation energy, and η_0 is approximately a constant. However, the relationship between viscosity and temperature of the conventional liquid has obviously deviated from the Arrhenius relationship, but meet empirical Vogel-Fulcher-Tammann (VFT) relation:

$$\eta = C\eta_0 e^{B/(T-T_0)}, \tag{2-3-2}$$

where T_0 is the Vogel temperature, which is usually considered to be a dynamic ideal glass transition temperature.

According to the relationship between viscosity and temperature, the liquids can be divided into the strong fluid and the fragile fluid (Angell1, 1991). The η (or relaxation time) meets Arrhenius's relation with the temperature liquid known as the strong fluid, and the liquid satisfying the VFT formula is fragile fluid. The concept of fragility by the magnitude of the fragility index m represented by Equation (2-3-3).

$$m = \left.\frac{\partial \log_{10}\eta}{\partial(T_g/T)}\right|_{T=T_g}. \tag{2-3-3}$$

The fragility also describes the degree of concaveness of the plot of T_g and log τ_α.

Generally, the glass transition temperature is measured by a thermal analysis method, for example, the differential scanning calorimetry (DSC). In conclusion, an amorphous system exhibiting a glass transition is defined as glass. After this, this amorphous solid refers to glass.

2.3.2 Relaxation phenomena

(From the book of *Relaxation and Diffusion in Complex Systems*, K.L. Ngai, 2011)

In a glassy state, the atoms or molecules are still moving toward the equilibrium position with a plodding speed, which human beings cannot catch up. This process is much more complex to understand and is known as relaxation phenomena. A macroscopic equilibrium system becomes a non-equilibrium state due to the change of the surrounding environment or the action of the outside world. The process from non-equilibrium state to a new equilibrium state is called the relaxation process. The relaxation process is essentially a process in which microparticles exchange energy due to interaction and finally reach the most stable distribution. The macroscopic law of the relaxation process depends on the properties of the microcosmic particle interaction in the system. Therefore, studying relaxation is one of the most effective ways to obtain information about these interactions.

In a glassy system, various relaxation phenomena are observed, typically by the structural relaxation in which the atomic structure transfers to a new equilibrium state. The simplest example of the relaxation process is the Debye relaxation phenomenon. The response function ψ(t) is a time correlation function named Kohlransch function that decreases exponentially. Therefore,

$$\psi(\mathrm{t}) = e^{-\frac{t}{\tau}}. \tag{2-3-4}$$

Here, τ is the relaxation time and indicates which time scale the equilibrium state is reached. In the general glassy system, the relaxation phenomena show different temperature dependences at various time scales, as shown in Figure 2-8.

The α-relaxation, also called the primary relaxation, is the structural rearrangement of atoms or molecules that occur in all glasses in the MHz region. The α-relaxation is believed to occur as a result of the cooperative movement of regions with several molecules of the supercooled liquid. It shows remarkable temperature dependence compared with other relaxation processes. In most glassy systems, the α-relaxation act the linear, exponential relationship with time as Kohlransch function as described above. A most commonly used expression is

$$\psi(\mathrm{t}) = e^{\left(-\frac{t}{\tau}\right)^{1-n_a}} (0 \leq n_a < 1). \tag{2-3-5}$$

This structural relaxation is considered directly to be related to the glass transition.

There is a faster secondary relaxation compared to α-relaxation, such as β-relaxation and γ-relaxation. These relaxation processes depend on the molecular structure and occur

relatively in the several Hz to GHz band in a fast process. There is also a fast chewing relaxation, which is a localized motion in the cage predicted from the mode-coupling theory. These are measured by broadband dielectric spectroscopy or Brillouin scattering. In the relaxation process of THz band of glass, the low energy excited boson peak derived from the random structure and local, the fast movement of relaxation in structural cage caused by vitrification is visible. The low-temperature properties and the boson peak will be described in the following chapters.

2.3.3 Fractal dimension

In 1975, Mandelbrot *et al.* proposed the concept of fractal for the first time, to quantify the structures and properties of disorder systems, which uses a fractal dimension to replace the integer dimension used in crystalline systems (Dewey, 1998). The fractal is widely applied to describe the statistical properties and the randomness of the self-similar structure of monomers in glasses. Self-similarity has the same structure independent of the location or magnification (Dewey, 1998). Self-similarity has no characteristic size; it is continuous but cannot be differentiated everywhere.

Figure 2-9 shows the structure of the Koch curve, which is a popular self-similarity. As shown in the figure, the Koch curve shows a self-similar feature, even when the scale is enlarged. In addition to the Koch curve, such features can also be seen in complex coastlines, mountain undulations, and polymer chain structures. However, these fractal structures found in nature are not entirely similar in part and whole, but appear to have similar complexity, and are self-similar in a statistical sense. To recognize the fractal structure, the scale at which it is observed becomes a complex problem. Thus, the concept of fractal only makes sense at a particular scale, and the structure no longer has self-similarity when viewed at a smaller or larger scale.

2.3.4 Boson peak

As we presented in section 2.2.3, the thermal properties of a crystal can be described by the Debye model. The Debye model demonstrated that the vibrational density of states (VDOS) $g(\omega)$ should be proportional to the square of frequency ω^2 and consequently, low-temperature heat capacity should be proportional to T^3:

$$\frac{g(\omega)}{\omega^2} = const. \tag{2-3-6}$$

$$\frac{C_V(T)}{T^3} = const. \tag{2-3-7}$$

However, in the disordered system, the Debye model completely fails to explain the vibrational density of states and the heat capacity at low temperatures. A broad peak is appearing in the C/T^3 spectrum between 1 K to 20 K, as shown in Figure 2-10, which is called the excess heat capacity (Carini et al., 2016). In this region, the non-Debye excess heat capacities of glasses in comparison with those of the crystalline counterparts are observed, known as "boson peak." The boson peak (BP) refers to "the excess low-frequency vibrational density of states *(VDOS)*, $g(v)$". At the same time, the so-called fractal dynamics can be observed near the BP frequency, owing to the self-similar structure of monomers in polymeric glasses. The dynamic can be described by

$$g(v) \propto v^{d_f-1}, \tag{2-3-8}$$

where d_f is the dynamic fracton dimension.

It is a glass-specific vibration mode observed in glassy (amorphous) systems and widely used to analyze the heat capacity and thermal conductivity of glassy materials. The specific plateau behavior in the temperature-dependence of thermal conductivity has been observed in glassy materials, and the boson peak observed in the T-dependence of C_P/T^3 in the inelastic scattering of light or neutrons (Shintani & Tanaka, 2008; Marruzzo et al., 2013; Baldi et al., 2017).

However, the origin and the mechanism of BP are still in controversy (Parshin et al., 2007; Buchenau & Schober, 2008). Several explanations have been proposed recently. Shintani suggested that the boson peak may be caused by the Ioffe–Regel limit of transverse vibrational modes in glassy systems (Shintani & Tanaka, 2008; Chumakov et al., 2011). Mori and his coworkers concluded that BP is attributed to the longer correlated length of the medium-range order and the concentration of hydroxyl groups. Violini *et al.* claimed BP to the first sharp diffraction peak (FSDP) of the static structure factor $S(Q)$ that similar to phonons in crystalline materials (Violini et al., 2012).

So far, the BP in glassy materials has been investigated by a variety of methods such as inelastic neutron scattering (INS) or X-ray scattering (IXS), the low-temperature thermal properties, low-frequency Raman scattering (LFRS) and numerical molecular dynamics simulations (MD) (Ruzicka et al., 2004; Matic et al., 2004; Crupi et al., 2010; Hédoux et al., 2009; Kojima et al., 1993). The BP can also be detected by dividing the absorption coefficient by the square of frequency $\alpha(v)/v^2$ according to the following relationship between the absorption coefficient $\alpha(v)$ and VDOS $g(v)$ (Galeener & Sen, 1978; Taraskin et al., 2006; Shibata et al., 2015; Kabeya et al., 2016; Terao et al., 2018; Kojima et al.,

2014).

$$\frac{\alpha(\nu)}{\nu^2} = C_{IR}(\nu) \cdot \frac{g(\nu)}{\nu^2}. \tag{2-3-9}$$

Here $C_{IR}(\nu)$ is the IR light-vibration coupling coefficient, which formalized by several models proposed by previous works (Tarashin et al., 2006; Kabeya et al., 2017; Mori et al., 2019). In 2019, Mori and his coworkers modified the expression of $C_{IR}(\nu)$ in the fracton region as

$$C_{IR}(\nu) = A + B\nu^{2\frac{d_f}{D_f}}, \tag{2-3-10}$$

where D_f is the static fractal dimension. Generally, in disorder systems, the fracton dimension d_f is smaller than the fractal dimension D_f (Mori et al., 2019).
Combining equation (2-3-8) and (2-3-10), we got the following relationship between absorption coefficient and frequency

$$\alpha(\nu) \propto \nu^{2\frac{d_f}{D_f}+d_f-1}. \tag{2-3-11}$$

Figures

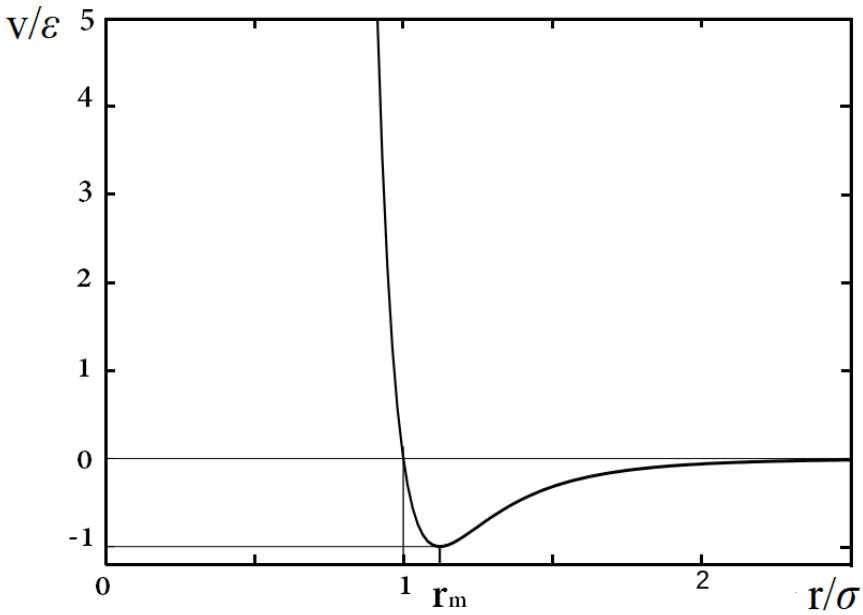

Figure 2-1 A graph of Lennard-Jones potential versus distance [Source: https://en.wikipedia.org/wiki/Lennard-Jones_potential].

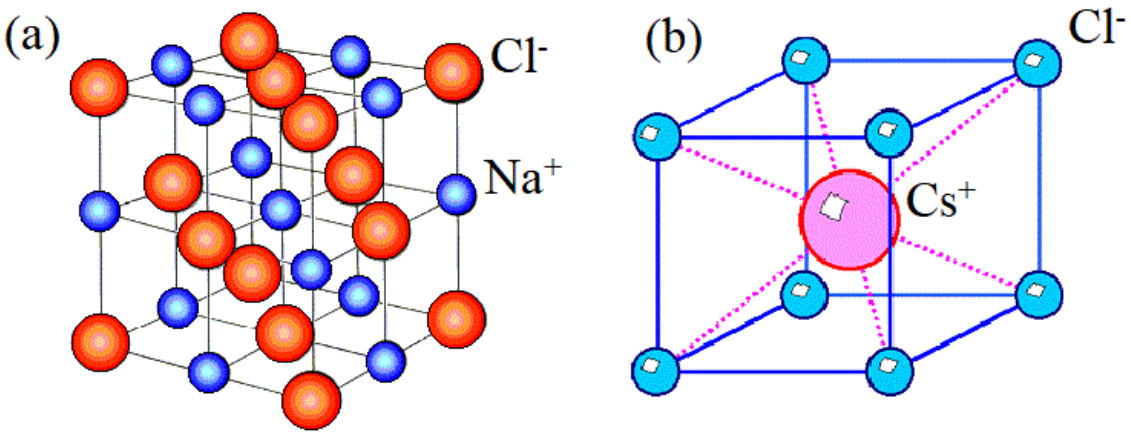

Figure 2-2 Atomic structure for sodium chloride (NaCl) and cesium chloride (CsCl) [Source: https://www.tf.uni-kiel.de/matwis/amat/def_en/kap_2/basics/b2_1_6.html].

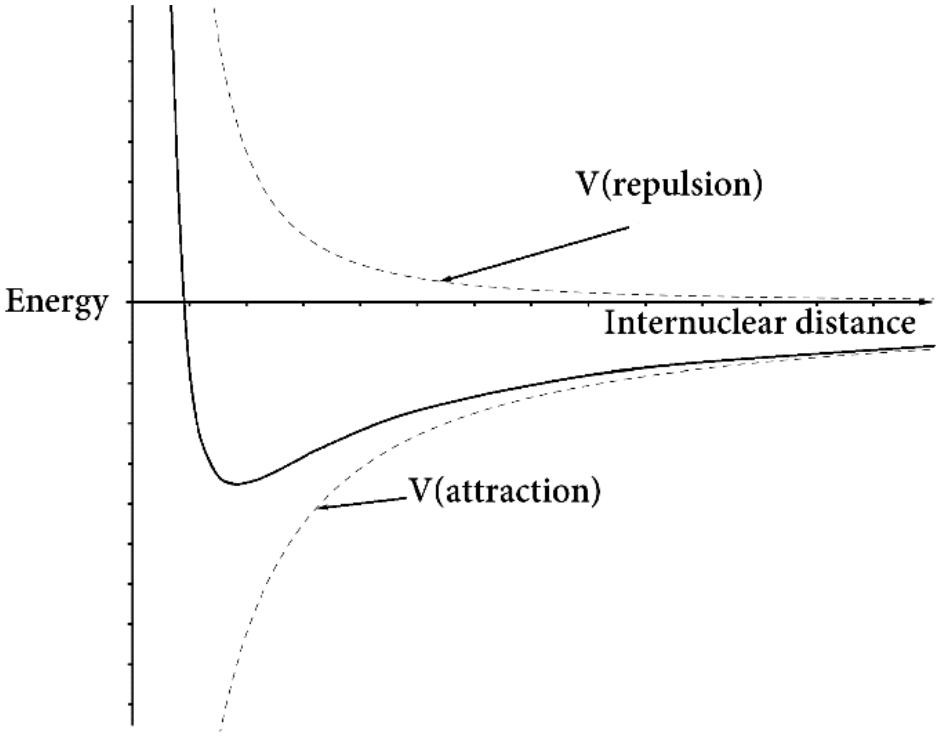

Figure 2-3 Energy per molecule of ion crystal.

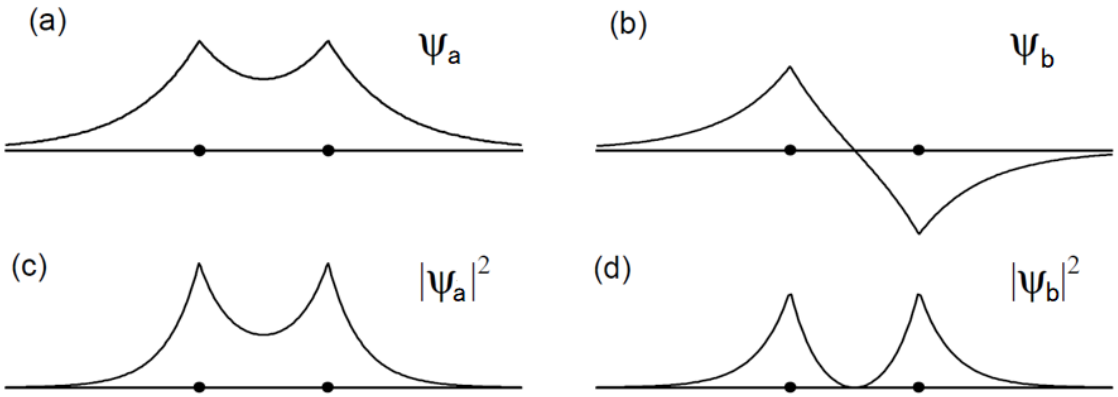

Figure 2-4 The combination schemes of two atoms. (a) and (b) are bonding orbital and antibonding orbital. (c) and (d) are the charge distribution of these two orbitals.

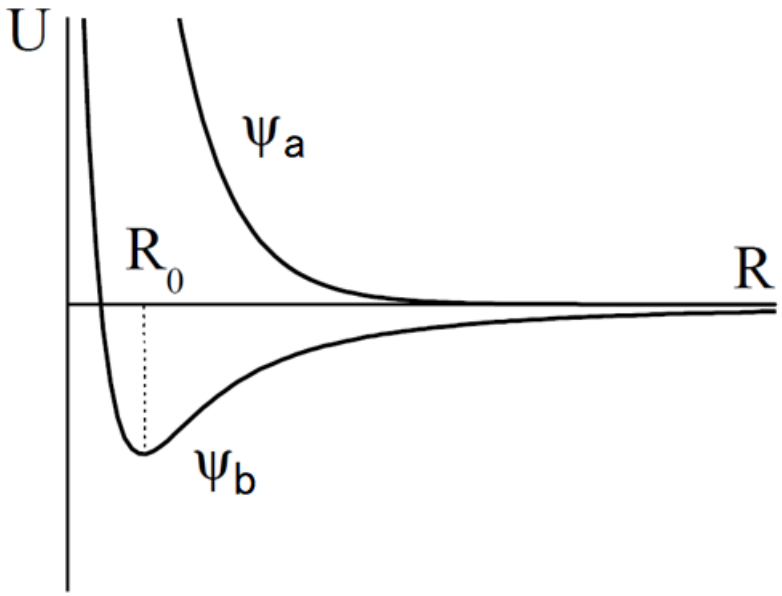

Figure 2-5 The energies of bonding orbital Ψ_a and antibonding orbital Ψ_b.

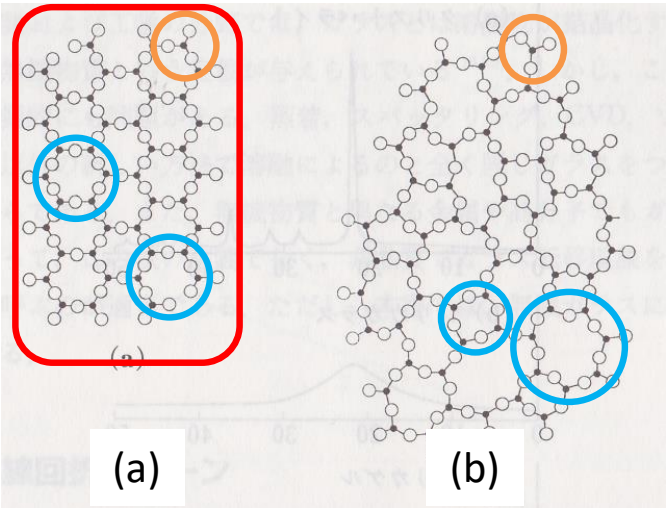

Figure 2-6 Two-dimensional representation of the structure of (a) silica crystals and (b) silica glass. ● represents Si atom, ○ represents O atom (Shibata, Master's thesis, 2015).

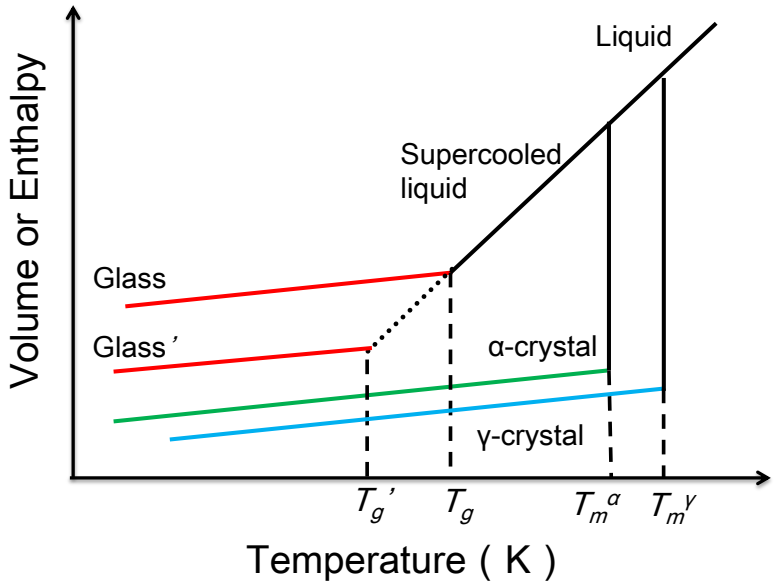

Figure 2-7 Schematic of the temperature dependence of enthalpy under constant pressure. T_g is the glass transition temperature.

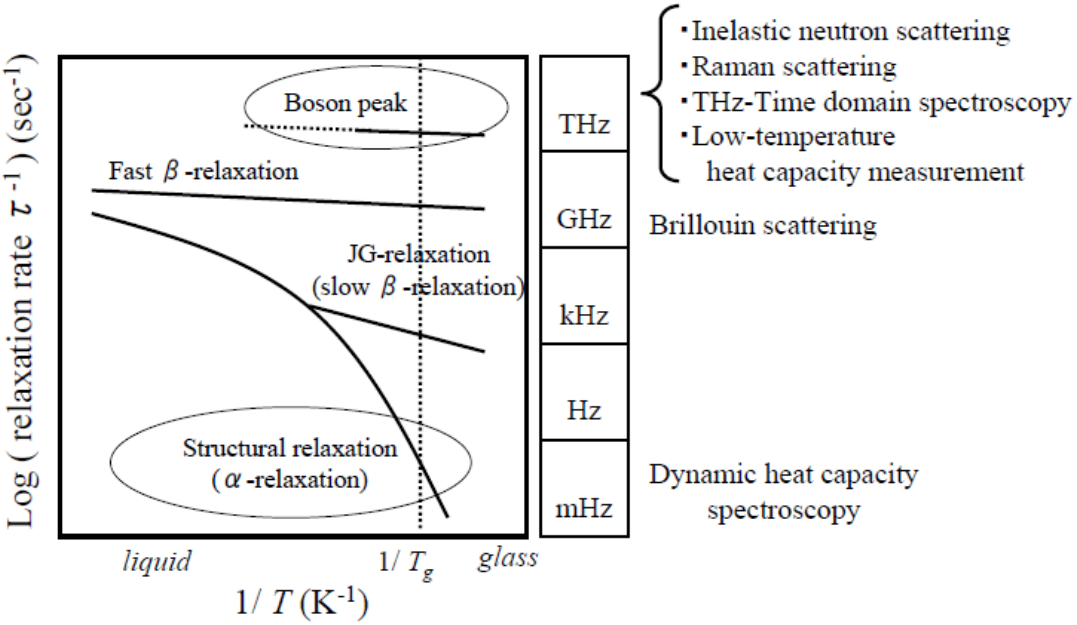

Figure 2-8 Relaxation map (Matsuda, Doctoral thesis, 2010).

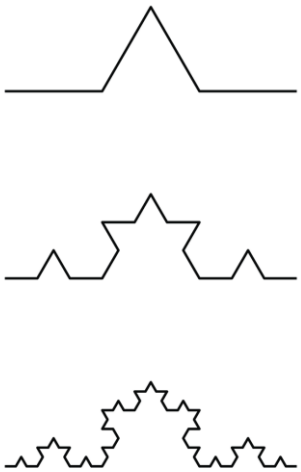

Figure 2-9 The constructure of the Koch curve (Dewey, 1998).

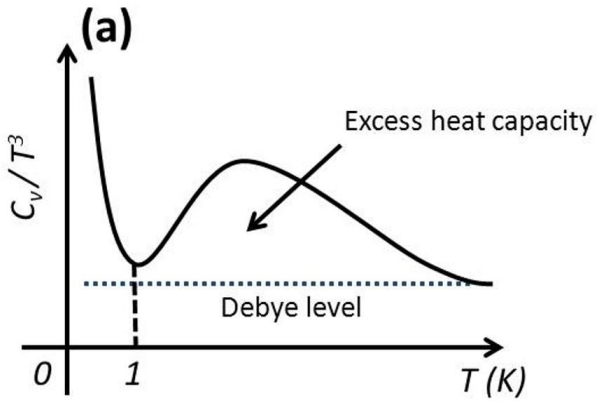

Figure 2-10 Schematic diagram of the low-temperature heat capacity of glasses. The figure is reproduced from ref (Matsuda, doctoral thesis, 2010).

Chapter 3 Terahertz technology

3.1 The interaction of light with matter

*(*From Chapter 2 of *Electrodynamics of solids: optical properties of electrons in matter,* Martin Dressel & George Grüner, 2002)

3.1.1 Maxwell equations in vacuum

The Maxwell equations and their time-dependent solutions describe all the classical electrodynamic phenomena and reveal the interactions between electromagnetic waves. The Maxwell equations in the vacuum are the fundamental equations of the electromagnetic field and the basic theory of electromagnetic problems. They are and expressed with the following forms:

$$\nabla \times \mathbf{E}(\mathbf{r},t) + \frac{1}{c}\frac{\partial \mathbf{B}(\mathbf{r},t)}{\partial t} = 0, \quad \text{(3-1-1a)}$$

$$\nabla \cdot \mathbf{B}(\mathbf{r},t) = 0, \quad \text{(3-1-1a)}$$

$$\nabla \times \mathbf{H}(\mathbf{r},t) - \frac{1}{c}\frac{\partial \mathbf{D}(\mathbf{r},t)}{\partial t} = \frac{4\pi}{c}\mathbf{J}(\mathbf{r},t), \quad \text{(3-1-1c)}$$

$$\nabla \cdot \mathbf{D}(\mathbf{r},t) = 4\pi\rho(\mathbf{r},t), \quad \text{(3-1-1d)}$$

where **E** and **B** are the electric field strength and magnetic induction, respectively. c is the light speed in a vacuum ($2.99792458 \times 10^{10}$ cm/s). **J** and ρ are the current density and the charge density, respectively.

In the vacuum condition, **J** = 0 and $\rho = 0$. The combination of *Faraday's induction law* (3-1-1a), Ampère's circuital law (3-1-1c), and Coulomb's law (3-1-1d) yields

$$\frac{1}{c^2}\frac{\partial^2 \mathbf{E}}{\partial t^2} = \nabla^2 \mathbf{E}, \quad \text{(3-1-2a)}$$

One solution of equation (3-1-2a) is expressed by a harmonic wave

$$\mathbf{E}(\mathbf{r},t) = \mathbf{E}_0 \exp\{\mathrm{i}(\mathrm{q}\cdot\mathrm{r} - \omega t)\}. \quad \text{(3-1-3)}$$

Similarly, because $q = \omega/\mathrm{c}$, the **B** field can have the same form and similar wave solution

$$\frac{1}{c^2}\frac{\partial^2 \mathbf{B}}{\partial t^2} = \nabla^2 \mathbf{B}, \quad \text{(3-1-2b)}$$

These wave functions are the simplest form without desperation. Such linearly polarized electromagnetic rendition is showing in Figure 3-1.

When there is a matter existing, the electric field and magnetic field will interact with the mater and lead to electric dipoles, magnetic moments, polarization charges, and induced current. Therefore, the total charge density becomes

$$\rho_{\text{total}} = \rho_{\text{ext}} + \rho_{\text{pol}}, \tag{3-1-4}$$

and the total current density becomes

$$\mathbf{J}_{\text{total}} = \mathbf{J}_{\text{cond}} + \mathbf{J}_{\text{bond}}. \tag{3-1-5}$$

where $\mathbf{J}_{\text{cond}} = \sigma_1\mathbf{E}$ (Ohm's law), σ_1 is the conductivity of the matter.

In this case, the electric displacement **D** and the magnetic field strength are introduced to account for the modifications by the medium:

$$\mathbf{D} = \epsilon_1\mathbf{E} = (1 + 4\pi\chi_{\text{e}})\mathbf{E} = \mathbf{E} + 4\pi\mathbf{P}, \tag{3-1-6}$$

$$\mathbf{B} = \mu_1\mathbf{H} = (1 + 4\pi\chi_{\text{m}})\mathbf{H} = \mathbf{H} + 4\pi\mathbf{M}, \tag{3-1-7}$$

where χ_{e} is the dielectric susceptibility, and χ_{m} is the magnetic susceptibility. μ_1 is the permeability and, in most cases, μ_1=1.Therefore, the Maxwell equations in a medium can be rewritten as follows:

$$\nabla \times \mathbf{E} + \frac{1}{c}\frac{\partial \mathbf{B}}{\partial t} = 0, \tag{3-1-8a}$$

$$\nabla \cdot \mathbf{B} = 0, \tag{3-1-8b}$$

$$\nabla \times \mathbf{H} - \frac{1}{c}\frac{\partial \mathbf{D}}{\partial t} = \frac{4\pi}{c}\mathbf{J}_{\text{cond}}, \tag{3-1-8c}$$

$$\nabla \cdot \mathbf{D} = 4\pi\rho_{\text{ext}}, \tag{3-1-8d}$$

Combining with equation (3-1-6) and Ohm's law, equation (3-1-8c) can be transformed into

$$c\nabla \times \mathbf{H} = -\text{i}\omega\epsilon_1\mathbf{E} + 4\pi\sigma_1\mathbf{E} = -\text{i}\omega\hat{\epsilon}\mathbf{E}. \tag{3-1-9}$$

Then, we can get the complex dielectric constant by assuming $\partial\mathbf{D}/\partial\text{t} = \text{-i}\omega\mathbf{D}$

$$\hat{\epsilon} = \epsilon_1 + i\frac{4\pi\sigma_1}{\omega} = \epsilon_1 + \text{i}\epsilon_2, \tag{3-1-10}$$

In a vacuum, the propagating electric and magnetic waves can be expressed by two sinusoidal periodic functions with wavevector q and frequency ω.

$$\mathbf{E}(\mathbf{r}, t) = \mathbf{E}_0 \exp\{\text{i}(\mathbf{q}\cdot\mathbf{r} - \omega t)\}, \tag{3-1-11a}$$

$$\mathbf{H}(\mathbf{r}, t) = \mathbf{H}_0 \exp\{\text{i}(\mathbf{q}\cdot\mathbf{r} - \omega t - \varphi)\}. \tag{3-1-11b}$$

Combining Maxwell equations (3-1-8a) and (3-1-8d) with (3-1-4), (3-1-5), and Ohm's law, the propagating electric field, and magnetic field can be obtained

$$\nabla^2\mathbf{E} - \frac{\epsilon_1\mu_1}{c^2}\frac{\partial^2\mathbf{E}}{\partial t^2} - \frac{4\pi\epsilon_1\mu_1}{c^2}\frac{\partial \mathbf{E}}{\partial t} = 0, \tag{3-1-12a}$$

$$\nabla^2\mathbf{H} - \frac{\epsilon_1\mu_1}{c^2}\frac{\partial^2\mathbf{H}}{\partial t^2} - \frac{4\pi\epsilon_1\mu_1}{c^2}\frac{\partial\mathbf{H}}{\partial t} = 0. \quad (3\text{-}1\text{-}12b)$$

Substituting (3-1-11a) into (3-1-12a), we can get the dispersion relation between wavevector q and the frequency ω.

$$\mathbf{q} = \frac{\omega}{c}\left[\epsilon_1\mu_1 + i\frac{4\pi\epsilon_1\mu_1}{\omega}\right]^{\frac{1}{2}}\mathbf{n_q}, \quad (3\text{-}1\text{-}13)$$

where $\mathbf{n_q} = \mathbf{q}/|\mathbf{q}|$.

3.1.2 Optical parameters

When an electromagnetic wave is propagating in a material, the dielectric constant, the conductivity, and the permeability are the commonly used parameters to describe the optical properties of the material. And the complex refractive index is used to describe the electromagnetic wave propagating and dissipating in the material,

$$\widehat{N} = n + ik = \left[\epsilon_1\mu_1 + i\frac{4\pi\mu_1\sigma_1}{\omega}\right]^{\frac{1}{2}} = [\hat{\epsilon}\mu_1]^{\frac{1}{2}}. \quad (3\text{-}1\text{-}14)$$

The real part of the complex refractive index n represents the wave propagation, and the image part k describes the dissipation of the wave.

The value of the complex wavevector $\mathbf{q} = \hat{q}\mathbf{n_q}$ then can be defined as

$$\hat{q} = \frac{\omega}{c}\widehat{N} = \frac{n\omega}{c} + \mathrm{i}\frac{k\omega}{c}, \quad (3\text{-}1\text{-}15)$$

where

$$n^2 = \frac{\mu_1}{2}\left\{\left[\epsilon_1^2 + \left(\frac{4\pi\sigma_1}{\omega}\right)^2\right]^{\frac{1}{2}} + \epsilon_1\right\}, \quad (3\text{-}1\text{-}16)$$

$$k^2 = \frac{\mu_1}{2}\left\{\left[\epsilon_1^2 + \left(\frac{4\pi\sigma_1}{\omega}\right)^2\right]^{\frac{1}{2}} - \epsilon_1\right\}. \quad (3\text{-}1\text{-}17)$$

And the phase difference φ between the magnetic field and dielectric field is

$$\tan\varphi = \frac{k}{n}. \quad (3\text{-}1\text{-}18)$$

In the presence of matter, the dielectric constant and conductivity are applied to describe the optical properties of the matter.

$$\hat{\epsilon} = \epsilon_1 + \mathrm{i}\frac{4\pi\sigma_1}{\omega} = \epsilon_1 + i\epsilon_2, \quad (3\text{-}1\text{-}19)$$

$$\hat{\sigma} = \sigma_1 + \sigma_2. \tag{3-1-20}$$

They can be derived from the complex refraction index with the following equations:

$$\epsilon_1 = \frac{n^2-k^2}{\mu_1}, \tag{3-1-21}$$

$$\epsilon_2 = \frac{2nk}{\mu_1}, \tag{3-1-22}$$

$$\sigma_1 = \frac{nk\omega}{\mu_1}, \tag{3-1-23}$$

$$\sigma_2 = \left(1 - \frac{n^2-k^2}{\mu_1}\right)\frac{\omega}{4\pi}. \tag{3-1-24}$$

When the electromagnetic wave **q** is propagating in a medium, the phase velocity and group velocity are:

$$v_{\text{ph}} = \frac{\omega}{q}, \tag{3-1-25}$$

$$v_{\text{gr}} = \frac{\partial\omega}{\partial q}, \tag{3-1-26}$$

where q is the real part is wavevector **q** and $q = 2\pi/\lambda$.

Substituting the wavevector **q** into (3-1-11a), the electric field can be separated into a real part and imaginary part

$$\mathbf{E}(\mathbf{r}, t) = \mathbf{E}_0 \exp\left\{\mathrm{i}\omega\left(\frac{n}{c}\mathbf{n_q}\cdot\mathbf{r} - t\right)\right\}\exp\left\{-\frac{\omega k}{c}\mathbf{n_q}\cdot\mathbf{r}\right\}. \tag{3-1-27}$$

The first exponent of this equation describes the reduction of velocity from free space c to medium c/n, and the second exponent represents the amplitude attenuation of the damping wave, $\boldsymbol{E}(\boldsymbol{r}) \propto \exp(-\alpha r/2) = \exp(-r/\delta_0)$ as shown in Figure 3-2. δ_0 is the decay length of the electric field.

$$\delta_0 = \left(\frac{\alpha}{2}\right)^{-1} = \frac{1}{Im\{\hat{q}\}} = \frac{c}{\omega k} = \frac{c}{(2\pi\omega\mu_1)^{\frac{1}{2}}}\left\{[\sigma_1^2 + \sigma_1^2]^{\frac{1}{2}} + \sigma_2\right\}^{\frac{1}{2}}. \tag{3-1-28}$$

When $\sigma_1 << |\sigma_2|$,

$$\delta_0 = \left[\frac{c^2}{2\pi\omega\mu_1\sigma_1}\right]^{\frac{1}{2}}. \tag{3-1-29}$$

δ_0 is defined as the skin depth in this case. Then we can obtain the absorption coefficient from the skin depth of δ_0 by Lambert-Beer's law,

$$\alpha = \frac{2k\omega}{c} = \frac{4\pi k}{\lambda_0} = \frac{4\pi\sigma_1\mu_1}{nc}. \tag{3-1-30}$$

3.2 THz technology

*(*From the book of *Principles of Terahertz Science and Technology,* Lee Yun-Shik, 2009*)*

3.2.1 THz spectroscopy

The terahertz (THz) spectroscopy, also named far-infrared spectroscopy or sub-millimeter in earlier ages, refers to electromagnetic waves with frequency in the range of 0.1 - 10 THz (wavelengths corresponding from 30 μm - 3 mm), which locates between microwave and infrared light, as shown in Figure 3-3 (Sirtori, 2002; Taday, 2003a). Frequently used units and their conversions at 1 THz are as follows (Lee, 2009):

• Frequency: v = 1 THz (1 THz =10^{12} Hz) = 1000 GHz;
• Angular frequency: $\omega = 2\pi v$ = 6.28 THz;
• Period: $\tau = 1/v$ = 1 ps;
• Wavelength: $\lambda = c/v$ = 0.3 mm = 300 μm;
• Wavenumber: $\bar{k} = k/2\pi = 1/\lambda$ = 33.3 cm^{-1};
• Photon energy: $hv = \hbar\omega$ = 4.14 meV;
• Temperature: $T = hv/k_B$ = 48 K.

The studies of microwave and infrared at both ends of the terahertz band are very mature. Microwave with a frequency less than 100 GHz can be generated by synthesizer technology or semiconducting devices, and infrared waves with a frequency above 30 THz can be excited by optical means such as laser technologies. Thus, terahertz waves lie right in-between electronics and photonics. For a long time, because of the lack of convenient and high-power terahertz sources and capable terahertz detector that can work stably at room temperature, the research on terahertz has been barren. Therefore, the THz region is regarded as the last unexplored area of the spectrum and known as the "*THz gap*" (Williams, 2007). Until the 1980s, the rapid development of ultra-fast laser technologies and new material developments promoted the considerable boom of terahertz technology and related sciences, leading remarkable advances in THz science and technology (Hafez et al., 2016).

Infrared (IR) spectroscopy technology is one of the most popular tools for biomedical and chemical analysis. Typically, materials in solid phase are formed with intramolecular bonding force, and these vibration modes can be detected by IR spectroscopy. However, the low frequencies are related to week molecular interactions, which are located in the THz region from 300 GHz to approximately 12 THz (25 - 1000 cm^{-1}, as shown in Figure

3-3) (Ge et al., 2009; Takahashi, 2014; Rungsawang et al., 2006; Taday et al., 2003b; Fitzgerald et al., 2005). The THz spectroscopy was demonstrated to have high sensitivity to phonon vibration, low-frequency internal motions, and hydrogen bonding interactions (Globus et al., 2003; Korter et al., 2006; Roth et al., 2010; Kutteruf et al., 2003). Therefore, THz spectroscopy is a complementary technology to traditional IR spectroscopy.

The THz detection is similar to IR detection, but the terahertz technology has many unique features by comparing with infrared detection as following:

1. Transient: The typical pulse width of THz waves is on the order of sub-picosecond ($1ps = 10^{-12}s$). It can not only perform sub-picosecond and femtosecond time-resolved transient spectroscopy studies, but also effectively prevent background radiation noise interference by sampling measurement technology. At present, the signal-to-noise ratio of the radiation intensity measurement is much higher than that of Fourier transform infrared spectroscopy technique (Hadjiloucas et al., 2009).
2. Broadband: The terahertz pulse source usually contains several cycles of the electromagnetic oscillation only (Hafez et al., 2016). The frequency band of a single pulse can cover from tens to tens of ranges, which is very suitable for the study of terahertz absorption spectra of materials in a broad frequency range.
3. Coherence: The coherence measurement technique of terahertz time-domain spectroscopy can directly measure the amplitude and phase of the terahertz electric field, and the refractive index and absorption coefficient of the sample can be easily extracted. Comparing with the method to get the optical parameters using the Kramers-Kroning dispersion relation, the operation process is greatly simplified, and the uncertainty in the calculation can be reduced.
4. Low energy: The energy of typical terahertz photons is in the meV scale (~4 meV at 1 THz), about one-thousandth of the energy of X-ray photons (Hafez et al., 2016). The energy is much lower than the energy that can ionize bio-tissues. This is the reason why THz wave is called non-ionizing radiation, which makes terahertz has excellent potential in biological nondestructive detection and imaging (Jepsen et al., 2011; Lee et al., 2018).
5. Penetration: THz waves can pass through many materials such as polymers, paper, cloth, and dusty air. Thus, the perspective imaging of the concealed sample can thus be achieved. The X-ray imaging method with the strong transmission is caused by high photon energy, which leads to serious health problems. The terahertz technology successfully solves these problems.
6. Characteristic absorption of the spectrum: The phonon absorption of the condensed

system is mostly located in the terahertz band, and the free electrons also have strong absorption and scattering for the terahertz wave. Terahertz spectroscopy is a useful tool for studying the physical processes in condensed matter materials. In particular, many organic molecules exhibit strong absorption and dispersion characteristics in the terahertz electromagnetic band (Upadhya et al., 2003). Therefore, the THz technology can be used to detect the rotation dynamics of gas and liquid, the intermolecular bonding vibrations and hydrogen bonding network of liquids and solid materials, and the collective vibrations and lattice vibration of solid materials.

Although THz technology is relatively new, the significant progress of the research have gradually been applied in a wide range of applications such as environment inspection (Mittleman et al., 1998), public security scanners (Federici et al., 2005), manufacturing process (Pawar et al., 2013), wireless communication (Federici & Moeller, 2010, Kleine-Ostmann & Nagatsuma, 2011), and biomedical detection and imaging (Pickwell & Wallace, 2006).

3.2.2 Generation of THz radiation

At present, the THz radiation source can be roughly classified into three types: incoherent heat radiation sources, wide-band THz pulse sources, and narrow-band terahertz continuous wave sources. The primary THz pulse radiation is generated by different exciting materials using ultrafast pulses, including photoconductivity, optical rectification, plasma oscillation, and electronic nonlinear transmission lines. There are also many options for THz continuous radiation, including electronic RF up-conversion technology, optical frequency down-conversion, reverse-back-wave tubes, semiconductor lasers, and quantum cascade lasers, free electron lasers, *etc*. Here, we mainly introduce frequently-used solid state terahertz generation techniques.

1. Photoconductive emitter (PCAs)

The photoconductive dipole antenna is one of the most widely used terahertz pulse generators, which was first developed by Auston *et al.* in 1984 (Auston et al., 1984). The principle of generating and detecting THz radiation based on the photoconductive effect is showing in Figure 3-4 (Tani et al., 2006). When the femtosecond laser excites the bias semiconductor, and if the photon energy of the laser is higher than the energy bandgap of the semiconductor, electrons, and holes will be generated in the conduction band and the valence band, respectively. The carrier density changes rapidly and accelerates under the action of a biased DC (direct current) voltage, thereby forming electromagnetic radiation

and transmitting it through the antenna to free space. The femtosecond laser pulse acts as a pump light to excite a fast photoconductor to generate a transient current that propagates through the antenna to a short-period transient. The THz electric field is proportional to the time derivative of the transient current (Hafez et al., 2016).

$$E(t) \propto \frac{d\boldsymbol{J}}{dt}, \tag{3-2-1}$$

here **J** is the current density.

A photoconductive antenna device similar to the generator is required to detect the radiation, but this photoconductor does not need to be biased. This photoconductor is excited by the same femtosecond laser pulse, and the output current can be detected at the moment of excitation.

THz pulses generated from PCAs show strong asymmetry in the THz field, quasi-half-cycle nature, and relatively low central frequencies (Hafez et al., 2016). The main factors affecting the radiation include the effective mass of electrons in semiconductor materials, the lifetime of photogenerated carriers, the maximum mobility and the breakdown electric field of materials. In order to improve the response speed of photoconductive antenna, the usual photoconductive materials are mostly semiconductor materials with very short electron lifetime, such as gallium arsenide (GaAs) grown at low temperature or graphene-based metamaterials (Shen et al., 2004; Low & Avouris et al., 2014).

2. Optical rectification (OR)

The resonant light rectification is a second-order nonlinear process. The process of OR to generate femtosecond laser pulses is usually simple. In a nonlinear medium, the two monochromatic beams will be mixed to produce a sum frequency oscillation and difference frequency oscillation. When the femtosecond laser pulses interact with a nonlinear medium, the time-dependent nonlinear polarization proportional to the light intensity is obtained from two-photon difference frequencies, which can result in the emission of electromagnetic waves, as shown in Figure 3-5. The following formula describes the process

$$P(0) = \chi^{(2)}(\omega, -\omega, 0)E(\omega)E^{*}(-\omega), \tag{3-2-2}$$

where $\chi^{(2)}$ is the second-order susceptibility tensor of the medium.

In the time domain, the temporal THz field is proportional to the second derivative of the change of this polarization concerning time *t* (Hafez et al., 2016):

$$E_{THz}(t) \propto \frac{\partial^2 P^{(2)}(t)}{\partial t^2}. \quad (3\text{-}2\text{-}3)$$

This provides broad bandwidth THz pulses, and to date, it has turned into one of the most efficient approaches (Huang et al., 2013; Vicario et al., 2014), giving rise to extremely high THz pulse energies as well as high electric fields.

3. Free electron laser (FEL)

The physical-based of the FEL is basing on the interaction between the high-speed electron beam and the periodically swinging the magnetic field generated by wiggler or undulator, as shown in Figure 3-6 (O"Shea & P., 2001). The electrons are moving periodically and accelerated under the magnetic field. When the speed of electrons is close to the speed of light, those electrons generate terahertz waves through spontaneous radiation with the Lorentz force.

The radiation frequency of the FEL can be adjusted by the energy of the incoming electron, which covers the frequency from the far-infrared to the X-ray. The FEL is characterized by high regulation, high energy, high efficiency, and excellent beam quality. However, FEL is expensive and bulky, which is not suitable for practical application.

4. Quantum cascade laser (QCL)

QCLs are compact semi-conductor sources based on the electronic transition between subbands of the conduction band in semiconductor quantum well. The injected electrons undergo multiple lasing transitions by "cascading" a series of such stages together---superlattice, as shown in Figure 3-7 (Köhler et al., 2002). Differing from the traditional p-n junction semiconductor laser whose emission wavelength is determined by the semiconductor energy gap, the QCL is a unipolar laser with only electron-involved, and the lasing wavelength depends on the energy level difference of two excited states determined by the quantum confinement effect.

The THz QCLs can obtain a sizeable optical power output (up to multi-Watt.) by appropriately increasing the number of series stages of the active region. At the same time, the THz QCLs have excellent performance in energy conversion efficiency, broad-band, and continuous-wave generation and integration and far-field emerging (Vitiello et al., 2015). One crucial challenge to QCL is to increase the operating temperature. In some commercial QCLs, a Sterling cooler is applied to maintain the temperature but expensive. The next development may focus on increasing the operating temperature at a low cost.

5. Intrinsic Josephson junction (IJJ) stacks

The Josephson junction consists of two superconductors sandwiched between very thin barrier layers that can be either typical metal or an insulator. The type of high temperature superconductor Josephson junction is quite different from that of traditional superconductors. At present, the high temperature superconducting Josephson junction at present basically has wood grain boundary Josephson junction (GBJ), also called intrinsic Josephson junction (IJJ) (Gross et al., 1997).

The IJJ is an ideal voltage-frequency converter. When a finite dc voltage V is applied to both ends of the Josephson junction, the interior of the junction produces an oscillating Josephson current with a frequency $f = 2eV/\hbar$, where e is the charge constant, which is called the ac Josephson effect (Ozyuzer et al., 2007). Specifically, 1 mV dc voltage corresponding to 484 GHz oscillation frequency. Therefore, under special conditions, the intrinsic Josephson junction can emit electromagnetic waves with wave frequency in the THz region. The operating frequency band of Josephson junction using high energy gap superconducting materials such as NbN or NB-TiN as electrode materials or tuned circuit materials can be extended to 1 - 2 THz.

In 2008, Kadowaki *et al.* succeeded in emitting electromagnetic waves in the continuous THz frequency band using a mesa structure (width 80 m× length 300 m× thickness 1 m or so) of $Bi_2Sr_2CaCu_2O_{8+\delta}$ (BSCCO) single crystal, as shown in Figure 3-8 (Kadowaki et al., 2008). The crystal structure of BSCCO single crystal is shown in Figure 3-9, in which the CuO layer with a thickness of about 0.3 nm is the superconducting layer, and the adjacent CuO layer is sandwiched between the insulated SrO layer and the BiO layer with a thickness of about 1.2 nm. Therefore, the superconducting-insulated-superconducting Josephson junction with a thickness of 1.535nm is naturally formed in the single crystal of BSCCO.

3.2.3 Detection of THz radiation

1. Photoconductive detection

The photoconductive antenna is based on the inverse process of the photoconductive radiation mechanism, as described in section 2.2.2. A PCA detector without a bias voltage is placed on the pulsed optical path, while the femtosecond probes laser pulse generated by the femtosecond laser. Since the pulse width of the probe light is much shorter than the pulse width of the incident signal, the pulse can be sampled by adjusting the time delay of the two pulses, as shown in Figure 3-4. The THz field to be measured accelerates the carriers, leading to a transient photocurrent inside the PCA detector. The measured photocurrent $I(t)$ is proportional to the incident THz electric field,

$$I(t) \propto \int_{-\infty}^{t} \sigma_s(t-t') E_{\mathrm{THz}}(t') dt, \quad (3\text{-}2\text{-}3)$$

$\sigma_s(t)$ is the transient surface conductivity (Lee, 2009). The equation (3-2-3) implies that the measured $I(t)$ also be affected by the semiconductor substrate. Former researches demonstrated that materials with short carrier lifetime (such as low-temperature grown GaAs and doped GaAs) are more suitable for PCA detector (Kono et al., 2001; Zhang et al., 2004; Singh et al., 2015).

2. Free space electro-optic (EO) sampling

Free space EO sampling is based on the linear EO effect in an electro-optic crystal with a femtosecond pulse. The linear electro-optic effect, also known as the Pockels effect, is the phenomenon that the refractive index of an EO crystal changes in proportion to the applied electric field. The birefringence generated in the crystal deflects the polarization direction of the detection pulse. The intensity detected by the photodetector is proportional to the field strength of the pulse. Since the pulse width of the pulse is much larger than the pulse width of the probe laser pulse, the electric field can be approximated as a DC bias electric field. Therefore, by changing the time delay between the pulse and the light detection pulse, the entire time waveform of the pulse can be obtained. A typical schematic diagram of free space EO sampling is shown in Figure 3-10 (Hafez et al., 2016).

3. Mixer and difference in frequency detection

The mixer is a non-linear electronic component that directly detects radiation and is a non-coherent measurement with low sensitivity. However, its primary application method is to combine the local oscillator to perform the different frequency measurement, which dramatically improves the detection sensitivity and also provides the phase information. The difference frequency measuring apparatus requires a local oscillator which generates a single-frequency electromagnetic wave which is close to the frequency of the signal to be measured and is called a reference wave. The signal to be tested and the reference wave are simultaneously frequency-divided by the mixer to generate an intermediate frequency wave. Compared with the signal to be tested, the frequency of the intermediate frequency wave is relatively low, and it is easy to be processed and amplified by an electronic method. The intermediate frequency wave is filtered by a filter of a specific frequency and then amplified to obtain a specific frequency. Since the difference frequency measurement has the property of bandpass filtering. Therefore, it can be used to measure the spectrum and achieve very high sensitivity. Its noise equivalent power can reach 10, much higher than the direct detector.

3.2.4 Application of THz technology

Each molecule has a specific vibration and rotational energy level. Usually, the vibration absorption frequency of intramolecular chemical bonds is mainly in the ordinary infrared band. However, for weak interactions between molecules such as hydrogen bonds, the vibrational configuration of macromolecular vibrations, the rotation and vibration transitions of dipoles, and the low-frequency vibration absorption frequencies of the characters in the body correspond to the infrared range, which is reflected by these vibrations. The molecular structure and related environmental information appear as different absorption peak positions or intensity of absorption peaks in the band. These spectral characteristics of organic molecules make it possible to identify the influence of compound structure, configuration, and environment on its state by using time-domain spectroscopy.

1. Application in biomacromolecule detection

Since the spacing between the rotational and vibrational energy levels of a large number of biological macromolecules are within the range of the frequency band, the resonance absorption peak can be effectively formed when the biological sample is analyzed, thereby making it possible to provide a kind of fingerprint spectrum for the biological sample. In addition, the pump-detection technique enables dynamic analysis of processes such as conformational changes that occur in specific physiological processes or other interactions, such as proteins, which are easily denatured by proteins, by time-resolved spectral analysis. The high degree of correlation between the overall structure of biomolecules and their spectral properties in the band is an essential microscopic basis for the application of this emerging technology to biological systems.

2. Application in medical diagnose and imaging

The THz photons do not produce harmful photoionization to living biological tissues, and can penetrate into many materials such as plastics, wood, paper, but cannot go through metals, water, *etc*. Although biological tissues absorb rather substantial, the contrast of intensity may be obtained from different organs. Therefore, wave imaging technology can be an effective means of medical examination. When the wave passes through the cancerous tissue and the healthy tissue, it has a different amplitude, waveform, and time delay. By imaging the human tissue and organs, the size and shape of the tumor can be obtained from it, and then the tumor can be diagnosed early.

3. Application in environmental monitoring

All or part of the rotational spectrum of the gas molecules is located in the far-infrared region. The continuous spectrum is unique in gas spectroscopy and can directly measure the rotational spectrum of the molecule. Water, oxygen, nitrides, chlorides, *etc*. in the atmosphere can radiate frequencies in between, so the wave detectors carried by satellites can monitor the content and distribution of these gases in the atmosphere, thus providing a global climate. World-wide environmental problems such as warming and destruction of the ozone layer provide a large amount of data and information.

4. Application in the security check

Compared to infrared, terahertz waves have unique advantages in the properties of propagation, scattering, absorption, and transmission. For example, THz waves have many non-polar materials with excellent penetrability (such as paper, clothes, and plastics, *etc.*), which can detect hidden contraband; THz spectroscopy has a higher resolution than the microwave. It is particularly sensitive to drugs, chemicals, and biological agents, enabling low-dose detection and imaging. Compared with X-rays, terahertz photons have low energy and do not cause ionization of biological tissues. They are suitable for safety checks in public places like airports and stations.

5. Application in military and communications

The application of terahertz in communication has been highly valued by relevant parties, such as inter-satellite communication, short-range atmospheric communication, short-range terrestrial wireless local area network. International projects are being researched and applied, such as EU cooperation project money. Wave is an excellent broadband information carrier. It has much more bandwidth and channel than the microwave. It is especially suitable for broadband wireless communication between satellites, satellites, and local area networks. The frequency band already designated by the International Communication Alliance is the next particular frequency band for inter-satellite communication. Further development must enter the high range--THz communication.

The wireless transmission speed available for communication, which is hundreds of times to thousands of times faster than current ultra-wideband technology, and it has both high directivity and intense cloud penetration compared to visible and infrared. Communication can perform high-secure satellite communications with extremely high bandwidth. From a technical point of view, radar technology can detect smaller targets and achieve more accurate positioning than microwave radar. The former has higher resolution and greater confidentiality so that radar can become the development direction of the high-precision radar in the future. It plays a huge role in military equipment and

national security.

Terahertz electromagnetic waves have excellent application prospects in network communication. The frequency of the terahertz wave is about twice the communication frequency of the mobile phone. The use of terahertz waves for radio communication can significantly widen the frequency band of the radio communication network, making the wireless mobile high-speed information network into a reality.

6. Application in astronomy

THz technology is an essential tool for astrophysics and cosmology research. THz radiation accounts for a significant proportion of observable galaxies. Most of these radiation comes from low-temperature cosmic dust and older galaxies. In the space, interstellar dust clouds emit about 4000 kinds of spectral lines. Most of the spectral lines are in the THz band. Now only about a few thousand kinds of lines have been identified, and more lines need further study. The National Radio Astronomy Observatory and several international organizations plan to collaborate to establish a 1.5 THz terrestrial radio telescope for astronomical observations. Small wave space detectors can be used for the detection of asteroids and comets. The European Space Agency plans to launch a satellite that will carry a 562 GHz wave detector to observe the water vapor and carbides in the head and tail of the comet.

3.3 Terahertz time-domain spectroscopy (THz-TDS)

3.3.1 The principle of THz-TDS

The terahertz time-domain spectroscopy (THz-TDs) is the most commonly used and instrumental coherent non-invasive detection technology first developed by Smith et al. in the 1980s (Dhillon2017). It has a high signal-to-noise ratio, high time resolution, high bandwidth, and high frequency, high sensitivity, and the ability to work at room temperature. The THz-TDs can directly obtain amplitude and phase information of a variety of materials without using the Kramer-Kronig relation, such as biological tissue, dielectric materials, semiconductors, gases, and superconducting materials (Walther et al., 2010; Lee et al., 2018). Therefore, THz-TDs can provide more sample information than Fourier transform spectroscopy.

The THz-TDS we used in this study is the RT-10000 manufactured by Tochigi Nikon Corporation. The configuration of the optical system of the apparatus is as shown in

Figure 3-11. As shown in the figure, the THz-TDS system consists of four parts:a femtosecond laser, a THz wave emitter, a THz wave detector, and a time delay controller for adjusting the time delay between generation pulse and detection pulse.

Photoconductive antennas using low-temperature grown GaAs are used for the terahertz light emitter and detector. The Mai Tai of Spectra-Physics, a femtosecond titanium sapphire laser, is used as an antenna excitation laser. The relative parameters applied in this laser are as following: the center wavelength of the optical pulse is 780 nm, the pulse width is 100 fs or less, the repetition frequency is 80 MHz, and the measurement range is approximately 0.2 to 4.5 THz (Terao, Master's thesis, 2019). The laser generated by the femtosecond laser is split into two lights: pump light and probe light by a beam splitter. The pump light is incident on the terahertz emitter to generate THz radiation. The emitted terahertz wave goes through a sample or reference sample and arrives at the THz detector. The THz detector is excited by probe light.

The time waveform of the electric field of the transmitted terahertz pulse wave can be obtained by moving the delay stage and measuring the instantaneous current at each point while shifting the timing at which the probe light reaches the detection antenna. The process of timing waveform detection is shown in Figure 3-12.

3.3.2 Reflection and Transmission

When light perpendicularly goes through from one medium 0 (free space) into another medium 1, both reflection and transmission will happen to the propagation light, as shown in Figure 3-13. These phenomena can be described by the reflection coefficient r and transmission coefficient t, which can be calculated by Fresnel equations:

$$r \equiv \frac{E_r}{E_i} = \frac{\tilde{n}_0 - \tilde{n}_1}{\tilde{n}_0 + \tilde{n}_1}, \tag{3-3-1}$$

$$t \equiv \frac{E_t}{E_i} = \frac{\widetilde{2n}_0}{\tilde{n}_0 + \tilde{n}_1}, \tag{3-3-2}$$

where E_i, E_r, and E_t are the amplitudes of the incident, reflected and transmitted light, respectively. $\tilde{n}_0$ and $\tilde{n}_1$ are refractive indexes of medium 0 and medium 1, respectively.

Then, the energy reflection is defined as reflectivity R,

$$R = r \cdot r^* = |r|^2. \tag{3-3-3}$$

Because the medium 0 is free space, $n_0 = 1$ and $k_0 = 0$. In this condition, the R can be

described by

$$R = \frac{(n-1)^2+k^2}{(n+1)^2+k^2}. \quad (3\text{-}3\text{-}4)$$

Inside the matter, the multiple reflections rather than a single reflection happens, as shown in Figure 3-14. The thickness of the medium 1 is given by *d*. The phase difference 2δ between the reflected light by the surface of the medium 1 and that by the backside, is given by,

$$2\delta = 2\frac{2\pi}{\lambda}\tilde{n}d = \frac{4\pi}{\lambda}(n+ik)d = \frac{2\pi}{c}\tilde{n}d. \quad (3\text{-}3\text{-}5)$$

The summation can calculate the multiple reflection coefficient *r* for the amplitude of the reflected light overall reflected light. By using the relationships $r_1' = -r_1$ and $t_1 \cdot t_1' = 1 - r_1^2$, we have,

$$r = r_1 + t_1 r_2 t_1' e^{2i\delta} + (t_1 r_2 t_1')(r_1' r_2)e^{4i\delta} + (t_1 r_2 t_1')(r_1' r_2)e^{6i\delta} \ldots\ldots = \frac{r_1 + r_2 e^{2i\delta}}{1 + r_1 r_2 e^{2i\delta}}. \quad (3\text{-}3\text{-}6)$$

Similarly, the multiple transmitted coefficient *t* can be given by,

$$t = t_1 t_2 e^{i\delta} + t_1 t_2 (r_1' r_2)e^{3i\delta} + t_1 t_2 (r_1' r_2)e^{5i\delta} + t_1 t_2 (r_1' r_2)e^{7i\delta} + \cdots \ldots = \frac{t_1 t_2 e^{i\delta}}{1+r_1 r_2 e^{2i\delta}} = \frac{(1-r_1^2)e^{i\delta}}{1+r_1 r_2}. \quad (3\text{-}3\text{-}7)$$

The reflectivity *R* can also be calculated by equation (3-3-2). With R, we obtain the transmissivity T by following equation (3-3-7):

$$\mathrm{T} = 1 - \mathrm{R}. \quad (3\text{-}3\text{-}8)$$

3.3.3 Transmission spectroscopy

One of the essential features of the THz-TDS is that a wave shape of a THz pulse can be directly measured in the time domain, and then information on amplitude and phase can be obtained by Fourier transform of a THz pulse measured. While only information on amplitude is measurable in a conventional Infrared (IR) spectroscopy, both information on amplitude and phase are obtained in the THz-TDS.

In the transmission measurement of the THz-TDS, a THz pulse single $E_{ref}(t)$ without a sample and that $E_{sample}(t)$ with a sample is measured. The Fourier transform of $E(t)$ is described by,

$$E(\omega) = \int_{-\infty}^{\infty} E(t) \cdot \exp(i\omega t)\, dt = |E(\omega)| \exp\big(i\theta(\omega)\big). \qquad (3\text{-}3\text{-}9)$$

The complex transmission coefficient $t(\omega)$ is, then, calculated using the information on amplitude and phase:

$$t(\omega) = \frac{E_{sample}(\omega)}{E_{ref}(\omega)} = \frac{|E_{sample}(\omega)|}{|E_{ref}(\omega)|} \cdot \exp\big[i \cdot \{\theta_{smaple}(\omega) - \theta_{ref}(\omega)\}\big] \equiv \bar{t} \cdot \exp(i\theta). \qquad (3\text{-}3\text{-}10)$$

On the other hand, the theoretical transmission coefficient $t_{theory}(\omega)$ is described by,

$$t_{theory}(\omega) = \frac{E_{sample}(\omega)}{E_{ref}(\omega)} = \frac{4\tilde{n}}{(1+\tilde{n})^2} \exp\left[i\frac{(1-\tilde{n})\omega}{c} d\right] = \frac{4(n+ik)}{(1+n+ik)^2} \exp\left[i\frac{(n-1)\omega}{c} d\right] \cdot \exp\left(-\frac{k\omega}{c} d\right). \qquad (3\text{-}3\text{-}11)$$

where d is the thickness of a sample and $\tilde{n}$ is the complex refractive index. The equation (3-3-11) is derived based on the assumption that multiple refractions of a THz pulse wave do not take place. On the other hand, by considering the multiple refractions, the equation (3-3-11) becomes

$$t_{theory}(\omega) = \frac{E_{sample}(\omega)}{E_{ref}(\omega)} = \frac{4\tilde{n}}{(1+\tilde{n})^2} \cdot \frac{\exp\left\{i\frac{(\tilde{n}-1)\omega}{c} d\right\}}{1 - \frac{(\tilde{n}-1)^2}{(\tilde{n}+1)^2} \exp\left(i\frac{2\tilde{n}\omega}{c} d\right)}. \qquad (3\text{-}3\text{-}12)$$

In an experiment, the $\tilde{n}$ can be calculated from the experimental $t(\omega)$ in such a way that $t(\omega)$ is fitted by the $t_{theory}(\omega)$ (equation 3-3-11 or 3-3-12), as $\tilde{n}$ is a fitting parameter using a non-linear least square algorithm.

Then, a real $n(\omega)$ and imaginary part $k(\omega)$ of a complex refractive index $\tilde{n}(\omega)$ are obtained by comparing $t'(\omega)$ with $t'_{theory}(\omega)$:

$$n(\omega) = \frac{c}{\omega \cdot \Delta d}\theta(\omega) + 1, \qquad (3\text{-}3\text{-}13)$$

and

$$k(\omega) = -\frac{c}{\omega \cdot \Delta d} ln\tilde{t}. \qquad (3\text{-}3\text{-}14)$$

Finally, a real $\varepsilon'(\omega)$ and imaginary $\varepsilon''(\omega)$ part of a complex dielectric constant are calculated:

$$\varepsilon'(\omega) = n(\omega)^2 - k(\omega)^2,$$
$$\varepsilon''(\omega) = 2 \cdot n(\omega) \cdot k(\omega). \qquad (3\text{-}3\text{-}15)$$

This method is a powerful way to calculate a complex dielectric constant in the THz-TDS because it is not required a complicated numerical fitting procedure such as a non-linear least square method.

Figures

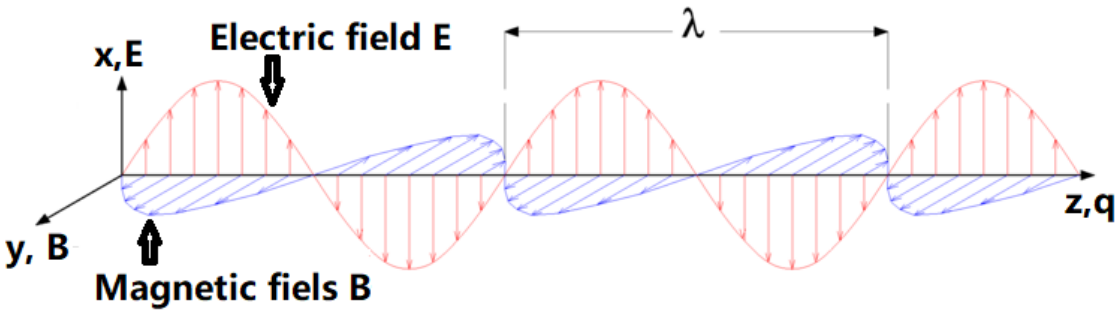

Figure 3-1 The propagation of linearly polarized electromagnetic waves with a wavelength of λ (z-axis). The propagation wavevector q (z-axis), the electric field **E** (x-axis), and the magnetic induction **B** (y-axis) are perpendicular to each other (Dressel & Grüner , 2002).

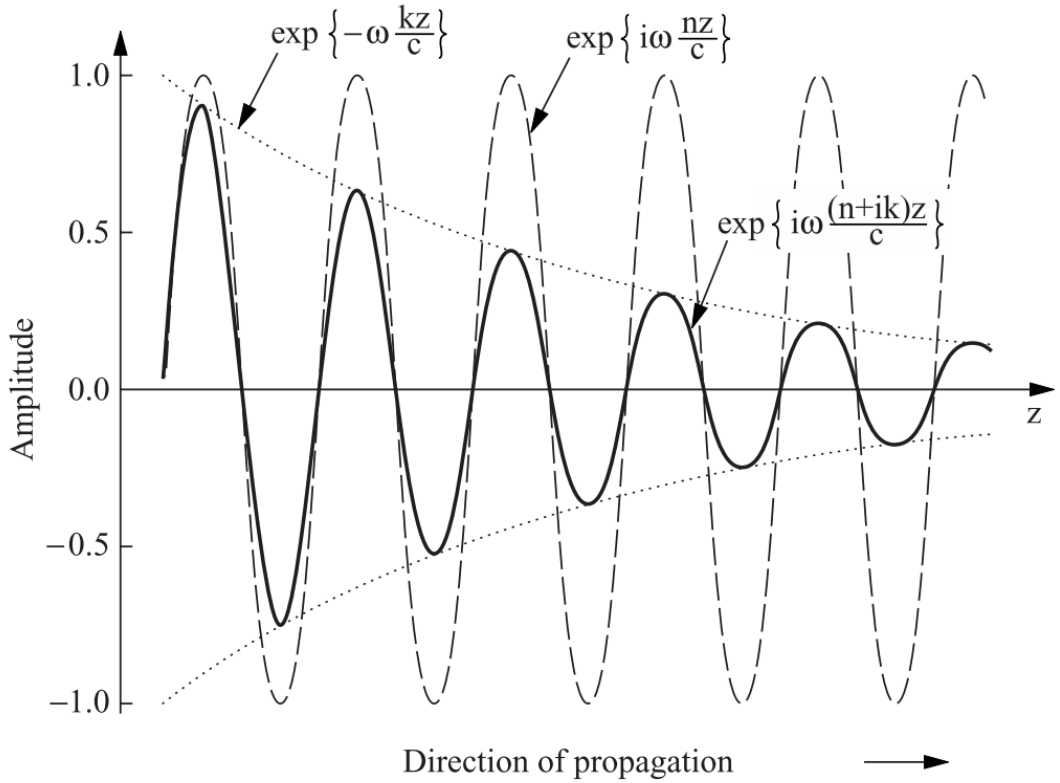

Figure 3-2 Spatial dependence of the amplitude of a damped wave as described by equation (3-1-27) (Dressel & Grüner , 2002).

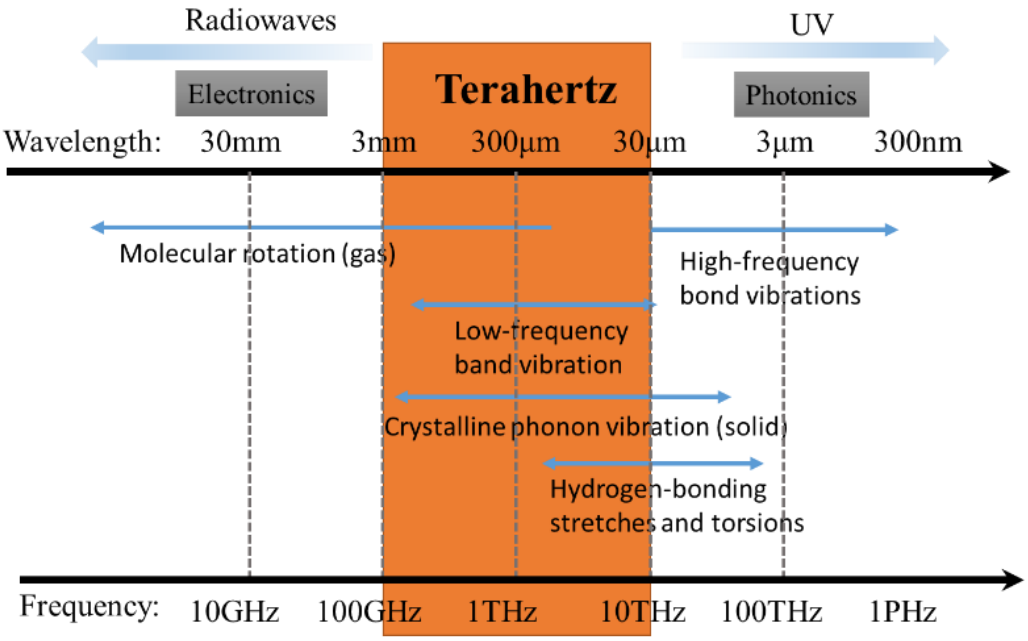

Figure 3-3 THz spectrum.

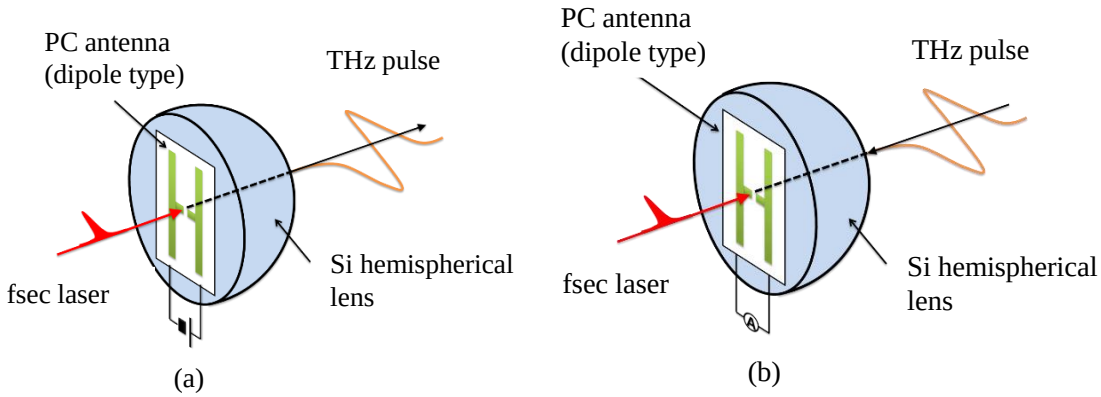

Figure 3-4 Photoconductive emitter (a) and photoconductive detector antenna (b) mounted on a hemispherical lens (Shibata, Master's thesis, 2015).

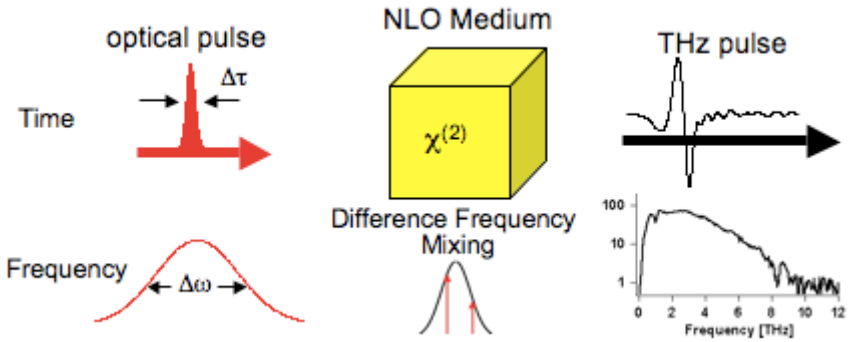

Figure 3-5 Schematic representation of optical rectification by difference frequency generation in non-linear crystal for the generation of THz [Source: https://cassandrahunt.com/research/THz_spectroscopy].

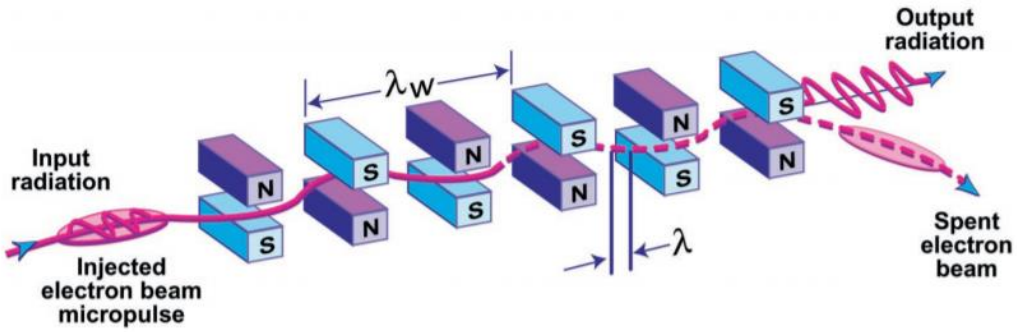

Figure 3-6 Schematic illustration of the interaction between the electron beam and the wiggler in an FEL with a planar wiggler (O'Shea, & P., 2001).

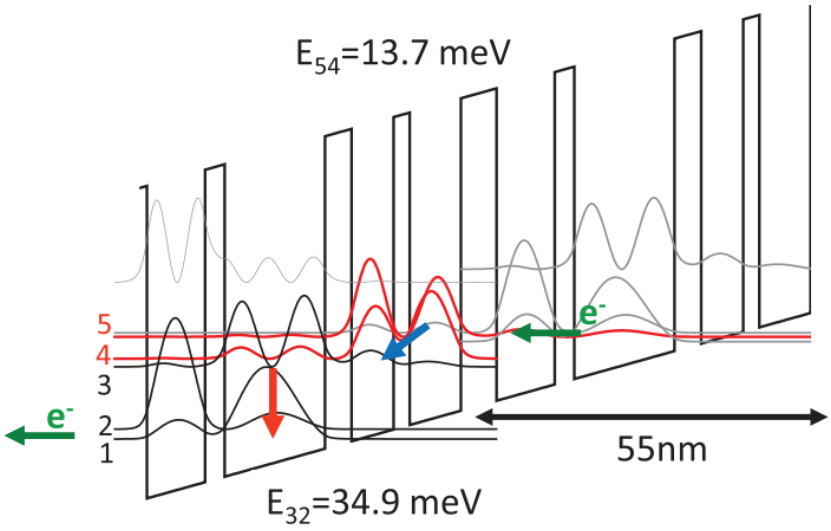

Figure 3-7 Bandstructure of two periods of a LO phonon depopulation-based QCL active region for emission at 3.3 THz (13.7 meV, electronic states 5 and 4) (Dhillon et al., 2017).

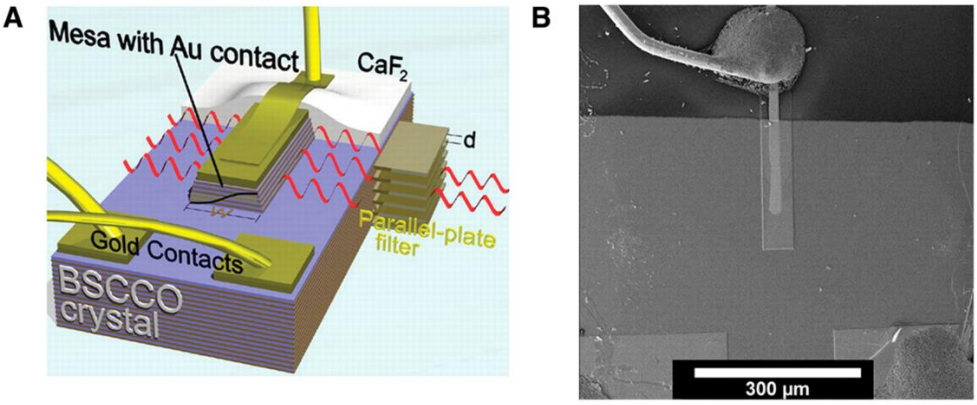

Figure 3-8 Schematic of the BSCCO mesas (a) and scanning electron microscope image of the mesa (b) (Ozyuzer et al., 2007).

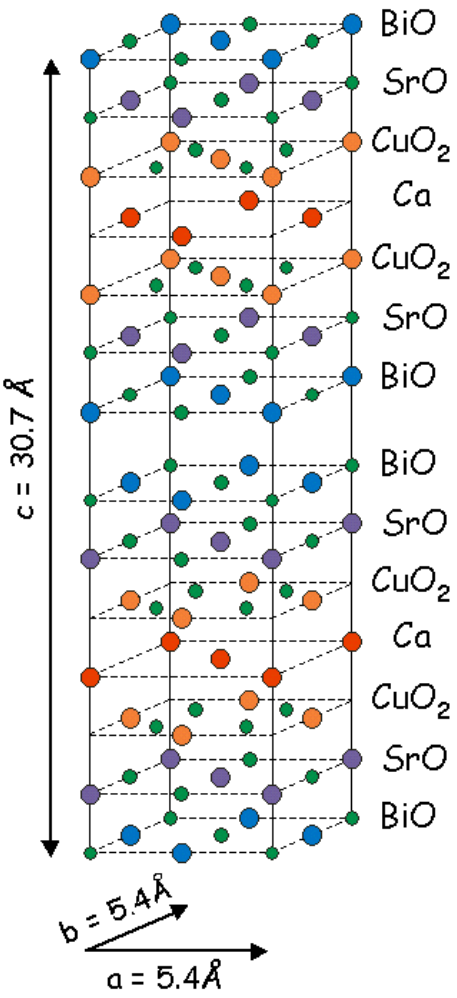

Figure 3-9 Schematic of the BSCCO.
[http://hoffman.physics.harvard.edu/materials/CuprateIntro.php]

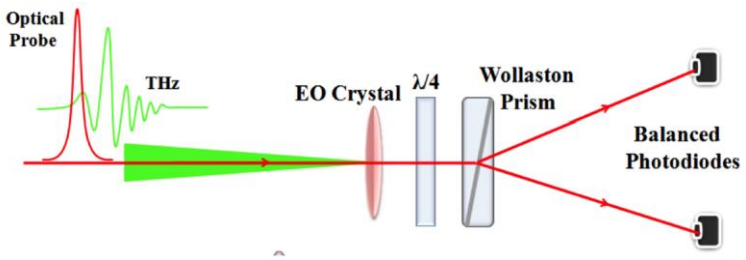

Figure 3-10 THz detection using the EO sampling technique (Hafez et al., 2016).

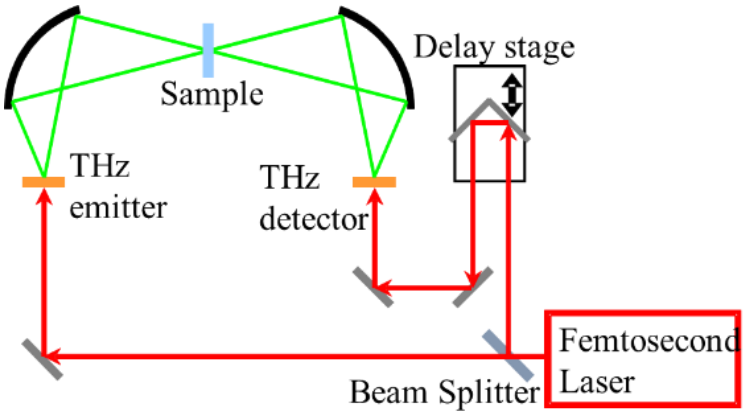

Figure 3-11 Schematic diagram of RT-10000 (Terao, Master's thesis, 2019).

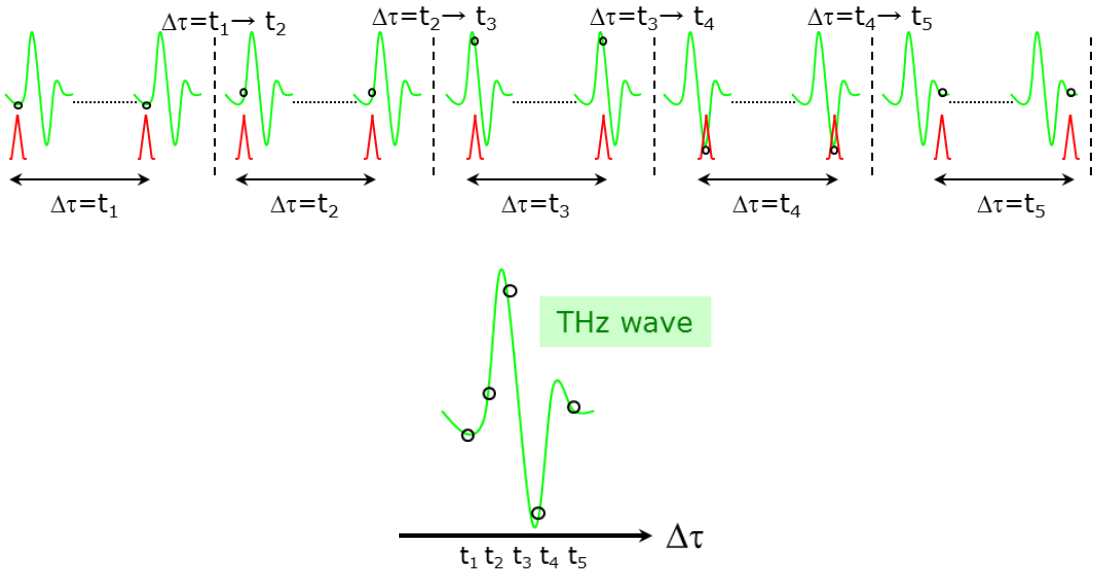

Figure 3-12 The process for timing waveform detection (Terao, Master's thesis, 2019).

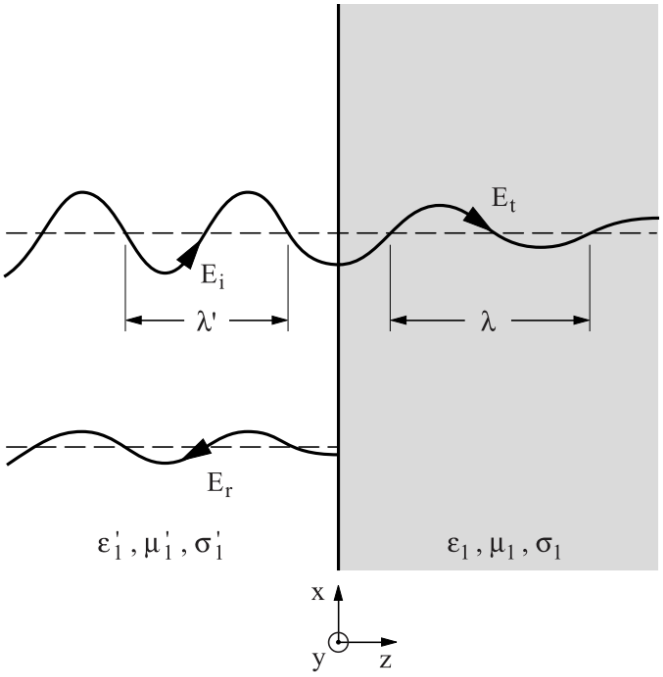

Figure 3-13 Incident E_i, reflected E_r and transmitted electric wave Et traveling normal to the interface between two media (Dressel & Grüner , 2002)..

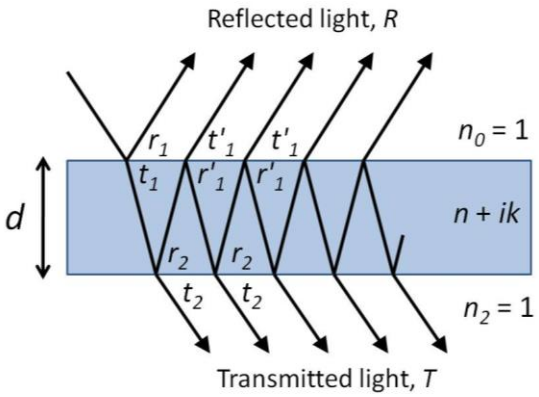

Figure 3-14 Multi-pass reflection of light between mediums (Matsuda, Doctoral thesis, 2010).

Chapter 4 Experimental section

4.1 Algae culture

4.1.1 Algae culture

In our experiment, two strains of algae, botryococcus braunii (BOT22) and monoraphidium (A11) were cultured in nalgen bottle with 9 L culture mediums, as shown in Figure 4-1. The BOT22 were cultured at room temperature with CO_2 (5% mixed with air) flow speed of 2 L/min. The medium used in BOT22 culture is called Radish Sprout Medium, with several nutritions.

To make Radish Sprout Medium, we pour 10 L of RO (Reverse Osmosis) water into a nalgene bottle. Use stirrer and put in the materials listed in Table 4-1 to the bottle and make sure all materials are completely dissolved into water. Cover the cap of the bottle with aluminum paper and stick a particular type on the aluminum paper. Then leave 1~2 hours for mixing with a stirrer. The transfer of medium should be done in the glove box to prevent infection of botryococcus.

The A11 was cultured at room temperature in the nalgene bottle with CO_2 (5% mixed with air) flow speed of 2 L/min. The medium used in A11 culture is called AF-6 medium with several nutritions as showing in Table 4-2. 250 g of glucose and 25 g of BACTO yeast extract were added in 10 L of AF6 medium.
The algae of Euglena gracilis EOD-1 was cultured by NEC Corporation, Japan. The culture medium is the same as that of the A11. The EOD-1 was cultured at room temperature and in dark condition, in the nalgene bottle with CO_2 (5% mixed with air) flow speed of 4 L/min. The culture period is two weeks.

4.1.2 Algae sampling

Algae sampling was done every Monday and Friday, and the harvest was done every two weeks. In our sampling, the value of DCW (dry cell weight), pH, QY (photosynthesis active), and OD680 (optical density at 680 nm). And we added the same volume of culture medium with the harvested volume of algae after every harvest.

DCW is a parameter to record the cell mass of algae. 5 ml of algae medium is filtered by

a filter paper. Then, the paper is dried by the oven, and the weight difference is recorded. QY is recording photosynthesis active by Fluorpen, which reflects photosynthesis efficiently. In this measurement, 100 µl of algae medium is diluted with water and full with the cuvette inside Fluorpen. Wait for 1 min before measurement.
OD680 measures the density of the algae at 680 nm wavelength, which also known as the optical absorption value. This absorption is mainly due to the presence of chlorophyll in algae cells, and the cell density and biomass can be roughly estimated through OD680.

Figure 4-2 shows the micro-morphology of BOT22 cell and A11 cell aggregation. As we can see from the photos, that the cells are all growing healthy so that they look to keep good cell shape and color.

4.1.3 Algae harvest

We used $Al_2(SO_3)_4$ for flocculation (1 g/L or 0.5 g/L). After half an hour, algae will flocculate. When we dewater the algae by plankton mesh with an aperture of 25 µm. The algae will transform into the holder after dewatered, as showing in Figure 4-3. The put into the oven for dry. The dried biomasses were storied in the refrigerator.

For A11, we harvested 8 times. We harvested 6 L every time. At the end of this culture, we harvested all algae of 9 L and kept the biomass in a z-plastic bag as a wet state. We also keep 45 ml of culturing algae.

For BOT22, the growth was slower than monorahidium A11. Therefore, we just harvest four times in a three-month culture. In addition, the flocculation of the BOT22 was harder than that of monorahidium A11. The algae medium would become sticky when the chemical component was added in which is hard to go through the 25-µm mash. Thus, we got a litter amount of biomass in this BOT22 culture. In the final harvest, the flocculation was a success, and we got a considerable amount of wet algal biomass. Again, we keep all biomass and 45 ml of culture algae medium. All samples are stored in a refrigerator.

4.1.4 Lipid extraction

In this part, we will try three different extraction methods to determine the best extraction method, which can get a high quality of lipid with high purity.

Firstly, 50 g of smashed dry biomass of monoraphydium was put into the conical beaker.

The algae powder samples were diluted with three different solvents with a ratio of 1:4 (weight/weight), as shown in Table 4-3, and put on a shaker with a speed of 50 rpm/min for 2 days.
After the two-day shake, the algae-solvent mixture was filtered by ADVANTEC filter paper with 185 mm. aperture. Then the filtered liquid was put into a Rotation vapor to remove the solvent. The bath temperature was set to 60 °C, and the pressure was 360-370 mbar. The filter paper was washed by diluted solvent for three times. Then we got crude oil. The last step was to wash crude oil by 30 chloroform with 40 °C temperature on EYELA MG-2200 machine.

In the filter process, Batch II showed the fastest filtrate by comparison within Batch.I and Batch III. There is a considerable amount of particle in Batch III algae-solvent mixture in the filtrating process, where blocked on the filter paper was blocked and stopped solvent would not go through. Therefore, Batch III took the longest time in the filtration process, and the filtered solvent contained lots of particles.

4.2 Sample preparation

4.2.1 Extraction of paramylon

In the THz spectra measurement, ten samples were prepared; they are one glucose, one cellulose, four paramylons (P1-P4), and four paramylon ester (PE1-PE4) samples. The paramylon (P4), glucose and cellulose were purchased from Wako Pure Chemicals (Tokyo, Japan).

Paramylon samples (P1-P3) were extracted from cells of *Euglena gracilis EOD-1* in the collective project of the Algae Biomass Energy System (ABES) Research, University of Tsukuba, and Development Center and NEC Corporation, Japan. The detailed process as follows: the harvested biomass of *Euglena* was dispersed in acetone and filtered by vacuum filtration to separate paramylon from other components. Then, the separated rough paramylon was treated at 90 ℃ for 10 minutes, with 1% sodium dodecyl sulfate (SDS) solution to remove the residual proteins. Paramylon was obtained after further centrifugation and repeated washing with 0.1% SDS solution and deionized water. Then the refined paramylon powder was obtained. Paramylon P4 was purchased for the comparative analysis. The gel permeation chromatography (GPC) was measured to get the molecular weights (MW) of those paramylon samples. All the measurements were carried out at 23°C using a polystyrene gel column (PLgel20μm MIXED-A, Polymer

Laboratories), and DMAc/LiCl (0.1 M) was used as an eluent at a flow rate of 0.5 mL/min. The detailed characteristics of paramylon samples are listed in Table 4-4.

4.2.2 Synthesis of paramylon ester

Paramylon esters (PE1-PE4) were synthesized from paramylon (P1) by a typical esterification method linking propionyl chloride and long-chain acid chloride sidechain into paramylon. The reaction process is shown in Figure 4-4. The detailed processes of synthesis were as follows. In the case of PE1 synthesis, the paramylon powder 4.5 g (27.0 mmol per anhydrous glucose unit (AGU)) was stirred in N-methyl pyrrolidone (57.6 mL) and pyridine (8.0 mL) overnight under a dry nitrogen atmosphere, and in mixture of 7.48 g (80.9 mmol) of propionyl chloride, 1.35 g (4.92 mmol) of palmitoyl chloride and 1.78 g (5.88 mmol) of stearoyl chloride were slowly added to the solution at 7 ℃. The resulting solution was stirred at 90 °C for four hours under a dry nitrogen atmosphere. During stirring, the solution tended to be gelatinized and cleared. After methanol (66.0 mL) and deionized water (14.5 mL) were added to precipitate the products keeping in the environment with a temperature of 65 ℃. The synthesized paramylon ester was separated by vacuum filtration. The obtained products were stirred five times in methanol (87 mL) and deionized water (9.7 mL) at 45 °C for 0.5 hours to elute unreacted components and isolated by vacuum filtration each time. The purified product was obtained by drying in a vacuum for 5 hours at 105 °C. The other paramylon ester samples were prepared by the same method, but different content of chloride mixture and the details are listed in Table 4-5.

The parameter of the degree of substitution (DS) is utilized to describe the substitution level, and it is defined as the integration ratio of the number of the propionyl or long-chain protons to the number of –OH groups in the paramylon ring proton unit. There are three –OH groups in a ring proton unit; the value of DS is smaller than 3 or equal to 3. The degree of substitution (DS) of the paramylon-ester was determined by NMR spectroscopy. The values of DS_{Pr} (DS of propionyl) and DS_{Lo} (DS of long-chain protons) of the paramylon-esters and the total DS analyzed by nuclear magnetic resonance (NMR) are listed in Table 4-5.

4.2.3 Synthesis of CM-starch

The powder CM-starch sample was provided by AGH-University of Science and Technology, Poland. Natural starch is a semi-crystalline polymer with an amorphous

region and a crystalline region, and its crystallinity is reported to be about 20-60%, depending on the moisture content and the source plant of the starch. The microwave-treated CM-starch is an amorphous starch with a crystallinity of almost 0. The structure of CM-starch is shown in Figure 4-5. In CM-starch, the partial of hydroxyl groups of starch are substituted by ether substituents (-COONa groups), with DS < 0.7 (Kaczmarska et al., 2018). For measurement, the powder sample was press into a pellet with a diameter of 15 mm and a thickness of 1.010 mm using a press.

4.3 Experimental setup and measurement

4.3.1 X-ray diffraction spectra

The X-ray powder diffraction spectra were measured using a commercial PANalytical X'Pert (Rigaku Corp.) with CuKα radiation (λ = 0.1542 nm) generated at 30 kV and 10 mA, and the crystal structures of our samples were studied. The polycrystal samples as-synthesized were milled to sub-micron particles and placed into a thin quartz glass plate for the measurement. The diffraction intensities were recorded from 2θ = 5° to 70° with 5 s per step with an angular step of 0.02°. All measurements were performed at room temperature.

4.3.2 Fourier transform infrared (FT-IR) spectra

The FT-IR spectra using a standard FT-IR spectrometer (FT/IR-4600, JASCO, Japan) were measured at wavenumbers between 400 and 4,000 cm^{-1} with a resolution of 4 cm^{-1} at room temperature. The data acquisition was carried out using 1 cm^{-1} step increments. As for the preparation of solid-state samples, to reduce particle scattering, the pure samples were firstly ground into fine powder by pestle and agate mortar. Since the absorption is strong, the samples were diluted with potassium bromide (KBr). Finally, the samples were pressed into surface-smooth pellets.

4.3.3 THz spectroscopy

The THz spectra using a commercial FT-IR spectrometer (FARIS-1, JASCO, Japan) were measured at wavenumbers between 10 and 400 cm^{-1}. FARIS-1 is a hybrid Fourier spectrophotometer of Michelson type with high efficiency on the high wavenumber side and Martin Puplet type with high efficiency on the low wavenumber side. The structure diagram is shown in Figure 4-6 and the photo of this system is shown in Figure 4-7. In this system, the optical source is a high-pressure mercury lamp with a power of 180 W

and a voltage of 120 V, and a Si-bolometer is used as a detector at a liquid He temperature. A wide range of measurements from infrared to far-infrared and millimeter-wave regions is possible by merely exchanging optical elements and switching detectors. Step scan specifications and polarization modulation specifications are also available, leading the possibility to build a customized system for different research purposes.

The samples were pressed to tablets with a tablet presser with a pressure of 2 MPa for 2 minutes. The radius of the tablet is 10 mm, and the thickness is about 3 mm. All samples were recorded with a resolution of 0.25 cm^{-1}, and the measurement was repeated 16 times and averaged for each sample at room temperature under vacuum condition.

4.3.4 Temperature-dependence THz spectroscopy

The THz-TDS (RT-10000, Tochigi Nikon Co.) with low-temperature-grown GaAs photoconductive antennas has both the emitter and detector (Hamamatsu Photonics K.K.). The structure of the system is shown in Figure 4-8. The THz spectra covering the frequency range of 0.25-2.25 THz, were measured using the standard transmission configuration for the temperature-dependent measurements. The details were described in section 3.3. The temperature was varied from 13 to 300 K using a liquid helium flow cryostat system (Helitran LT-3B, Advanced Research Systems). During measurement, dry air is passed through the chamber to prevent the absorption of terahertz light by water. In this experiment, we made a thinner sample and a thicker sample for each measurement and connected the absorption coefficients of the thinner sample and the thicker sample to get clear and smooth data for analysis (Terao et al., 2018).

4.4 Sample evaluation

4.4.1 FT-IR spectroscopy

The IR spectroscopy has frequently been used to study the intramolecular bonding by vibrational dynamics in polysaccharides (Liang, & Marchessault, 1959; Ellis et al., 1940). In recent years, several works on the calculation of vibrational frequencies of mono- and disaccharides have been performed (Walther et al., 2003; Pearson et al., 1960; Upadhya et al., 2004; Sevilla & Fuertes, 2009). The IR technology may be able to distinguish different isomers of saccharides and obtain information concerning their detailed structure.

In Figure 4-9, we present the FT-IR data of Paramylon (P1) and paramylon ester (PE1) in

the frequency range between 400 and 4,000 cm^{-1} (corresponding to 13.2 and 132 THz, respectively) measured at room temperature in order to check the quality of the sample. The red curve in Figure 4-9 is for paramylon, whereas the dark blue curve corresponds to the data of paramylon ester. An exciting feature observed here is first that a strong but rather broad absorption peak intensity centered at 3400 cm^{-1} in P1 is significantly reduced in PE1. Secondly, a sharp and strong absorption peak appears at 1750 cm^{-1} in PE1, and thirdly absorption peaks at 1050 and 1400 cm^{-1} in PE1 split into two lines each other remaining one of them to the original frequency and the others shift up about 100 cm^{-1} to the higher frequency at 1400 cm^{-1}. Similar splitting in PE1 is also found in the absorption line at 2940 cm^{-1}.

Since the characteristic stretching mode frequency of -OH bound is known to lie around 3400 cm^{-1} regions, the huge absorption peak at 3400 cm^{-1} for paramylon P1 can be interpreted by the -OH stretching mode frequency of -the OH bond of glucans. Therefore, the intensity of this mode is significantly reduced in paramylon ester because the –OH groups were removed by esterification. This proves the success in introducing the acid chloride side chains into paramylon ester. The success also is proved by the appearance of a peak at 1750 cm^{-1} for paramylon ester, which indicts the –C=O stretching that only existing in acid chlorides. The absorption after splitting at around 1100 cm^{-1} may be assigned to be the stretching mode of the ester group (C–O). Slight increase of the peak intensity at 2800-2900 cm^{-1} may be related to the additional antisymmetric and symmetric stretching modes of $–CH_2$ and $–CH_3$. The details are showing in Table 4-6.

4.4.2 X-ray diffraction (XRD) spectra

Powder XRD patterns for cellulose, paramylon (P1), and paramylon ester (PE1) samples are shown in Figures 4-10 and 4-11. In the paramylon XRD spectrum as shown by the red line in Figure 4-10, four distinguished and sharp peaks were observed at $2\theta \approx 7°$, 19.5°, 21°, and 24°. They were assigned to be the 100, 111, 210, and 121 plane reflections of paramylon crystal, as indicated by red arrows in Figure 4-10 (Kawahara, 2014).
In addition, at least three small peaks in 2θ between 12° and 18° (marked by green circles) were visible in our data of paramylons. I would like to point out that these three small peaks can also be found in the data shown in Fig. 6 of Kawahara's paper (Kawahara, 2014).

In contrast, to the paramylon spectra of the powder XRD patterns for paramylon ester showed two broad peaks at $2\theta \approx 8.7°$ and $2\theta \approx 20.4°$, as shown by the black line in Figure

4-10. The occurrence of broad peaks can be attributed to the esterification of paramylon and transformation of its crystalline structure to a more disordered amorphous material. The peak at $2\theta \approx 8.7°$ for paramylon ester is originated from some factor with the peak $2\theta \approx 7°$ for paramylon. The shift is because of the esterification that caused the disordered structure of paramylon ester.

On the other hand, three broad peaks were observed at $2\theta \approx 15°$, 23°, and 34° in the cellulose XRD spectrum, as shown by the blue line in Figure 4-10. These peaks correspond to the reflection on the family of planes (110), (200) and (004) of cellulose, respectively (Kouadri & Satha,2018), as indicated by blue arrows in Figure 4-10. These peaks were narrower than those observed in paramylon ester and broader than those of paramylon. This phenomenon indicates that the cellulose is semi crystal, and its degree of crystallinity is lower than that of paramylon and higher than paramylon ester.

Figure 4-11 shows the XRD spectra of paramylons with different MW and paramylon esters with different DS. Four paramylon samples (P1 ~ P4) with different molecular weights (as seen in Table 4-4) showed similar spectral features despite slightly different peak intensities. Although the extraction processes of paramylon from *Euglena gracilis* cells are different from the one used in the reference, our X-ray data agrees very well with the previously reported ones. By comparing the intensities of these four samples with each other, it seems that the peak intensities are larger for lager molecular weight samples. Indeed, the peak intensity in P2 is highest, and that of P3 is lowest among paramylon samples. This result would mean that much smaller scales might determine the peak positions and the line widths of X-ray spectra in paramylon samples, *i.e*., they may be determined by much more local structural characteristics. Since the line widths are all relatively sharp ≈ 1°, all paramylon samples are supposed to have an anatomically well-ordered high degree of crystallinity.

Concerning the paramylon esters, global features that existed in the paramylon ester remain in the X-ray spectrum, as seen in Figure 4-11(e) and 11(f). For the paramylon ester sample, the peaks are much broader, and only two peaks can be identified. The broader peaks would mean that the X-ray reflections in paramylon ester show more amorphous halo scatting-like. As for PE1 sample, two broad peaks at $2\theta \approx 9°$ and 19° were observed, whereas, for PE4 sample, the two peaks at $2\theta \approx 7°$ and 20° were found as seen in Figure 4-11. Although the reason for the distinct different behavior in the lower absorption peak in PE1 and PE4 samples is not apparent, the broad peaks could be caused by the disorder effect due to the esterification of paramylon and the transformation of the crystalline

structure to more amorphous-like structure (Gan et al., 2017). According to the previous study, the effect of the degree of order of the side chains has been reported to reduce the peak width in the angle around $2\theta \approx 20°$ in cellulose (Gan et al., 2017).

Moreover, we like to point out that the lowest peak around $2\theta \approx 7°$ of PE4 shifts remarkably to a higher angle at $2\theta \approx 9°$ in PE1. We speculate that the long-range periodicity existing in paramylon, such as helical structure, may be modified by the esterification (Gan et al., 2017). Taking such a model that a long periodicity is destroyed and became shorter structure parameters as the DS level is increased.

Figures

Figure 4-1 The botryococcus braunii (BOT22) (the left bottle) and monoraphidium (A11) (the right), were cultured in nalgen bottle with 9 L culture mediums.

(a)

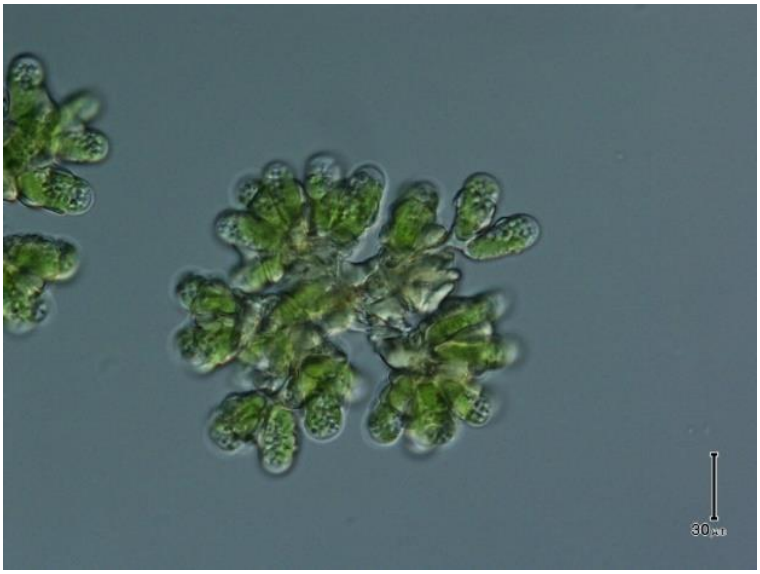

(b)

Figure 4-2 The micro-spectroscopy of BOT22 (a) cell and A11 cell (b).

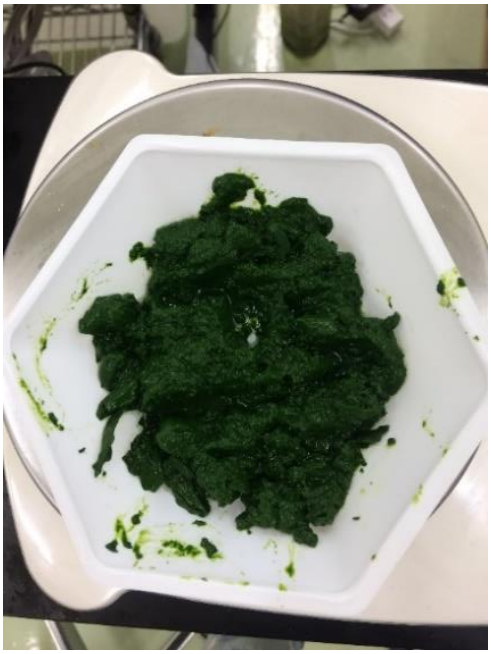

Figure 4-3 The algae biomass after dewatered.

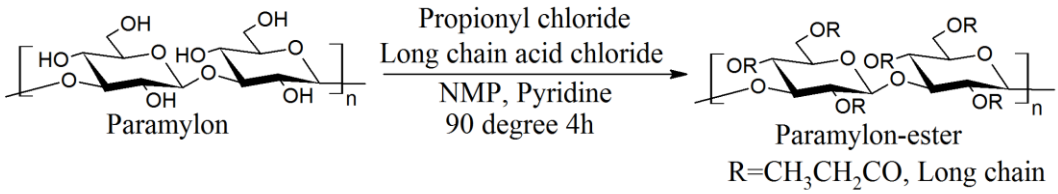

Figure 4-4　Synthesis process of paramylon ester.

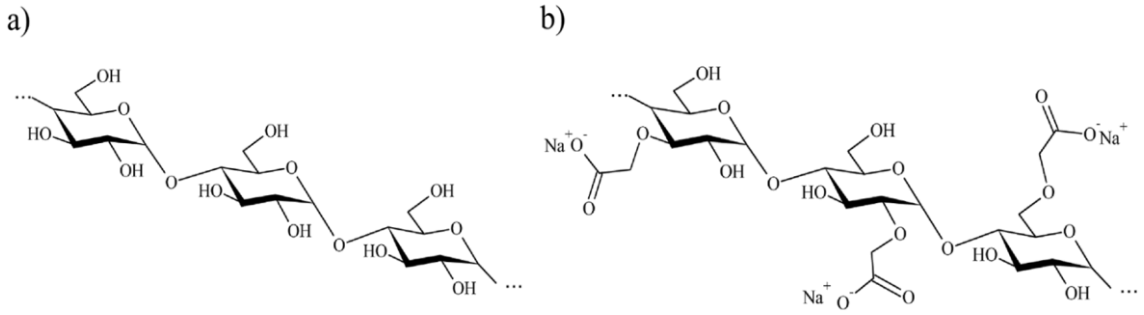

Figure 4-5 The chemical structures of natural starch and CM-starch (Kaczmarska et al., 2018).

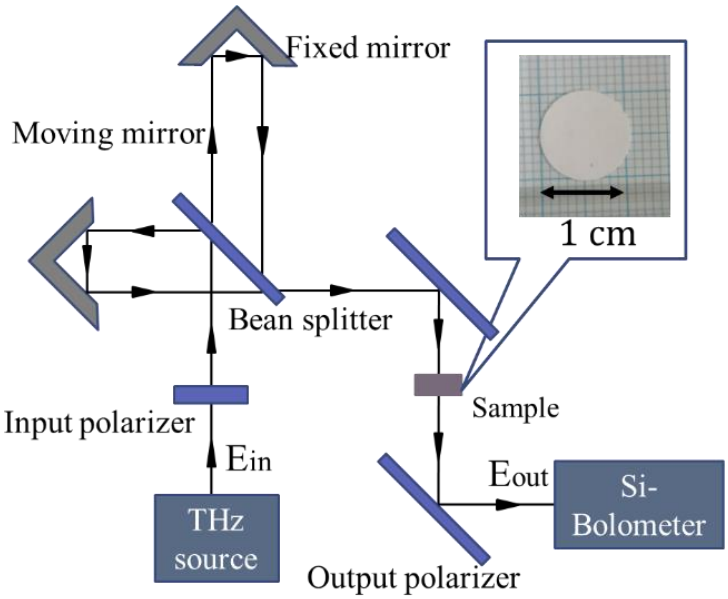

Figure 4-6 Schematic diagram of FARIS-1.

Figure 4-7 The photo of FARIS-1 and bolometer.

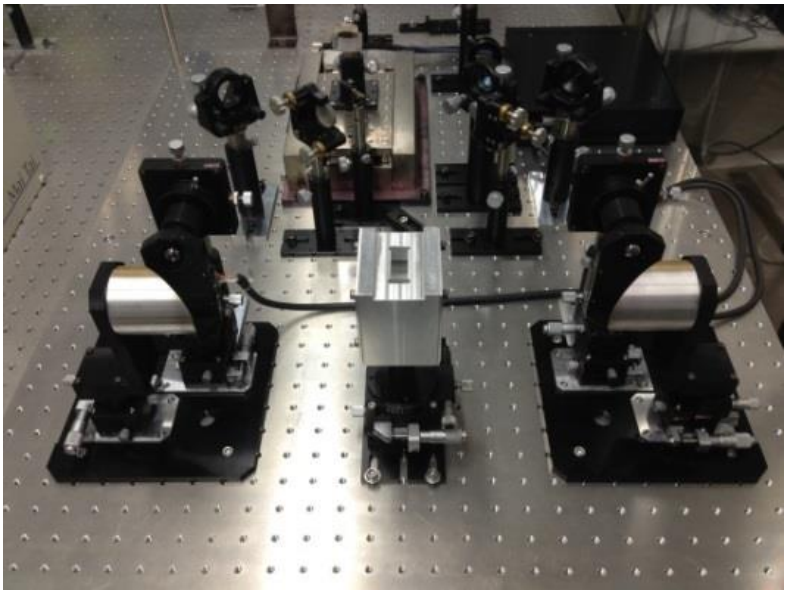

Figure 4-8 A photo of the experimental setup of RT-10000 for THz-TDS measurements.

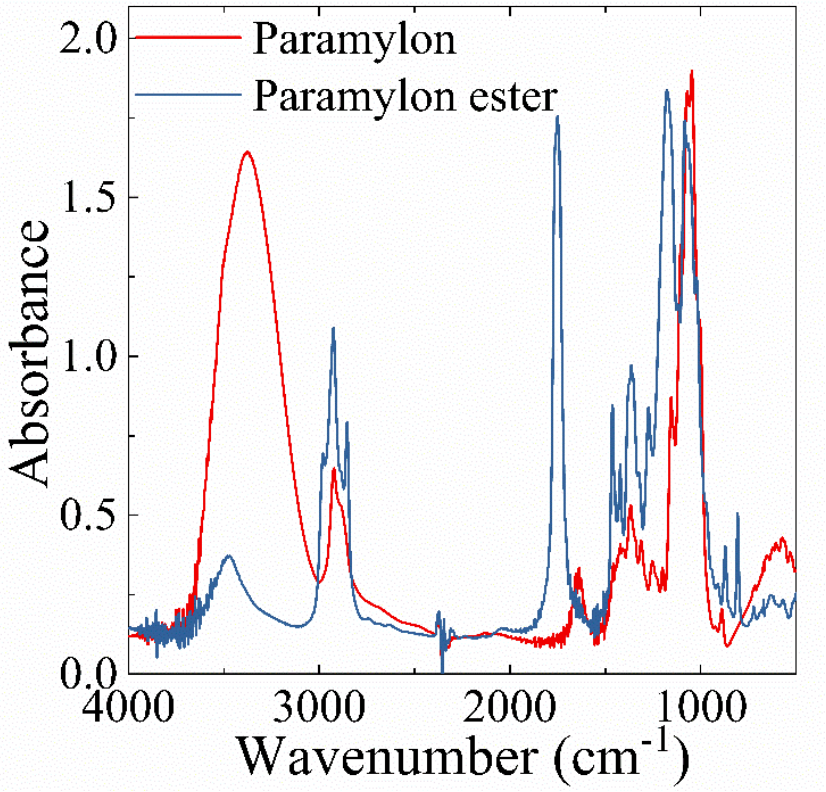

Figure 4-9 FT-IR spectra of paramylon (P1) and paramylon-ester (PE1).

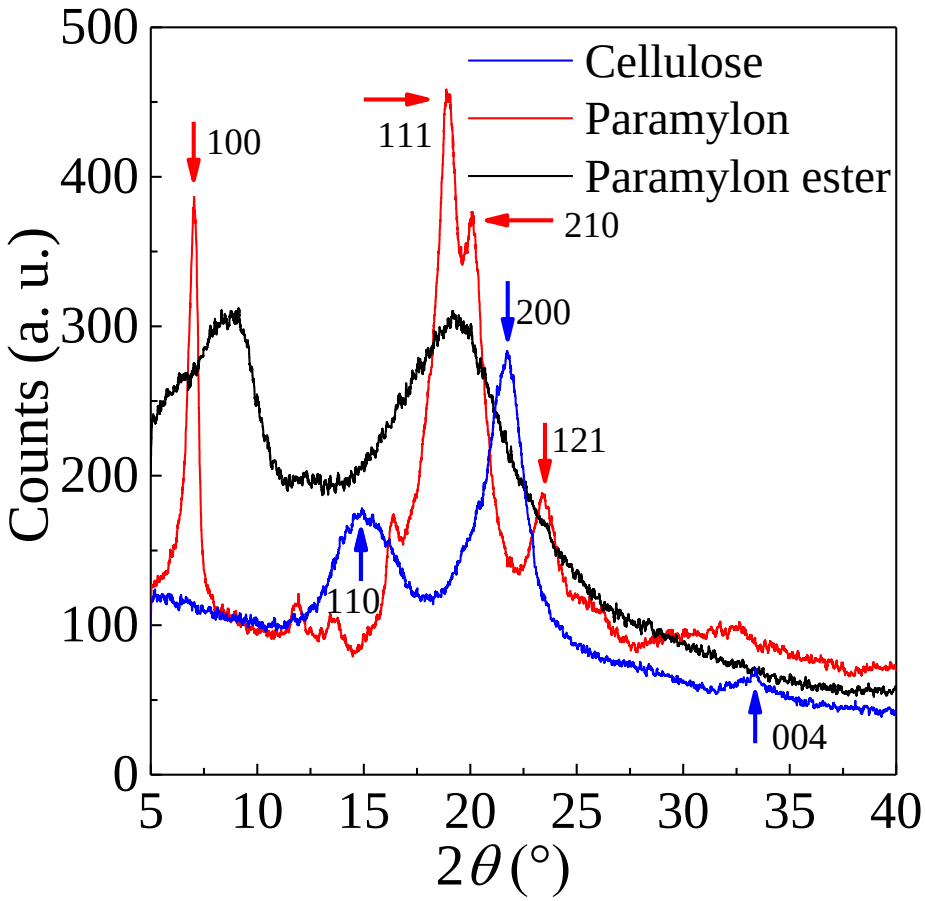

Figure 4-10 Powder X-ray diffraction spectra for cellulose, paramylon, and paramylon ester.

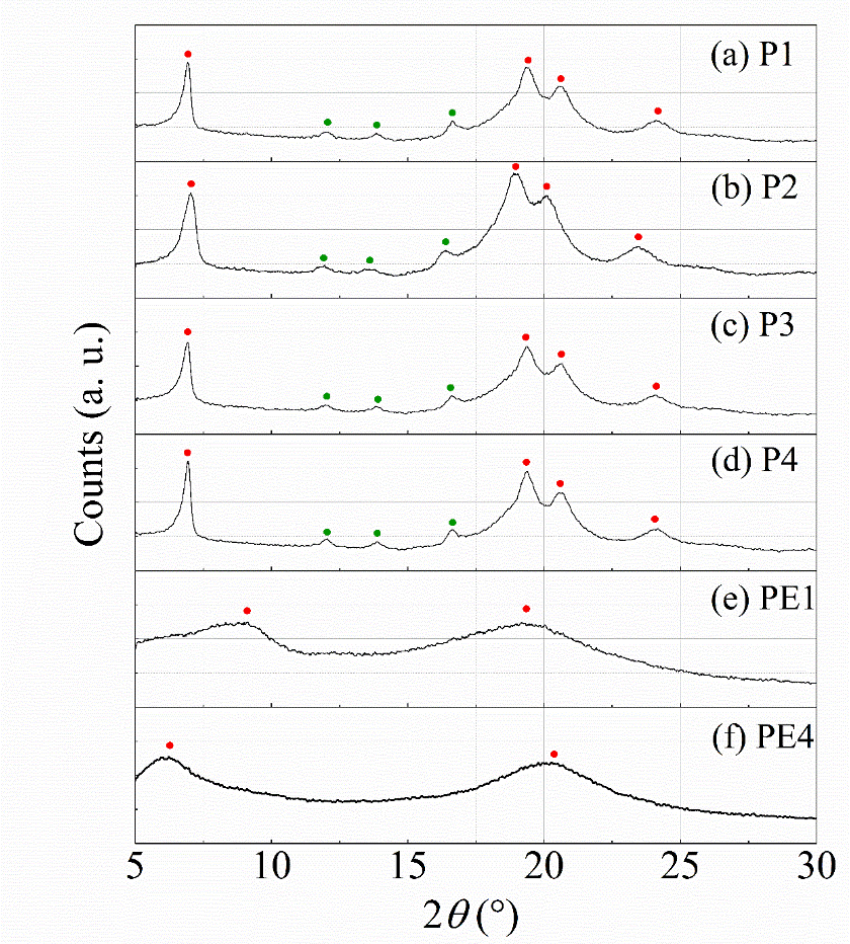

Figure 4-11 Powder X-ray diffraction patterns of paramylons and paramylon esters.

Tables

Table 4-1 The components and their content to make 10 L of Radish Sprout Medium.

Component	White	Red
$N\text{-}NO_3$, 9.5%; $N\text{-}NH_4$, 1.5%; $P2O_5$, 9%; K_2O, 35%; MgO,1%; B, 50 ppm; Zn, 125 ppm.	550	-
KNO_3	250	-
NH_4NO_3	95	-
Magnesium sulfate	70	-
EDTA-Mn, 8.3%; EDTA-Zn, 6.4%		
Magnesium nitrate	71.5	500
Calcium nitrate	-	580
Chelated iron	-	17

Table 4-2 The components and their content to make 10 L of AF-6 medium.

Component	Weight
$NaNo_3$	70 g
NH_4No_2	11 g
$MgSo_4$ $7H_2O$	15 g
$CaCl_2$ $2H_2O$	5 g
Fe Citrate	1 g
Citric Acid	1 g
KH_2PO_4	10 g
K_2HPO_4	5 g
Biotin	2 mg
Thiamine	10 mg
Vitamin B6	1 mg
Vitamin B12	1 mg
$FeCl_3$ $6H_2O$	980 mg
$MnCl_2$ $4H_2O$	180 mg
$ZnCl_2$	110 mg
CoCl2 $6H_2O$	20 mg
Na_2MoO_4 $2H_2O$	12.5 mg
Na_2EDTA 2H2O	5000 mg
MES	4 g
NaOH	16 mg

Table 4-3 The details of three different solvents.

Batch	Solvent	Radio (%)
Batch Ⅰ	Hexane: ethanol	79:21
Batch Ⅱ	Hexane: acetone	54:44
Batch Ⅲ	Methanol: chloroform	1:2

Table 4-4 The specific detailed information of paramylon samples.

Paramylon	Mn (Number-average Molecular Weight)	Mw (weight-average molecular weight)	Mw/Mn	Content of Protein (μ g/mg)
P1	71100	256000	3.6	1.49
P2	90900	264000	2.9	No data
P3	40400	96700	2.4	2.97
P4	69000	239000	3.5	0.048

Table 4-5 The detailed specific information of paramylon ester samples with different degrees of substitution (DS). The DS_{Pr} is the DS value of propionyl, and the DS_{Lo} is the DS of long-chain protons.

	Content of chloride mixture for esterification			Degree of substitution		
Paramylon ester	Propionyl chloride	Palmitoyl chloride	Stearoyl chloride	DS_{Pr}	DS_{Lo}	Total DS
PE1	7.48 g	1.35 g	1.78 g	2.28	0.31	2.59
PE2	7.50 g	0.677g	0.892g	2.26	0.16	2.32
PE3	6.00 g	0.677 g	0.892g	1.8	0.22	2.02
PE4	5.50 g	0.677 g	0.892 g	1.5	0.27	1.77

Table 4-6 The absorption peak assignment of IR spectra.

Absorption (cm^{-1})	Appearance	Group
3550-3200	strong, broad	O-H stretching
3000-2840	medium	C-H stretching
1740-1720	strong	C=O stretching
1420-1330	medium	O-H bending
1150-1085	strong	C-O stretching

Chapter 5 The analysis of glucose polymers

5.1 Introduction

Glucose is a monosaccharide with the formula of $C_6H_{10}O_6$ with a chain form or a ring form. The structure of the ring form glucose is shown in Figure 5-1(a). Glucose is widely distributed in nature and an inevitable energy supplement for the metabolism of life. Glucose has a relatively simple chemical structure, and its physical properties are well studied. Glucose forms a crystal whose cell parameters of glucose are shown as follows: space group $P2_12_12_1$ (Z = 4), a = 10.366Å, b = 14.851Å, c = 4.975Å, α, β, γ = 90.0° (Brown et al., 1979).

In particular, the D-glucose is the base unit to compose polysaccharides, such as cellulose, starch, and paramylon, which are also very important to human's daily life. These polysaccharides are linking glucosyl units by different glucosidic bonds. These polysaccharides share the same formula $(C_6H_{10}O_5)_n$, but the internal structures are remarkably different, leading to different physical and chemical properties. The chemical structures of the relevant polymers are shown in Figure 5-1.

Cellulose connects glucosyl units in multiple parallel structures by β-(1,4) glycosidic bonds. The unit number of cellulose ranges from 10^2 to 10^4 (Peccianti et al., 2017). The unit cell parameters of monoclinic cellulose are shown as follows: a = 16.34 Å, b = 15.72 Å, c = 10.38 Å (fiber axis), and β = 97.0° (Gardner & Blackwell, 1974). The thickness of the lamella cellulose chain is about 0.5 nm (Agarwal et al., 2018).

Starch is another glucose polymer consisting of glucosyl units by α-(1,4) glycosidic bonds. In nature, the storage starch is in the form of semi-crystalline granules with granule size range from sub-micron to 100 μm (Jane et al., 1994). The natural starch has two basic components: amylose (minor part) and amylopectin (major part). The amylose has a long linear chain structure consists of glucose residues connected through α-(1,4)-linkages with a few α-(1,6)-interconnected sidechains (Hizukuri et al., 1981). Amylopectin has a relatively complex double helix structure because it is consisting of shorter chains (bonding by α-(1,4)-linkages) that inter-connecting by a lot of α-(1,6)-branches (Imberty et al., 1991). The double helix structure contributes to the crystalline part of starch granule, which ranges from 17% to 50%. The starch crystallises has two type of monoclinic unit

cells, one has dimensions a = 20.83 Å, b = 11.45 Å, c = 10.58 Å (type A), and another has dimensions $a = b$ = 18.5 Å, c = 10.4 Å (type B) (Koroteeva et al, 2007).

In this chapter, we initiated for the first time to find the characteristic fingerprint spectra of paramylon and paramylon ester in the THz region, by comparing the presently available data of saccharides such as glucose and cellulose. The qualitative and quantitative analyses subsequently were concerned with paramylon with different molecular weight and paramylon ester with different degree of substitutions.

5.2 Spectral characteristics of biopolymers

5.2.1 Absorption intensity comparison

The absorption data of glucose, cellulose, paramylon, and paramylon ester in the THz frequency region between 0.3 and 10 THz is shown in Figure 5-2, which measured by the FARIS-1 system. There is strong noise in the high-frequency region because of the weak signal intensity and the strong absorption of the samples. The absorption coefficient of all sample increase with frequency. There are two possibilities that can be attributed to such a phenomenon: the scattering existing in the amorphous part and the hydrogen-bonding network to form macromolecules (Peccianti et al., 2017; Kurabayashi et al., 2017). As we mentioned above, glucose is a crystal with small molecular size; therefore, we think the increase of absorption for glucose is more related to the hydrogen bonding network.

Figure 5-2(b) and 5-2(c) show the absorption coefficient of cellulose and paramylon, which increase with the frequency, as glucose does. The absolute intensities cellulose and paramylon are much higher than that of glucose, nearly twice of glucose. It is easy to understand because cellulose is a semi-crystalline material, and its molecular weight is far more extensive than glucose. The bigger molecular weight leads to a larger number of vibrational modes and the high value of the absorption coefficient. Paramylon has a very similar spectral shape and intensity compared with cellulose in the low-frequency region below 3 THz, as shown in Figure 5-2(b) and (c). These similarities are attributed to the almost same chain structure of glycogen units of these two materials. However, in the higher-frequency region, the absolute value of paramylon is higher than that of cellulose even paramylon has a very high degree of crystallinity up to 90%, which is much higher than that of cellulose (about 50%). This result is suggestive to think that the absorption features appearing in this frequency region may originate mostly from the weak hydrogen or the similar bonds between the long strands of saccharide chains. The helix structure of

paramylon may cause stronger hydrogen bonding interaction by comparing it with the linear plate structure of cellulose. Having this interpretation in mind, the relatively lower paramylon ester absorption intensity can be understood more reasonably, as shown in Figure 5-2(d), because -OH groups of paramylon ester have been substituted by acid chloride side chains, even the crystallinity of paramylon ester is lower than cellulose.

5.2.2 Absorption peak analysis

(1) Glucose

The absorption spectrum of the glucose shows eight distinguished and relatively sharp peaks at low frequencies at 1.5, 2.1, 2.5, 2.7, 2.9, 3.4, and 3.7, as shown in Figure 5-2(a). These peaks are in good agreement with the previous studies (Lee et al., 2018; Nakajima et al., 2019; Zheng et al., 2012; Zheng et al., 2014; Wang et al., 2016; Song et al., 2018). These peaks are attributed to the intermolecular interaction modes in solid-phase glucose, and these modes are affected by the crystallinity of samples and controlled by non-covalent bonds between glucose molecules (Lee et al., 2018; Walther et al., 2003). Again, the shape absorption peaks in glucose demonstrate that glucose sample has a high degree of crystallinity and long-range order atomic arrangement. Our result in low-frequency region is in good agreement with the experimental result and theoretical calculations of Song *et al.* They assigned the rotational modes of molecules around a-axis at 1.42 THz and 3.74 THz, the rotation of molecules around a-axis at 3.48 THz, the translational motion of molecules along b-axis at 2.51 THz, and twisting of CH_2OH at 2.05, 2.64 and 2.91 THz (2018). The details are listed in Table 5-1. In the high-frequency region, six broad peaks are distributed at 4.5, 5.4, 6, 6.6, 8, and 8.9 THz. Generally, the absorption modes in THz region can be divided into two contributions. One is the intermolecular interaction modes located below 7.5 THz. Another one is the covalent skeletal deformation mode, such as C-O-C, C-C-O, and C-C-C, which are distributed in the high-frequency region (Nakajima et al., 2019).

(2) Cellulose

In Figure 5-2(b), cellulose shows five significant and broad absorption peaks at 3, 5.2, 6.53, 7, and 9 THz, and a shoulder-like peak at 2 THz. These absorption peaks are in good agreement with the previous studies of Vieira and Pasquini (Vieira & Pasquini, 2014), where only two weak and broad peaks at around 2.1 and 2.9 THz in a very narrow window of 0.7 and 3.7 THz measured by THz-TDS were presented. More recently, Kurabayashi *et al.* reported that absorption four peaks corresponding to 3.0, 5.1, 6.2 and 7.0 THz were seen in a window of 2.5 and 8 THz, and the peak intensity of those peaks strongly depend

on the crystalline structure of samples (Kurabayashi et al., 2017). The previous studies demonstrated that absorption peaks at around 2 and 3 THz are related to long-range intermolecular interactions in the crystalline part of cellulose (Vieira & Pasquini, 2014, Peccianti et al., 2017). The peaks observed in cellulose become broader by compared with that of glucose because of the superposition of the ordered vibrational modes in the crystalline part and the random orientational modes in the amorphous part (Peccianti et al., 2017). Furthermore, Vieira *et al.* assigned the absorption peak at 2.15 THz as the backbone vibration modes of a glucan-based biopolymer (Vieira & Pasquini, 2014).

(3) Paramylon

The paramylon, however, shows broader absorption spectral width than the cellulose and only broad peaks around 4, 6 and 8 THz and a shoulder-like peak around 2 THz are observed, as shown in Figure 5-2(c). This result is contrary to the universal optical phenomenon because paramylon possesses much higher crystallinity compared to cellulose, and in general, materials with higher crystallinity demonstrate more distinguished absorption peaks compared to less crystalline ones. However, the above behavior of paramylon can be easily explained by considering the number of atoms within each cell. A unit cell of paramylon contains 18 glucopyranose residues with the unit cell size of $a = b = 15$ Å and $c = 18$ Å (Chuah et al., 1983). The size of the unit cell of cellulose is given by $a = 7.78$ Å, $b = 8.20$ Å, and $c = 10.38$ Å with only 4 glucopyranose residues (Penttilä, 2013). A unit cell of paramylon comprises 378 atoms, which far exceeds those in a unit cellulose cell (84 atoms). These excess atoms result in the realization of a large number of vibration modes. Therefore, a probable reason behind the broad absorption spectrum of paramylon is the superposition of a large number of vibration modes. The differences in the peak features may also be attributed to the different chain structures between cellulose and paramylon, as we mentioned above.

(4) Paramylon ester

The absorption spectrum of paramylon ester is quite different from those of other polysaccharides. Comparing the absorption data of paramylon as shown in Figure 5-2(c) and paramylon ester as shown in Figure 5-2(d), firstly, it is evident that both absorption lines are much broader and three broad peaks around 4.0, 6.0 and 8.0 THz are found for paramylon, whereas only two broad peaks 2.7 and 5.0 THz are found for paramylon ester. Welther *et al.* demonstrated that the increase in the effective mass will redshift the vibrational potentials of the hydrogen bonds, and lead the redshift of absorption peak in the THz region (2003). Therefore, we speculate that the peaks that appeared at 2.7 and

5.0 THz in the spectrum of paramylon ester are the results of the redshift of the peaks at 4.0 and 6.0 THz in the spectrum of paramylon. Since in paramylon ester, the -OH group in a glucose unit is replaced by propionyl or long-chain protons (stearoyl and palmitoyl groups (60:40)), which has much bigger effective mass than -OH group.

Also, the substitution of -OH groups leads to the smaller amount or weaker force of the hydrogen bonding network in paramylon ester. Consequently, this leads to the lower frequency and intensity absorption peak in the THz region. It is believed that the decreasing number of -OH group in paramylon esters induces the reduction of the dipole moment, resulting in the reduction of the absorption intensity near 5 THz. This speculation is based on the recent systematic study of -OH bond in nicotinamide exhibiting a characteristic stretching vibrational mode around 4.0 THz (Takahashi et al., 2017). In spite of the exciting similarity in both cases, further study is certainly needed to verify such speculation more clearly.

It is noted that the spectral shape becomes broader from paramylon to paramylon ester and from cellulose to paramylon as well. This may be reflected by the broader feature of the vibrational mode frequencies in each material due perhaps to the more disordered nature of the structure originated from the synthesizing processes. Since the number of absorption peaks, as well as these peak positions, might be related to each other, but it seems not to have enough clues to assign them clearly at this moment. By making further study in more detail, we are confident that it is possible to establish the so-called fingerprint spectra of long chain-like macromolecules such as paramylon, paramylon-esters, and the related many similar compounds associated with the polysaccharides.

5.2.3 Peak assignments for polysaccharides

As depicted in Figure 5-3, a sharp peak for cellulose and broad peaks for paramylon and paramylon ester exist at approximately 2 THz. The sharp peak of cellulose derives from its crystalline part (Vieira & Pasquini, 2014; Peccianti et al., 2017). If the same origin exists for all peaks, phonon analysis based on DFT calculations for crystalline cellulose is helpful to understand the origin of the broad peak of 2 THz in the amorphous part. It is proposed to be considered in future research. As regards the origin of vibration modes at 2 THz, Fischer *et al.* (2005) commented that the absorption peak at approximately 2 THz relates to backbone vibration modes of cellulose, and the frequency of this peak is decreasing with the increase of the sidechain mass. However, experimental results obtained in this study reveal that although the sidechain mass of paramylon ester is much

higher compared to those of paramylon and cellulose, peak frequencies of all three polymers undergo little change. Recently, Milkus *et al.* (2018) performed MD simulations using the Kremer–Grest model to calculate the VDOS for polymeric glass. They attributed the existence of the low-frequency VDOS band to vibrational modes resulting from the Lennard–Jones (LJ) potential, which describes noncovalent interactions between molecules. We speculate that LJ interactions can be attributed to noncovalent interactions caused by van der Waals forces that act between all atoms, thereby resulting in the realization of broad absorption peaks for paramylon and its corresponding ester at approximately 2 THz.

At 3 THz, cellulose and paramylon show distinguished peaks and large absorption coefficient values. The sharp peak at 3 THz for cellulose is derived from its crystalline part, which is the same as the peak observed at 2 THz. In contrast, paramylon ester does not demonstrate any peak near 3 THz and has a very small absorption-coefficient value. These differences are caused by the change in magnitudes of dipole moments induced by the different structures of these polymers. In particular, it is considered that the reduced number of -OH groups in paramylon ester causes the observed reduction in the absorption coefficient at 3 THz. Regarding other saccharides, lactose (Saito et al., 2006) and maltose (Bernier et al., 2017) demonstrate sharp absorption peaks at approximately 3 THz, thereby suggesting that 3-THz modes are a general feature of glucose-based polymers. In addition, Shibata et al. (2015) have reported that the strong absorption peak of amorphous indomethacin at 3 THz can be attributed to a mode caused by hydrogen-bonded centrosymmetric cyclic dimers between indomethacin molecules. Furthermore, Hoshina et al. considered the mode observed at 2.92 THz for poly(3-hydroxyalkanoates) as the hydrogen-bonding interaction between helical chains (Hoshina et al., 2010; Hoshina et al., 2013). It can, therefore, be concluded that the observed absorption peak near 3 THz derives from the vibrational motion of -OH groups.

As already mentioned, the value of the absorption coefficient for paramylon ester is significantly reduced at 3 THz, whereas corresponding values for cellulose and paramylon remain nearly steady. This is because, for cellulose and paramylon, -OH-group vibrations contribute towards the realization of not only a specific mode but also collective vibrational modes in the THz region, thereby resulting in large absorption-coefficient values around 3 THz.

5.3 Qualitative analysis of paramylons with different molecular weights (MW)

Figure 5-4 shows the absorption spectra of paramylons with four different molecular weights, which were described in Table 4-4. Four paramylon samples show a very similar absorption behavior. They all have a broad absorption peak at around 4 and 6THz. This fact that the absorption is, in fact, independent of the size of the molecules must be originated from a typical characteristic feature of paramylon such as vibration modes originated from hydrogen bonding modes of -OH group.

At higher frequencies above 8 THz, the noise becomes stronger, and we could not find out any significant absorption peak in this region. It is worth pointing out that the impurity content may affect the higher background absorption level.

5.4 Quantitative analysis of paramylon esters with different degree of substitutions (DS)

In contract with the spectra features of paramylon below 8 THz as found above, paramylon ester samples show two broad absorption peaks around 2.7 and 4.8 THz, as shown in Figure 5-5. Although they are rather broad but can be regarded as the proper special features of paramylon ester. With increasing the quantity of DS, the total THz absorption decreases dramatically. Such a difference is much significant in the higher frequency region above 4 THz. This fact can be supported by our speculation that the decrease of the number of -OH groups may reduce the absorption intensity, as we already mentioned above. When the DS equals 2.59 for PE4, the peak around 5 THz is hardly to see (shaded by purple color), which demonstrates that the peak observed at 5 THz for paramylon ester is attributed to the vibrations of hydrogen bonding. In addition, the broad absorption peak shaded by a green color around 2.7 THz slightly has a tendency to shift to lower frequencies with increasing DS-values of paramylon esters. This provides evidence that the peak at 2.7 THz for paramylon ester may be the result of the redshift of the peak at 4 THz for paramylon. This phenomenon is consistent with Fischer's result that the absorption peak of glucans may shift to lower frequency with the increasing of sidechain masses (Fischer et al., 2005).

The relationship between the DS-value of paramylon-ester and the intensity of absorption peak around 2.7 THz and 4.85 THz shows in Figure 5-6. The DS-values have a clear

linear relationship with the peak intensities around 2.7 THz and at 4.85 THz. The linear fitting is showing by the black line for 2.7 THz absorption and red line for 4.85 THz absorption. Comparing the fitted line slopes for the two peak intensities, the slope value of 4.85-THz absorption peak is more significant than that of 2.7 THz line so that they intercept each other, indicating higher scattering and absorption effect in the higher frequency region. The average correlation coefficients (R^2) are calculated to be 0.985 and 0.999 for 2.7 THz and 4.85 THz, respectively. From this linear behavior of two finger-print absorption intensities, it is interesting to point out that the DS-value of paramylon-ester can be estimated. A similar characterization using the finger-print absorption may be possible for even other glucose-based polymers.

5.5 Conclusion

I have studied THz absorption spectra of paramylon extracted from algae *Euglena gracilis* and chemically modified by the esterification to paramylon-esters at ABES center and NEC Corp. Prior to the THz measurement, the crystallinities the samples were checked by powder X-ray diffraction method in polycrystal paramylon powders and discussed the level of disorder of these materials. We have also measured the FTIR spectra of paramylon and paramylon ester and confirmed that the chemical esterification reaction is well completed. Then, we performed THz spectral measurement down to below 0.5 THz and observed for the first time the characteristic fingerprint-like absorption peaks existing both in paramylon and paramylon esters. The different absorption features of different polysaccharides indicate that absorption features of each sample in the THz region are sensitive to the structure and spatial arrangement of molecules, which providing a spectral fingerprint to identify different saccharides. These characteristic features are discussed by comparing the data with the spectra of glucose and cellulose having similar but much more straightforward structures. Moreover, these materials are so popular that many publications have been available.

From the main results, it can be said that the paramylon has broad three absorption peaks at 4.0, 6.0, and 8.0 THz, while the paramylon ester shows similar broad spectral features around 2.7 and 4.85 THz. Four paramylons with different molecular weights were compared with each other, and a possible impurity effect showing up in a frequency region from 5 to 9 THz in paramylon was discussed. Last, we analyze the spectra of paramylon esters with different DS. The linear relationship between the peak intensities and DS was found with reasonable accuracy. Although we are not able to identify the absorption and was unsuccessful in assigning the absorption modes, we believe that the

present work deserves a new step for a better understanding of paramylon and paramylon-ester. Further intensive study is needed to explore useful applications of these compounds.

Figures

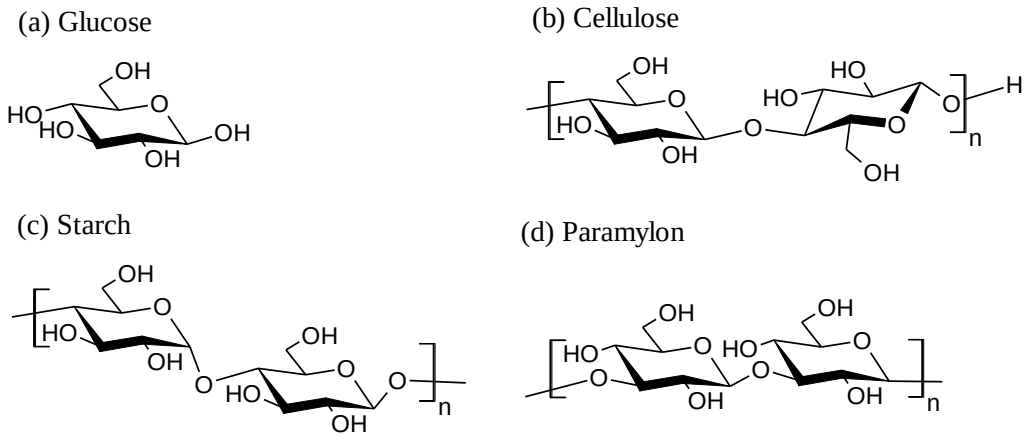

Figure 5-1 The chemical structures of glucose (a) and polysaccharides (cellulose (b), starch (c), and paramylon (d)).

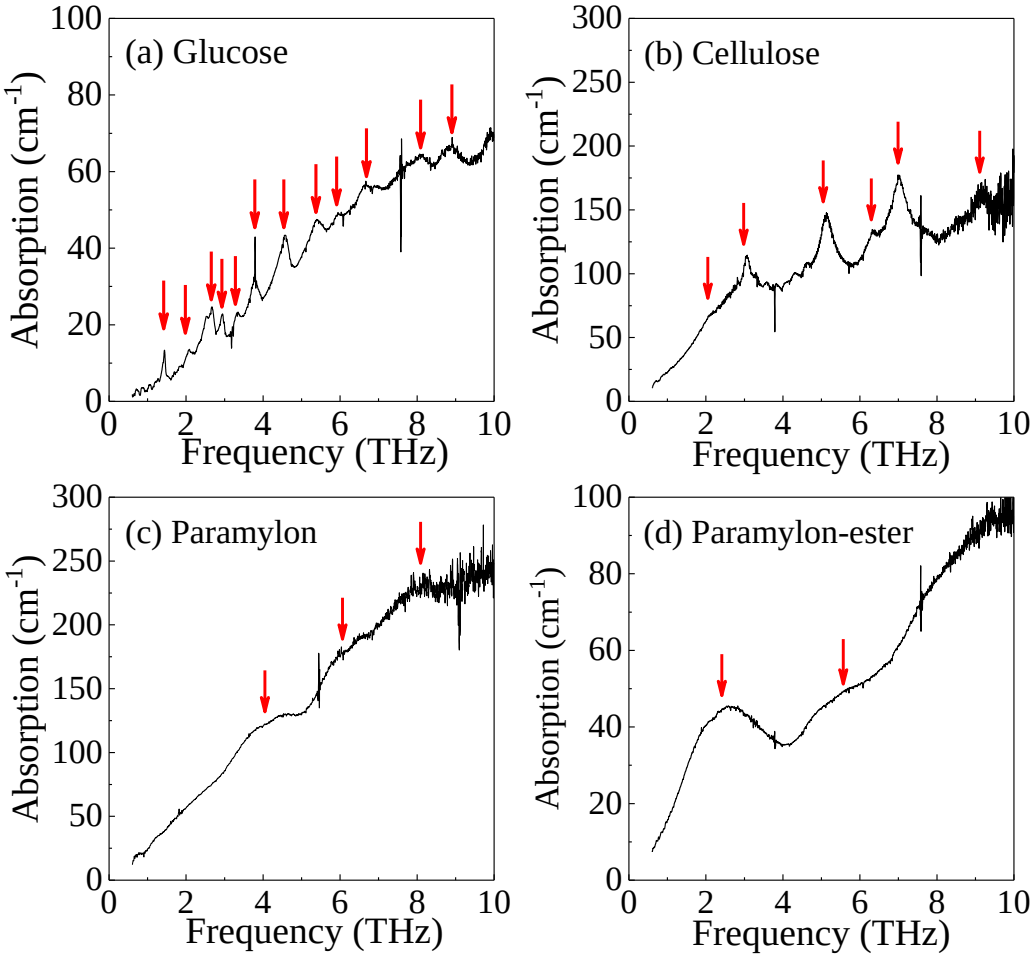

Figure 5-2 Absorption spectra of (a) glucose, (b) cellulose, (c) paramylon, and (d) paramylon-ester.

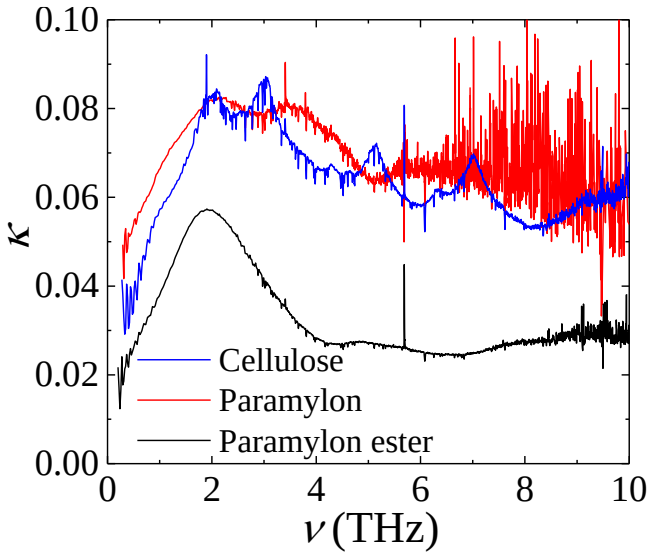

Figure 5-3 Extinction spectra of cellulose, paramylon, and paramylon-ester.

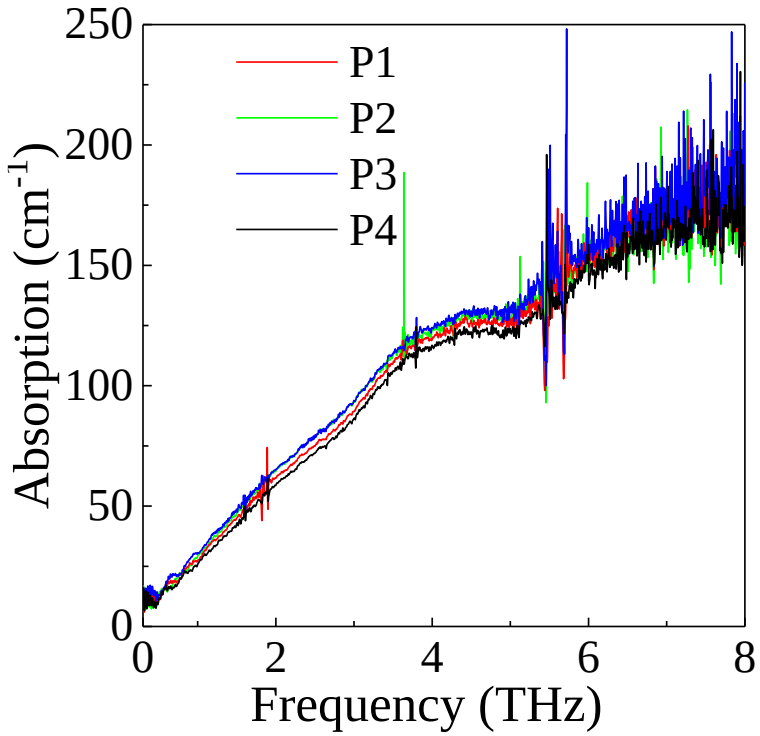

Figure 5-4 Absorption spectra of paramylons with different molecular weights.

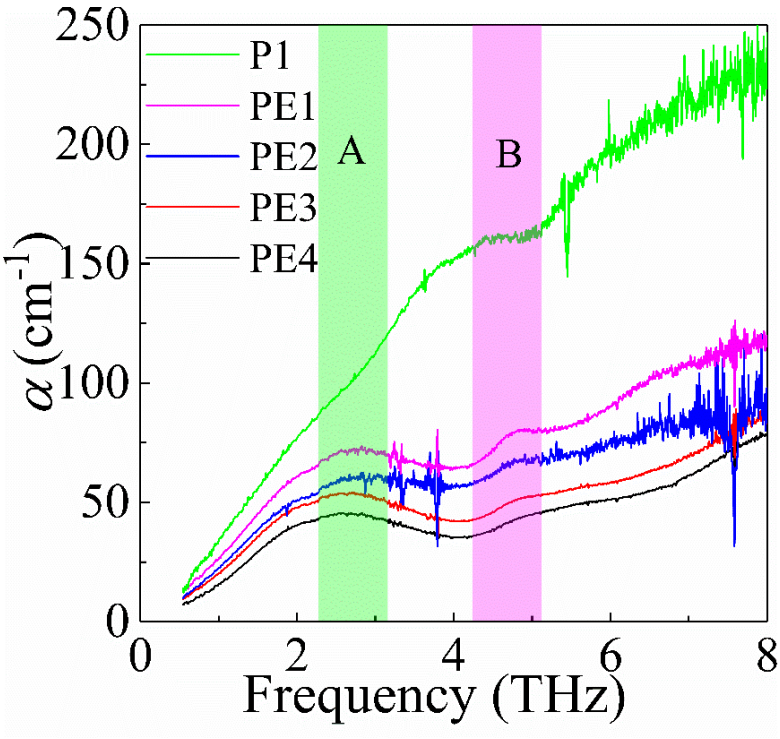

Figure 5-5 Absorption spectra of paramylon esters with different degree of substitutions.

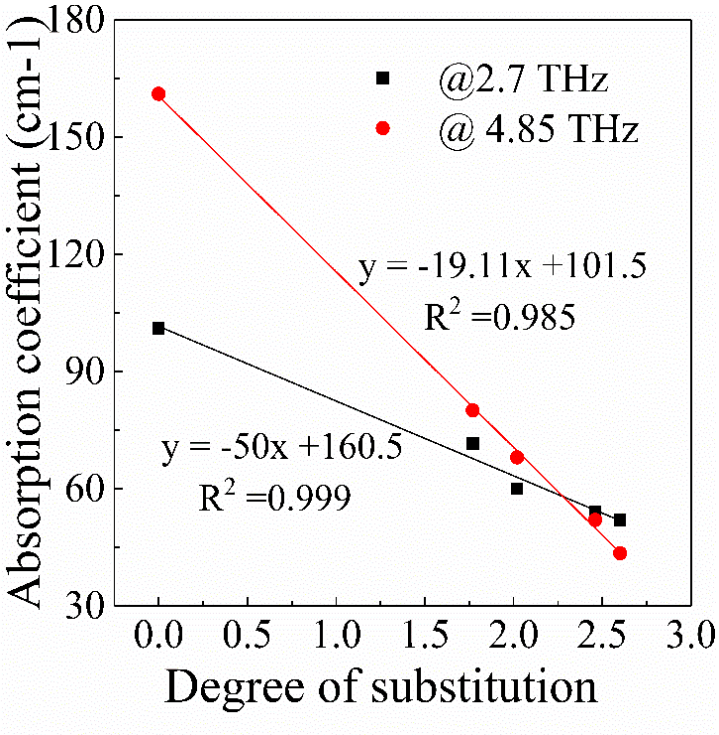

Figure 5-6 The relationship between the DS and the intensities at 2.7 THz and 4.85 THz.

Table

Table 5-1 The assignment of the THz absorption peaks of glucose.

Experiment (THz)	Simulation (THz) (Song et al., 2018)	Mode description (Song et al., 2018)
--	1.26	Translational motion of molecular along a-axis
1.5	1.5	Rotation of molecules along a-axis
2.1	2.03	Twisting of –CH2OH
2.5	2.38	Translational motion of molecular along b-axis
2.7	2.68	Twisting of –CH2OH
2.9	2.7	Twisting of –CH2OH
3.4	3.69	Rotation of molecules along b-axis
3.7	3.88	Rotation of molecules along a-axis

Chapter 6 Boson peak analysis

6.1 Introduction

As we mentioned in Chapter 2, glassy systems show very different optical properties compared with those of ordered crystals as counterparts because of the disordered structure of glasses. One of the most significant differences is the vibrational modes in low-frequencies vibration modes. In crystals, the acoustic phonon shows a linear dispersion relation $g(\nu) \propto \nu^2$ as the Debye model described. In the glassy system, a university excitation, which is called as the boson peak (BP), is observed in the $g(\nu)/\nu^2$ spectrum in the THz region.

In this chapter, the temperature-dependence THz spectroscopy was performed on four glucose polymers and esters—cellulose, paramylon, paramylon ester, and sodium carboxymethyl starch (CM-starch)—to investigate the determinants of the boson peaks and fractal dynamics. The complex dielectric constants of these glucose polymers were analyzed and compared with each other and with glucose and starch that reported by previous studies. The properties of BPs of these polymers were discussed; their fractons were calculated based on the $\alpha(\nu)/\nu^2$ spectra.

6.2 Temperature dependence of complex dielectric constant and boson peak

6.2.1 Analysis of cellulose

The real $\varepsilon'(\nu)$ and imaginary parts $\varepsilon''(\nu)$ of the complex dielectric constant of cellulose are shown in Figures 6-1(a) and 6-1(b). The crystallinity of cellulose equals 50% approximately (Ishikawa, 1997). Therefore, those spectra consist of the superposition of the response from the crystalline part and the amorphous part.

There is a broad resonant peak around 1 THz in the spectra of $\varepsilon''(\nu)$, as shown in Figure 6-1(b), which is an absorption owing to an optical phonon in the crystalline part of cellulose, rather than the amorphous part. As the temperature decreases, the value of $\varepsilon''(\nu)$ decreases, and the peak becomes more apparent than at higher temperatures. The behavior is attributed to the freezing of fast relaxation at low temperatures, which exists in the THz side. On the other hand, when the temperature increases, the thermal energy increases,

the vibrational levels will be populated, leading to broad absorption profile (Walther et al., 2003).

The temperature-dependences of the $\varepsilon''(\nu)$ spectra of cellulose are similar to those of starch, as shown in Figure 6-2(b) (Terao et al., 2018). By comparing with $\varepsilon''(\nu)$ spectra of starch, the resonant peak in $\varepsilon''(\nu)$ spectra of cellulose are significantly more apparent. Instead of a peak observed in the $\varepsilon''(\nu)$ spectra of cellulose, there is an inflection point appeared around 0.7 THz in the $\varepsilon''(\nu)$ of starch. This is because there is no optical phonon existing around 1 THz in the starch system. Both the peak and inflection points observed in the spectrum indicate the existence of the boson peak. The relationship between the phonon mode and the boson peak will discuss in the late section.

The value of real part $\varepsilon'(\nu)$ of cellulose decreases with the decrease in temperature and shows a peak at 0.75 THz, which is the typical value of BP frequency, as shown in Figure 6-1(a). Same as the spectrum of $\varepsilon''(\nu)$, the peak undergoes a dramatic change in shape and width as the temperature decreases. The behavior of the real parts $\varepsilon'(\nu)$ can also be easily understood by the Kramers–Kronig relations between the real and imaginary parts of the complex dielectric constant (Terao et al., 2018).

Figure 6-1(c) shows the $\alpha(\nu)/\nu^2$ spectra of cellulose. A blurred peak is observed near 1 THz at room temperature, which is hardly visible owing to the effect of the existence of the fast relaxation tail. The peak becomes much clearer at low temperatures and is located at 0.92 THz at the lowest temperature. The peak is composed of both the phonon peak of the crystalline part and the boson peak of the amorphous part of the semi-crystalline cellulose, and we concluded that this peak frequency is the boson peak frequency of cellulose. This BP frequency is similar to that of starch (0.99 THz). Because cellulose and starch have very similar chemical structures, and they are both semi-crystalline. The crystallinity of cellulose is about 50% (Ishikawa, 1997), which is higher than that of starch (33.9%) (Kaczmarska et al., 2018). The higher crystallinity of cellulose causes the lower intensity of cellulose than starch because the BP peak indicts the disappearance of translational symmetry of amorphous molecules and the spectral shape of the VDOS around BP frequency (Mori et al., 2019).

6.2.2 Analysis of CM-starch

Figure 6-3 shows the temperature dependence of (a) the real part $\varepsilon'(\nu)$ and (b) the

imaginary part $\varepsilon''(\nu)$ of complex dielectric constant, and the $\alpha(\nu)/\nu^2$ spectrum (c) of the CM-starch during the heating process measured by THz-TDS, which is measured by Terao (Terao, Master's thesis, 2018).

As the temperature increases, the values of both the real and imaginary parts of the ε increase, as shown in Figures 6-3(a) and 6-3(b). This behavior is similar to cellulose and starch, as we discussed above. A broad peak is observed at 0.75 THz in the $\varepsilon'(\nu)$ spectrum at the lowest temperature and the peak shift to lower frequency as the temperature increase, as shown in Figure 6-3(a). This temperature-dependence shift is different from that of starch. In the $\varepsilon'(\nu)$ spectrum of starch, a resonance peak is 0.7 THz at the lowest temperature, and this frequency is similar by compared with that measured at higher temperatures, as shown in Figure 6-2(a). The temperature-dependent frequency shift in the $\varepsilon'(\nu)$ spectrum of CM-starch is caused by the tail of the fast relaxation mode seen in the low-frequency region has shifted to the high-frequency side as the temperature rises as we mentioned above. In the fragile system, the fast relaxation mode is strong and partially hide the BP structure at high temperature. The imaginary part $\varepsilon''(\nu)$ increase with the increase of frequency, as shown in Figure 6-3(b), which is good agreement the relation of real part $\varepsilon'(\nu)$. An inflection point is appeared at 1.3 THz at the lowest temperature, indicating the presence of a boson peak.

Figure 6-3(c) depicts the $\alpha(\nu)/\nu^2$ spectrum of the CM-starch. The boson peak was clearly observed at 1.16 THz at the lowest temperature of 16 K. As the temperature increased, the shape of the boson peak became broader, and the peak frequency shifted to the lower-frequency side. The BP frequency of CM-starch at the lowest temperatures slightly higher than that of starch. However, because only a smaller amount of -COONa groups were introduced into CM-starch, and the -mass of –COONa is small. The structure difference between starch and CM-starch should is smaller, and hence the BP frequency should be similar. Also, the BP shape of CM-starch is broader than that of starch, which can be regarded as a more shoulder-like structure by comparing with starch. The shoulder and the plateau-like spectral shape at low temperatures resemble the Raman spectrum of polymethylmethacrylate (PMMA) (Saikan et al., 1990). From the analogy of the Raman coupling coefficient of PMMA (Surovtsev & Sokolov, 2002), the reason why the BP of PMMA is not a peak but a shoulder structure can be naturally understood by assuming that the $C_{IR}(\nu)$ of PMMA is linear frequency-dependent. In addition, the linear frequency-dependent $C_{IR}(\nu)$ leads the lower BP frequency measured by THz spectroscopy than the BP frequency measured by Raman scattering and neutron inelastic scattering (NIS).

Therefore, the higher BP frequency and broader BP shape may cause by the linear frequency-dependent of the $C_{IR}(v)$ (Surovtsev & Sokolov, 2002). To conclude that the real BP frequency of CM-starch is lower than measured BP frequency by THz spectroscopy and similar to the BP frequency of starch, which is around 1 THz.

6.2.3 Analysis of paramylon and paramylon ester

Figures 6-4(a) and 6-4(c) show the $\varepsilon'(v)$ and $\varepsilon''(v)$ of the complex dielectric constant for the paramylon. Both values of the $\varepsilon'(v)$ and $\varepsilon''(v)$ decrease toward low temperature which is same as those of the substances we discussed above. However, the amount of reduction of $\varepsilon''(v)$ spectrum seems frequency-independence, and it resembles a nearly constant loss (NCL) behavior (Ngai, 2011). The broad peak at 2 THz shows almost no temperature dependence indicating that paramylon is amorphous aperiodic. According to the results of XRD that we discussed in section 4.4, paramylon has a high degree of crystallinity (approximately 90%). However, the observed NCL behavior of paramylon is representative of amorphous materials, and this contradicts the above consideration of paramylon being highly crystalline. Therefore, the occurrence of the observed broad peak in the THz band can be attributed to the presence of a large unit cell, as mentioned in section 5.3.

On the other hand, the features of the complex dielectric constant of the paramylon ester are differing from those of the other glucose polymers mentioned above, as shown in Figures 6-4(b) and 6-4(d). The value of $\varepsilon'(v)$ of paramylon ester increases as the temperature decreases, whereas that of other substances decreases towards lower temperatures. For example, for all substances, the values of $\varepsilon'(v)$ around 1 THz decrease toward low temperature, however, the value of $\varepsilon'(v)$ around 1 THz increases for only paramylon ester. The origin of the difference mainly can be attributed to the blueshift of the VDOS peak of paramylon ester, which can be observed in the $\varepsilon''(v)$ spectrum of paramylon ester, as shown in Figure 6-4(d). A clear broad peak is observed around 2 THz in the $\varepsilon''(v)$ spectrum, and the peak is shifted to higher frequency toward low temperature. The peak frequency of the lowest temperature is 2.35 THz, and this value is 20% higher than that of the absorption-peak measured at room temperature (1.85 THz).

We point out that generally, we should be careful in interpreting the temperature change of the terahertz spectrum of such a glass. If we do not examine temperature changes in both the real and imaginary parts, we may misunderstand the origin of the behavior. In

particular, care should be taken when analyzing data in narrow frequency bands.
Figures 6-4(e) and 6-4(f) shows the $\alpha(\nu)/\nu^2$ spectra of paramylon and paramylon ester. At room temperature, the BP of paramylon ester has not been observed owing to the effect of the excess wing of fast relaxation. However, at low temperatures, a clear shoulder has been observed around 0.75 THz, which can be regarded as the BP of paramylon ester. The reason why the BP of paramylon ester is not a peak but a shoulder structure can be naturally understood by assuming that the $C_{IR}(\nu)$ of paramylon ester is linear frequency-dependent, this is similar to CM-starch. According to the VDOS peak measured by NIS, the real BP frequency is 0.5 THz (unpublished data). Therefore, the BP frequency of paramylon ester is 0.5 THz, slightly lower than the frequency detected by THz spectroscopy.

On the other hand, even at the lowest temperature, BP of paramylon is not clearly observed, and the following two reasons can be considered. One possibility is that the BP of paramylon has been hidden by the NCL-like structure that remained even at low temperatures. Another possibility is that paramylon, which has a high degree of crystallinity, has polycrystalline-like properties, and the BP disappeared virtually. There is no resonant-like structure in the spectrum of $\varepsilon'(\nu)$ near 1 THz for paramylon, which universally appears associated with BP (Kabeya et al., 2016; Terao et al., 2018), even at low temperatures, as shown in Figure 6-2(b). From these observations, the BP of paramylon seems not to exist. Detailed studies should be done with complementary investigations such as low-frequency Raman scattering and low-temperature specific heat measurement.

6.3 Comparison of boson peaks

Figure 6-5 compares the BP spectra for glassy glucose, cellulose, starch, CM-starch, and paramylon ester at the lowest temperature. The BP spectrum of glassy glucose was measured and discussed by previous research (Kabeya et al., 2016). The BP frequencies and intensities measured at the lowest temperature of glassy glucose and mentioned glucose polymers are listed in Table 6-1.

The maximum intensity at BP frequency of the $\alpha(\nu)/\nu^2$ spectrum for glassy glucose is the 29.0 $cm^{-1}THz^{-2}$ at BP. The glucose was selected as the reference for the analysis of glucose polymers because the crystallinity of glassy glucose nearly equals to zero. The BP intensities of cellulose, starch, and CM-starch were 10.9, 20.4, and 23.0 $cm^{-1}THz^{-2}$,

respectively. All glucose polymers have lower BP intensities than glucose. This is because glucose is a monomer and has more -OH groups than glucose polymers. The number of hydroxyl groups (-OH) contained per glucosyl unit is 3 for glucose polymers and 5 for glucose (Terao et al., 2018).

Then, the crystallinities of those polymers were compared. The crystallinities of cellulose, starch, and CM-starch were 50%, 33.9%, and 0%, respectively. As the crystallinity increases, the maximum BP intensity decreases, as listed in Table 6-1. This result demonstrated that the higher crystallinity might cause higher BP intensity of glucose polymers. The BP intensity of paramylon ester equals 11.4 $cm^{-1}THz^{-2}$, which equals nearly half the corresponding value for CM-starch, although their crystallinities are nearly the same. The DS of paramylon ester is 2.6, nearly all -OH groups existing in the paramylon ester system are substituted by chloride acids. While the DS of CM-starch is smaller than 0.7, only a small amount of the -OH groups are replaced by -COONa groups. Therefore, the low BP intensity of paramylon ester may cause by the disappearance of hydrogen bonds. This phenomenon is caused by the same factor as the lower intensity of monomer glucose than polymers. In conclusion, the BP intensity may be affected by the content of -OH groups and the crystallinity of an amorphous sample.

The BP frequencies of glucose polymers are also compared by setting glassy glucose as a reference. The BP frequency for cellulose, starch, and CM-starch nearly equals that for monomeric glucose glass, which is about 1 THz, as shown in Table 6-1. Recently, the VDOS value for polymer glass has been investigated by performing MD simulations (Milkus et al., 2018; Giuntoli & Leporini, 2018; Tomoshige et al., 2019), and results obtained demonstrate that the BP frequency does not change much for either in a monomer or polymer. Therefore, results obtained in this study for cellulose, starch, and glucose are consistent with those obtained via MD simulations.

The BP of paramylon ester was observed at 0.75 THz as a shoulder, and the real BP frequency was identified to be 0.5 THz by NIS, which is much lower than the corresponding values of other glucose polymers and glucose. The probable reasons behind the significant reduction in BP frequency for paramylon ester compared to those for other measured glucose polymers are discussed here. There exist two probable reasons for this. One cause is the different masses of the monomer molecules by comparing it to other polymers. The mass of the paramylon ester monomer is much larger than that of other substances. To test this hypothesis, the BP frequency of another polymer was

considered. The BP frequency for PMMA is low at 0.48 THz (Hashimoto et al., 2016), although its mass equals 92 g/mol, which is less than one-third the mass of a paramylon-ester unit. Thus, the above hypothesis is likely false.

The second possible factor could be the hydrogen bonding, *i.e.,* the BP frequency for paramylon ester may decrease dramatically owing to the disappearance of –OH groups that form hydrogen bonds in other glucose polymers. Here, glucose and glucose polymers are divided into two categories: hydrogen-bonded glass and non-hydrogen bonded glass. In the hydrogen-bonded glasses, including glucose, cellulose, starch and CM-starch, the primary intermolecular interaction is the hydrogen bonding interaction; therefore, the dominant factor affecting the BP frequency is the hydrogen bonding network. On the other hand, there are few or no hydrogen bonds in the non-hydrogen bonded glass, *i. e.* paramylon ester. The week van de Weels force may be the dominant force acting between molecules. As a result, the week van de Weels force becomes the primary determinant for BP frequency. Therefore, the determinants for BP frequency may be hydrogen bonding network and week van de Weels force. The details of the categories are listed in Table 6-2.

6.4 Fracton analysis

To evaluate the interaction between the light and VDOS of the BP and fracton regions, the fractions of starch and CM-starch were determined by the log-log plot of the absorption coefficient, as shown in Figure 6-6. The absorption coefficients show a linear relationship with frequency in the log-log plot. The spectrum of starch is a linear slope from 0.8 THz to 2.2 THz, which is regarded as the fracton region. The value of the slope of this line region is μ = 1.4. On the other hand, in the spectrum of CM-starch, a linear region appeared from about 0.8 THz to 2.2 THz, and the value of this slope was μ = 1.5, which was slightly larger than that of starch. The higher power-law dependence is considered to reflect that CM-starch was an amorphous starch having a crystallinity of almost zero, and thus exhibited stronger absorption than starch. The value of fracton dimensions d_f for CM-starch and starch is the same as 1.33, which taken from the literature [Alexander]. (The details are listed in Table 6-2).

$$\mu = 2\frac{d_f}{D_f} + d_f - 1. \tag{6-1}$$

6.5 Conclusions

The VDOS and the determinants of boson peak (BP) of several glucose polymers, including cellulose, paramylon, paramylon ester, and CM-starch, were investigated by the temperature-dependent THz spectroscopy. The complex dielectric constants (ε) observed below 2-THz frequency were analyzed and compared. For cellulose, paramylon, and CM-starch, the values of both the real part $\varepsilon'(\nu)$ and imaginary part $\varepsilon''(\nu)$ of the ε decrease with the decrease of the temperature because of the redshift of excess wing owing to the freezing of fast relaxation modes. The complex dielectric constant of paramylon ester is very different from others. The value of $\varepsilon'(\nu)$ of paramylon ester increases as the temperature decreases. The origin of the behavior mainly can be attributed to the blueshift of the VDOS peak located around 2 THz in the $\varepsilon''(\nu)$ spectrum. The BP behaviors of the mentioned glucose polymers were compared and discussed with the $\alpha(\nu)/\nu^2$ spectra. There is no peak observed in the $\alpha(\nu)/\nu^2$ spectrum of paramylon because paramylon had a high degree of crystallinity. Cellulose, CM-starch, and paramylon ester show BP at 0.92, 1.16, and 0.50 THz, respectively. I compared those BPs to the BPs of glucose and starch that studied by previous studies. The result demonstrated that the hydrogen bond network might be the dominant factor of BP frequency in glucose and glucose polymer glasses. On the other hand, if there are no or few hydrogen bonds in the sample, for example, paramylon ester, the dominant factor of BP might be weak van der Waals force.

Figures

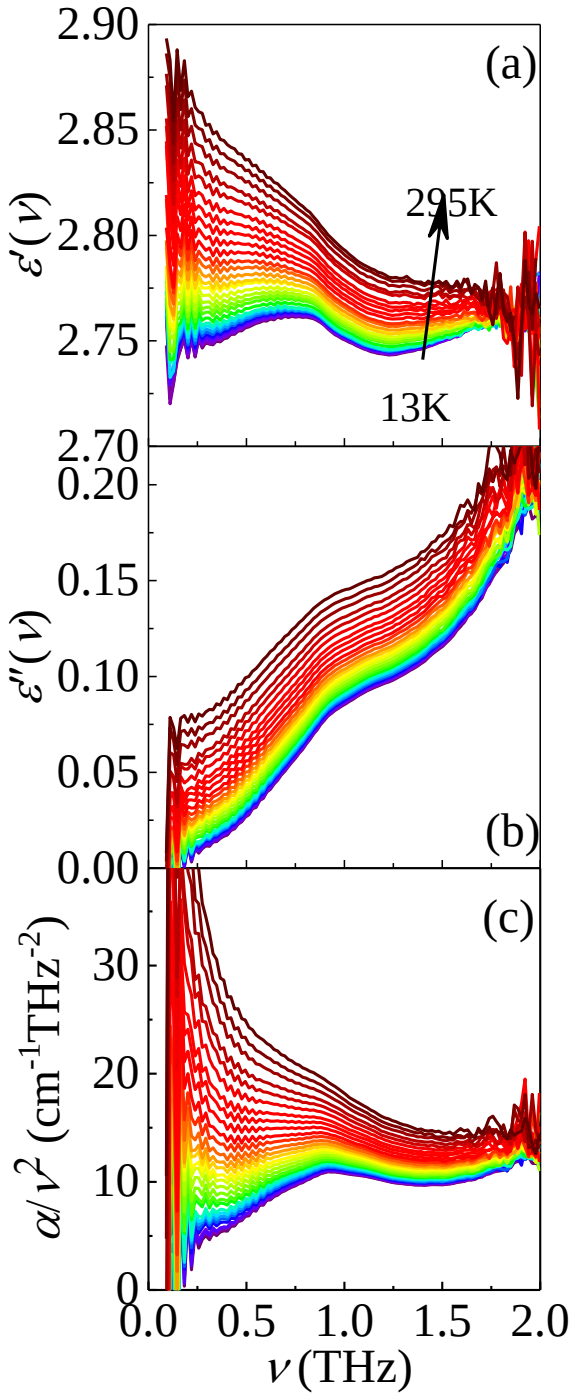

Figure 6-1 Temperature dependence of (a) real and (b) imaginary parts of complex dielectric constants and $\alpha(\nu)/\nu^2$ spectra for cellulose during heating from 13 K to 295 K. Data are plotted at intervals of 10 K above 20 K.

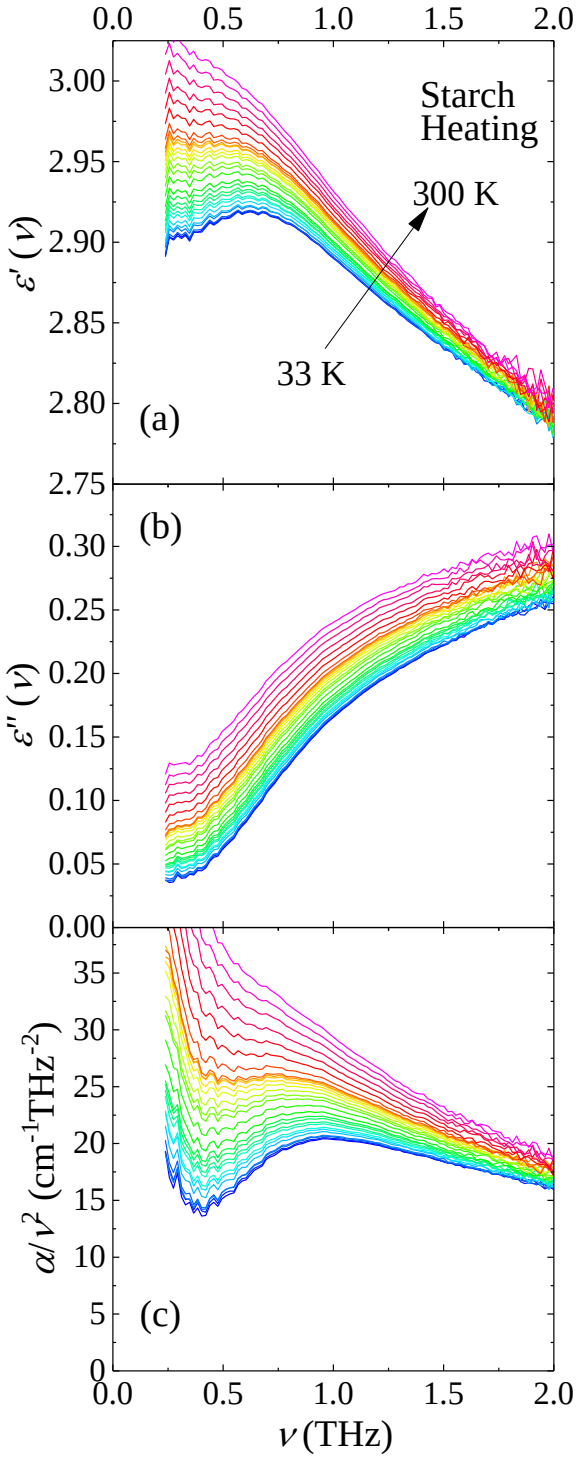

Figure 6-2 Temperature dependence of (a) real and (b) imaginary parts of complex dielectric constants and $\alpha(\nu)/\nu^2$ spectra for starch during heating from 33 K to 300 K. Data are plotted at intervals of 10 K above 40 K (Terao et al., 2018).

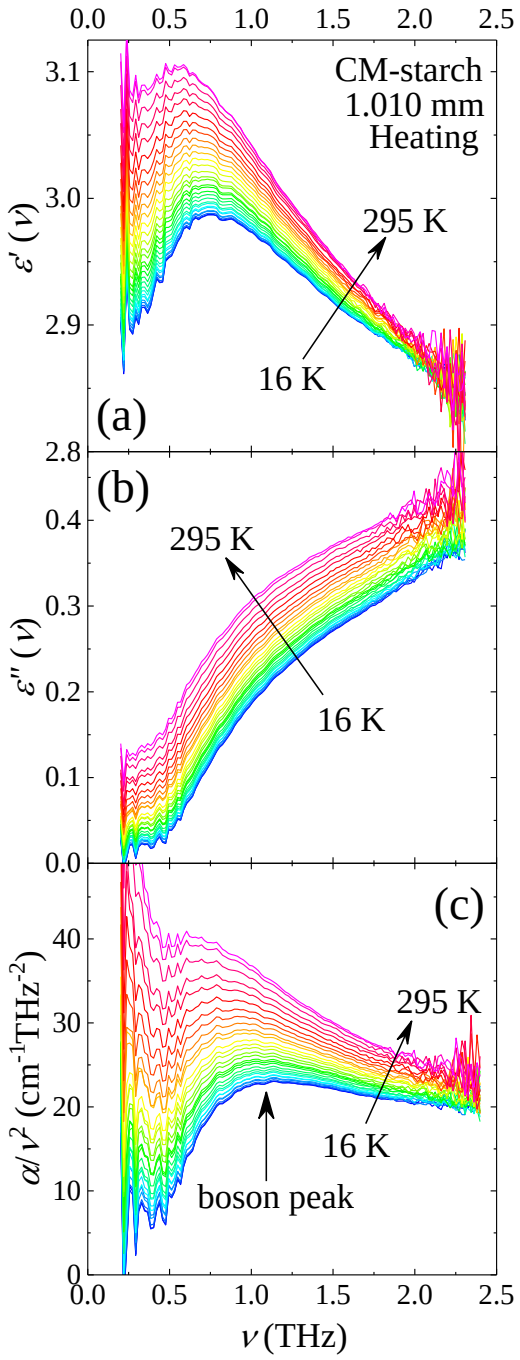

Figure 6-3 Temperature dependence of (a) the real $\varepsilon'(\nu)$ and (b) imaginary parts $\varepsilon''(\nu)$ of complex dielectric constants, and the $\alpha(\nu)/\nu^2$ spectrum of the CM-starch during the heating process from 16 K to 295 K. The data are plotted every 10 K above 20 K (Terao, Master's thesis, 2018).

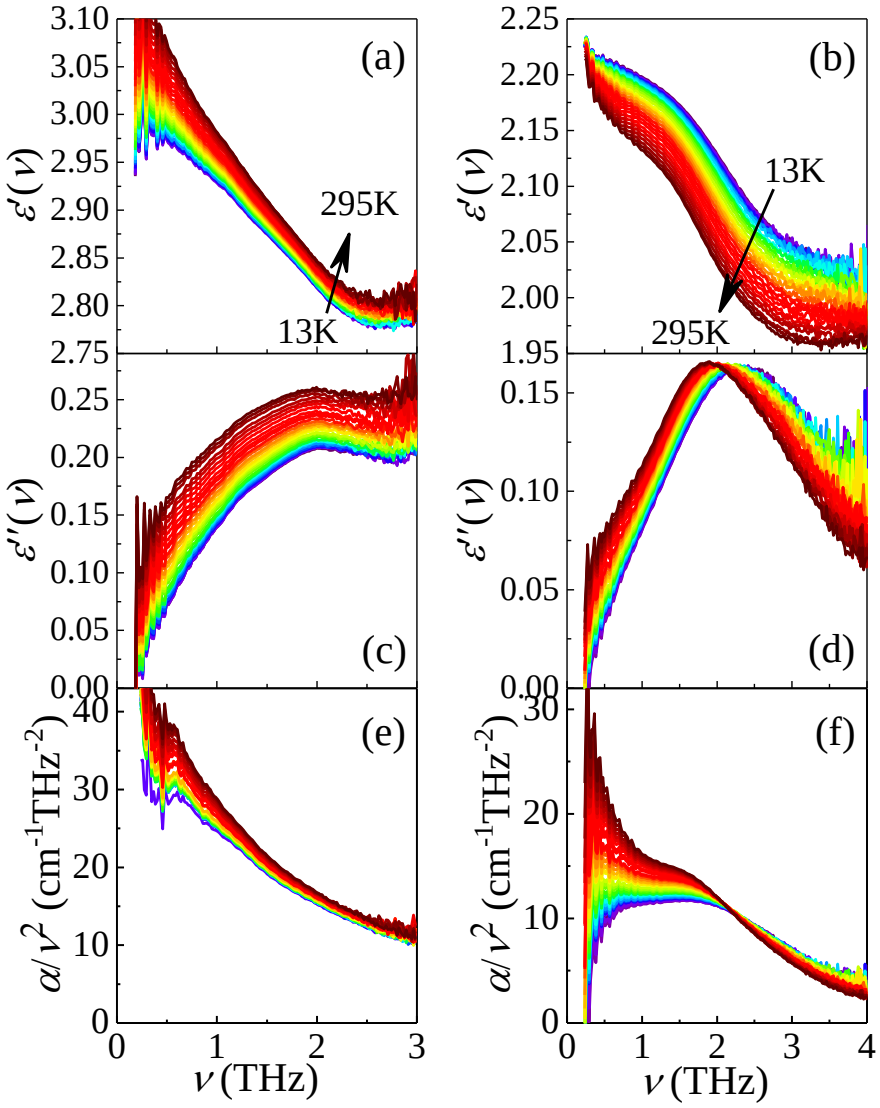

Figure 6-4 Temperature dependence of (a) the real $\varepsilon'(\nu)$ and (b) imaginary parts $\varepsilon''(\nu)$ of complex dielectric constants, and the $\alpha(\nu)/\nu^2$ spectrum of the paramylon and paramylon ester during the heating process from 13 K to 295 K. The data are plotted every 10 K above 20 K.

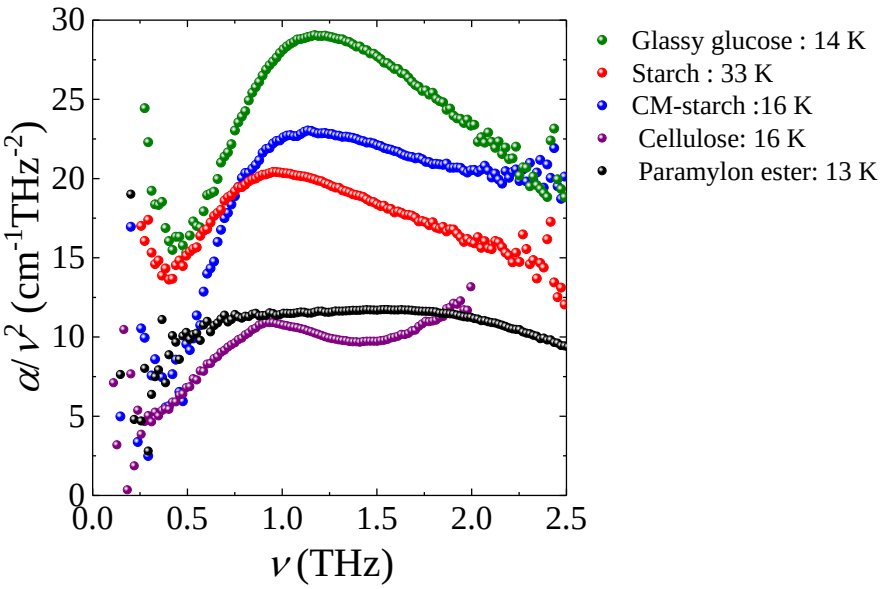

Figure 6-5 Comparison of $\alpha(\nu)/\nu^2$ spectra at the lowest temperature of CM-starch (blue dots), natural starch (red dots), and glassy glucose. The data of natural starch and glucose were obtained by the previous study (Terao et al., 2018; Kabeya et al.,2017).

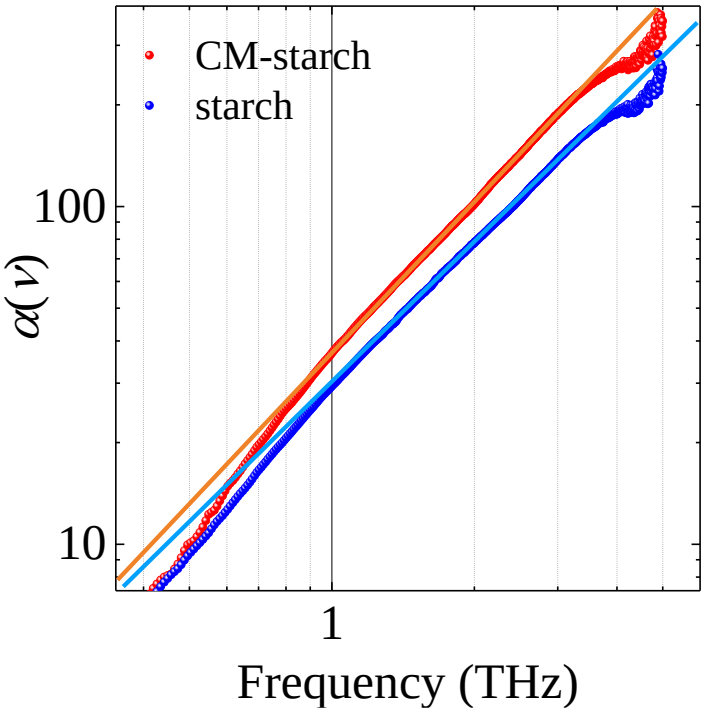

Figure 6-6 The log-log plot of the absorption coefficient of starch and CM-starch.

Tables

Table 6-1 The comparison of the frequencies and intensities of glucose polymers and esters.

Sample	Crystallinity (%)	ν_{BP} (THz)	Maximum intensity$_{(BP)}$ ($cm^{-1}THz^{-2}$)
Glucose	0	1.17	29.0
Cellulose	50.0	0.92	10.9
Starch	33.9	0.99	20.4
CM-starch	0	~1	23.0
Paramylon	~90%	--	--
Paramylon ester	~30%	~0.5	11.4

"~" indicting the value is approximated.

Table 6-2 The detailed of the categories of polymers.

Sample	ν_{BP} **(THz)**	Category	Determinant of ν_{BP}
Glucose, Glucose polymers	**~1**	Hydrogen bonded glass	Hydrogen bond network
Paramylon ester	**0.5**	Non-hydrogen bonded glass	Weak van der Waals force

Table 6-3 The detailed parameters of CM-starch and natural starch.

	v_{BP}	μ	d_f	D_f
CM-starch	1.16	1.5	1.33	2.17
Starch	0.99	1.4	1.33	2.38

Chapter 7 Conclusions

The high resolution, high sensitivity, and relatively simple detection of terahertz technology provide a new perspective for spectroscopy research. In addition, the rapid development of terahertz radiation generation and detection technology in recent years has provided a foundation for terahertz research. However, the terahertz spectroscopy analysis still lacks explanation. Decoding the structural information of molecules from specific resonance absorption THz spectra and associating the vibration patterns of substances with the structure and function of molecules is an essential topic in THz spectroscopy development.

In this work, the investigation of absorption properties and vibrational dynamics of glucose polymers were conducted, including cellulose, paramylons, and paramylon-esters have been focused on studying using Fourier-transform infrared-THz (FT-IR-THz) spectroscopy. The spectral characteristics of paramylon and paramylon ester were studied by comparing their absorption feature with those of glucose and cellulose. The qualitative analysis of paramylons with different molecular weight (MW) and the quantitative analysis of paramylon-esters with different degrees of substitution (DS) were conducted based on the spectral absorption characteristics of paramylon and paramylon ester. The temperature-dependence THz spectroscopy is also performed on cellulose, paramylon, paramylon ester, and CM-starch to investigate the origin of the boson peak and fraction dynamics. The complex dielectric constant observed below 2 THz frequency was analyzed, and the BP behaviors were discussed by comparing with those of glucose and starch. The main work of the paper is summarized as follows:

(1) The development of wave science and technology and its application in the field of biochemistry are reviewed. The electromagnetism, quantum mechanics, quantum chemistry, and semiconductor physics related to the science and technology of terahertz wave are expounded. The transmission terahertz time-domain spectroscopy and its related material parameters extraction method, sample preparation, and operation process of experimental instruments are introduced.

(2) The spectral characteristics of paramylon and paramylon ester at room temperature (0.3-8 THz) were studied by time-domain spectroscopy. We compared the results with the spectra of glucose and cellulose. The main reason is that their different crystal structures and the different amount of -OH groups, which both lead to the difference in lattice vibration mode and intermolecular hydrogen bonding. The paramylon has broad three absorption peaks at 4.0, 6.0, and 8.0 THz, while the paramylon ester shows similar broad

spectral features around 2.7 and 4.85 THz. Four paramylons with different molecular weights were compared with each other. They all showed absorption peaks at 4 and 5 THz, which can be regared as the special spectral features of paramylon. Last, the spectra of paramylon ester with different DS were analyzed. The linear relationship between the peak intensities and DS was found with reasonable accuracy. This result indicates that THz spectrosacopy is very sensitive to the structure and spatial arrangement of molecules and can identify the differences in similar structures. This study provides an efficient and non-damaging new detection method for food safety and biological detection.

(3) The BP behaviors of cellulose, starch, CM-starch, paramylon and paramylon ester were compared and discussed with the $\alpha(v)/v^2$ spectra. There is no peak observed in the $\alpha(v)/v^2$ spectrum of paramylon because paramylon had a high degree of crystallinity. Cellulose, CM-starch, and paramylon ester show BP at 0.92, 1.16, and 0.50 THz, respectively. The boson peak analysis revealed that the BP frequency for monomeric glucose nearly equals the corresponding values of glucose polymers. This is consistent with recent results of MD simulations for polymer glasses. The comparison of the BP frequencies of mentioned glucose polymers and glucose also demonstrated that the hydrogen bond network might be the dominant factor of BP frequency in glucose and glucose polymer glasses. On the other hand, for the non-hydrogen bonds in the sample, *i.e.*, paramylon ester, the dominant factor of BP might be weak van der Waals force.

In this work, the THz-TDS and FTIR were used to study the spectral properties of several polymers. The spectral features of paramylon and paramylon ester in the THz region were studies for the first time. The prediction mode of DS of paramylon ester were built according to the intensities of the peaks. The boson peak (BP) behaviors of the mentioned cellulose, CM-starch, paramylon and paramylon ester were compared and discussed with the α(v)/v2 spectra for the first time. The dominant factor of BP frequency were discussed according to the BP frequency. The results of this thesis provide effective experimental methods, and spectral analysis means for the study of other molecules and provides a basis for the application of the THz technology. The thesis also provides the evidents for the BP determinants for the glusoce polymers.

At present, the THz spectroscopy has made significant progress in experimental spectroscopy and theoretical simulation, especially in the field of biomolecules. However, compared with mature spectral technology, spectral research on bio-polymers and amorphous materials is still in its infancy, lacking more in-depth theoretical research and a large number of experimental spectral data. The additional effort should be made in the spectroscopy analysis.

List of publications

1. Zhong J.L., Mori T.,… ,& Kadowaki K. Microstructure and molecular-vibration analysis of Glucose polymers and ester via terahertz spectroscopy. Carbohydrate polymers (IF= 6.044), https://doi.org/10.1016/j.carbpol.2019.115789.

2. Zhong J.L., Mori T.,… ,& Kadowaki K. Terahertz Characteristic Absorption Spectra of Paramylon and Paramylon-Ester Compounds. Journal of Infrared, Millimeter, and Terahertz Waves (IF= 1.762), Under review.

3. Zhong J.L., Mori T.,… ,& Kadowaki K. Spectroscopic characterization at THz frequencies of glucose-based biomaterials: paramylon, paramylon-ester and cellulose. IRMMW-THz, 2019.

References

Agarwal, U. P., Ralph, S. A., Reiner, R. S., & Baez, C. (2018). New cellulose crystallinity estimation method that differentiates between organized and crystalline phases. *Carbohydrate Polymers*, 190, 262-270.

Angell, C. A. (1991). Relaxation in liquids, polymers and plastic crystals—strong/fragile patterns and problems. *Journal of Non-Crystalline Solids*, 131, 13-31.

Amaro, H. M., Guedes, A. C., & Malcata, F. X. (2011). Advances and perspectives in using microalgae to produce biodiesel. *Applied Energy*, 88(10), 3402-3410.

Auston, D. H., Cheung, K. P., & Smith, P. R. (1984). Picosecond photoconducting Hertzian dipoles. *Applied Physics Letters*, 45(3), 284-286.

Baldi, G., Giordano, V. M., Monaco, G., & Ruta, B. (2010). Sound attenuation at terahertz frequencies and the boson peak of vitreous silica. *Physical Review Letters*, *104*(19), 195501.

Barsanti, L., Passarelli, V., Evangelista, V., Frassanito, A. M., & Gualtieri, P. (2011). Chemistry, physico-chemistry and applications linked to biological activities of β-glucans. *Natural Product Reports*, 28(3), 457-466.

Bernier, M., Garet, F., & Coutaz, J. L. (2017). Determining the complex refractive index of materials in the far-infrared from terahertz time-domain data. *In Terahertz Spectroscopy-Cutting Edge Technology*. Intech-Open Science.

Binder, K., & Kob, W. (2011). *Glassy materials and disordered solids: An introduction to their statistical mechanics*. World scientific.

Buchenau, U., & Schober, H. R. (2008). An atomic mechanism for the boson peak in metallic glasses. *Philosophical Magazine*, 88(33-35), 3885-3900.

Brown, G. M., & Levy, H. A. (1979). α-D-Glucose: further refinement based on neutron-diffraction data. *Acta Crystallographica Section B: Structural Crystallography and Crystal Chemistry*, 35(3), 656-659.

Carini, Jr., G., Carini, G., Cosio, D., D'Angelo, G., & Rossi, F. (2016). Low temperature heat capacity of permanently densified SiO2 glasses. *Philosophical Magazine*, *96*(7-9), 761-773.

Chacón-Lee, T.L. & González-Mariño, G.E. (2010). Microalgae for "Healthy" Foods—Possibilities and Challenges. *Comprehensive Reviews in Food Science and Food Safety*, 9(6), s. 655-675.

Chisti, Y. (2007). Biodiesel from microalgae. *Biotechnology Advances*, 25(3), 294-306.

Cho, D. H., Ramanan, R., Heo, J., Shin, D. S., Oh, H. M., & Kim, H. S. (2016). Influence of limiting factors on biomass and lipid productivities of axenic Chlorella vulgaris in

photobioreactor under chemostat cultivation. *Bioresource Technology*, 211, 367-373.

Chuah, C. T., Sarko, A., Deslandes, Y., & Marchessault, R. H. (1983). Packing analysis of carbohydrates and polysaccharides. Part 14. Triple-helical crystalline structure of curdlan and paramylon hydrates. *Macromolecules*, *16*(8), 1375–1382.

Chumakov, A. I., Monaco, G., Monaco, A., Crichton, W. A., Bosak, A., Rüffer, R., Meyer, A., Kargl, F., Comez, L., Fioretto, D., Giefers, H., Roitsch, S., Wortmann, G., Manghnani, M. H., Hushur, A., Williams, Q., Balogh, J., Parliński, K., Jochym, P., & Piekarz, P. (2011). Equivalence of the boson peak in glasses to the transverse acoustic Van Hove singularity in crystals. *Physical Review Letters*, *106*(22), 225501.

Crupi, C., D'Angelo, G., Wanderlingh, U., Conti Nibali, V., & Vasi, C. (2010). Low frequency dynamics of lysozyme: A Raman scattering and low temperature specific heat study. *Journal of Spectroscopy*, *24*(3-4), 201-205.

Darzin, A., Pienkos, P. & Edye, L. (2010). Current status and potential for algal biofuels production. *IEA Bioenergy Task 39*, August 2010.

Das, P., Aziz, S. S., & Obbard, J. P. (2011). Two phase microalgae growth in the open system for enhanced lipid productivity. *Renewable Energy*, 36(9), 2524-2528.

Dewey, T. G. (1998). *Fractals in molecular biophysics*. Oxford University Press.

Dhillon et al. (2017). The 2017 terahertz science and technology roadmap. *Journal of Physics D: Applied Physics*, 50(4), 043001.

Dressel, M., & Grüner, G. (2002). *Electrodynamics of solids: optical properties of electrons in matter*.

Ellis, J. W., & Bath, J. (1940). Hydrogen bridging in cellulose as shown by infrared absorption spectra. *Journal of the American Chemical Society*, 62(10), 2859-2861.

Federici, J. F., Schulkin, B., Huang, F., Gary, D., Barat, R., Oliveira, F., & Zimdars, D. (2005). THz imaging and sensing for security applications—explosives, weapons and drugs. *Semiconductor Science and Technology*, 20(7), S266.

Federici, J., & Moeller, L. (2010). Review of terahertz and subterahertz wireless communications. *Journal of Applied Physics*, 107(11), 6.

Fischer, B., Hoffmann, M., Helm, H., Modjesch, G., & Jepsen, P. U. (2005). Chemical recognition in terahertz time-domain spectroscopy and imaging. *Semiconductor Science and Technology*, *20*(7), S246.

Fitzgerald, A. J., Cole, B. E., & Taday, P. F. (2005). Nondestructive analysis of tablet coating thicknesses using terahertz pulsed imaging. *Journal of Pharmaceutical Sciences*, *94*(1), 177–183.

Formighieri, C., Franck, F., & Bassi, R. (2012). Regulation of the pigment optical density of an algal cell: filling the gap between photosynthetic productivity in the laboratory and in mass culture. *Journal of Biotechnology*, 162(1), 115-123.

Galeener, F. L. & Sen, P. N. (1978). Theory for the first-order vibrational spectra of disordered solids. *Physical Review B*, *17*, 1928–1933.

Gan, H., Enomoto, Y., Kabe, T., Ishii, D., Hikima, T., Takata, M., & Iwata, T. (2017). Synthesis, properties and molecular conformation of paramylon ester derivatives. *Polymer Degradation and Stability*, *145*, 142–149.

Gan, H., Kabe, T., Kimura, S., Hikima, T., Takata, M., & Iwata, T. (2019). Crystal structures and crystalline elastic modulus of paramylon esters. *Polymer*, 172, 7-12.

Gardner, K. H., & Blackwell, J. (1974). The structure of native cellulose. *Biopolymers: Original Research on Biomolecules*, 13(10), 1975-2001.

Ge, M., Liu, G., Ma, S., & Wang, W. (2009). Polymorphic forms of furosemide characterized by THz time domain spectroscopy. *Bulletin of the Korean Chemical Society*, *30*(10), 2265-2268.

Giuntoli, A. & Leporini, D. (2018). Boson peak decouples from elasticity in glasses with low connectivity. *Physical Review Letters*, *121*(18), 185502.

Globus, T. R., Woolard, D. L., Khromova, T., Crowe, T. W., Bykhovskaia, M., Gelmont, B. L., ... & Samuels, A. C. (2003). THz-spectroscopy of biological molecules. *Journal of Biological Physics*, 29(2-3), 89-100.

Guiry, M. D. (2012). How many species of algae are there?. *Journal of Phycology*, 48(5), 1057-1063.

Gonçalves, A. L., Simões, M., & Pires, J. C. M. (2014). The effect of light supply on microalgal growth, CO2 uptake and nutrient removal from wastewater. *Energy Conversion and Management*, 85, 530-536.

Gottlieb, J. (1850). Ueber eine neue, mit Stärkmehl isomere Substanz. *Justus Liebigs Annalen der Chemie*, 75(1), 51-61.

Gross, R., Alff, L., Beck, A., Froehlich, O. M., Koelle, D., & Marx, A. (1997). Physics and technology of high temperature superconducting Josephson junctions. *IEEE transactions on Applied Superconductivity*, 7(2), 2929-2935.

Hadjiloucas, S., Walker, G. C., Bowen, J. W., Becerra, V. M., Zafiropoulos, A., & Galvão, R. K. H. (2009). High signal to noise ratio THz spectroscopy with ASOPS and signal processing schemes for mapping and controlling molecular and bulk relaxation processes. *In Journal of Physics: Conference Series* (Vol. 183, No. 1, p. 012003). IOP Publishing.

Hafez, H. A., Chai, X., Ibrahim, A., Mondal, S., Férachou, D., Ropagnol, X., & Ozaki, T. (2016). Intense terahertz radiation and their applications. *Journal of Optics*, 18(9), 093004.

Hargreaves, J. W., & Whitton, B. A. (1976). Effect of pH on growth of acid stream algae. *British Phycological Journal*, 11(3), 215-223.

Hashimoto, Y., Mori, T., & Kojima, S. (2016). Broadband terahertz time-domain spectroscopy and low-frequency Raman scattering of glassy polymers: Boson peak of PMMA. *Molecular Crystals and Liquid Crystals*, 629(1), 258-263.

Hédoux, A., Paccou, L., Guinet, Y., Willart, J. F., & Descamps, M. (2009). Using the low-frequency Raman spectroscopy to analyze the crystallization of amorphous indomethacin. *European Journal of Pharmaceutical Sciences*, *38*(2), 156-164.

Hizukuri, S., Takeda, Y., Yasuda, M., & Suzuki, A. (1981). Multi-branched nature of amylose and the action of debranching enzymes. *Carbohydrate Research*, 94(2), 205-213.

Ho, S. H., Chen, W. M., & Chang, J. S. (2010). Scenedesmus obliquus CNW-N as a potential candidate for CO2 mitigation and biodiesel production. *Bioresource Technology*, 101(22), 8725-8730.

Hoshina, H., Morisawa, Y., Sato, H., Kamiya, A., Noda, I., Ozaki, Y., & Otani, C. (2010). Higher order conformation of poly (3-hydroxyalkanoates) studied by terahertz time-domain spectroscopy. *Applied Physics Letters*, *96*(10), 101904.

Hoshina, H., Ishii, S., Yamamoto, S., Morisawa, Y., Sato, H., Uchiyama, T., Ozaki, Y., & Otani, C. (2013). Terahertz spectroscopy in polymer research: assignment of intermolecular vibrational modes and structural characterization of poly (3-hydroxybutyrate). *IEEE Transactions on Terahertz Science and Technology*, *3*(3), 248–258.

Huang, S. W., Granados, E., Huang, W. R., Hong, K. H., Zapata, L. E., & Kärtner, F. X. (2013). High conversion efficiency, high energy terahertz pulses by optical rectification in cryogenically cooled lithium niobate. *Optics Letters*, 38(5), 796-798.

Imberty, A., Buléon, A., Tran, V., & Péerez, S. (1991). Recent advances in knowledge of starch structure. *Starch-Stärke*, 43(10), 375-384.

Inwongwan, S., Kruger, N. J., Ratcliffe, R. G., & O'Neill, E. C. (2019). Euglena Central Metabolic Pathways and Their Subcellular Locations. *Metabolites*, 9(6), 115.

Ishikawa, A., Okano, T., & Sugiyama, J. (1997). Fine structure and tensile properties of ramie fibres in the crystalline form of cellulose I, II, IIII and IVI. *Polymer*, *38*(2), 463-468.

Jane, J. L., Kasemsuwan, T., Leas, S., Zobel, H., & Robyt, J. F. (1994). Anthology of starch granule morphology by scanning electron microscopy. *Starch-Stärke*, 46(4), 121-129.

Jepsen, P. U., Cooke, D. G., & Koch, M. (2011). Terahertz spectroscopy and imaging–Modern techniques and applications. *Laser & Photonics Reviews*, 5(1), 124-166.

Kabeya, M., Mori, T., Fujii, Y., Koreeda, A., Lee, B. W., Ko, J. H., & Kojima, S. (2016). Boson peak dynamics of glassy glucose studied by integrated terahertz-band spectroscopy. *Physical Review B*, *94*(22), 224204.

Kaczmarska, K., Grabowska, B., Spychaj, T., Zdanowicz, M., Sitarz, M., Bobrowski, A., & Cukrowicz, S. (2018). Effect of microwave treatment on structure of binders based on sodium carboxymethyl starch: FT-IR, FT-Raman and XRD investigations. *Spectrochimica Acta Part A: Molecular and Biomolecular Spectroscopy*, 199, 387-393.

Kadowaki, K., Yamaguchi, H., Kawamata, K., Yamamoto, T., Minami, H., Kakeya, I., ... & Gray, K. E. (2008). Direct observation of terahertz electromagnetic waves emitted from intrinsic Josephson junctions in single crystalline Bi2Sr2CaCu2O8+ δ. *Physica C: Superconductivity and its Applications*, 468(7-10), 634-639.

Kawahara, Y. (2014). (1→ 3)-β-d-Glucan nanofibers from paramylon via electrospinning. *Carbohydrate Polymers*, 112, 73-76.

Khan, M. I., Shin, J. H., & Kim, J. D. (2018). The promising future of microalgae: current status, challenges, and optimization of a sustainable and renewable industry for biofuels, feed, and other products. *Microbial Cell Factories*, 17(1), 36.

Kiss, J. Z., Roberts, E. M., Brown, R. M., & Triemer, R. E. (1988). X-ray and dissolution studies of paramylon storage granules from Euglena. *Protoplasma*, 146(2-3), 150-156.

Kittel, C. (1976). *Introduction to solid state physics* (Vol. 8), Chapter 3 CRYSTAL BINDING. New York: Wiley.

Kleine-Ostmann, T., & Nagatsuma, T. (2011). A review on terahertz communications research. *Journal of Infrared, Millimeter, and Terahertz Waves*, 32(2), 143-171.

Kojima, S. (1993). Low-frequency Raman investigation of the liquid-glass transition in glycerol. *Physical Review B*, *47*(5), 2924.

Kojima, S., Shibata, T., Igawa, H., & Mori, T. (2014). Broadband terahertz time-domain spectroscopy: crystalline and glassy drug materials. *In IOP Conference Series: Materials Science and Engineering*, *54*(1), 012001.

Köhler, R., Tredicucci, A., Beltram, F., Beere, H. E., Linfield, E. H., & Davies, A. G., et al. (2002). *Terahertz semiconductor-heterostructure laser*. , 417(6885), 156-159.

Kono, S. , Tani, M. , & Sakai, K. . (2001). Ultrabroadband photoconductive detection: comparison with free-space electro-optic sampling. *Applied Physics Letters*, 79(7), 898.

Koroteeva, D. A., Kiseleva, V. I., Krivandin, A. V., Shatalova, O. V., Błaszczak, W., Bertoft, E., ... & Yuryev, V. P. (2007). Structural and thermodynamic properties of rice starches with different genetic background: Part 2. Defectiveness of different supramolecular structures in starch granules. *International Journal of Biological Macromolecules*, 41(5), 534-547.

Korter, T. M., Balu, R., Campbell, M. B., Beard, M. C., Gregurick, S. K., & Heilweil, E. J. (2006). Terahertz spectroscopy of solid serine and cysteine. *Chemical Physics Letters*, 418(1-3), 65-70.

Kouadri, I., & Satha, H. (2018). Extraction and characterization of cellulose and cellulose nanofibers from Citrullus colocynthis seeds. *Industrial Crops and Products*, 124, 787-796.

Kreger, D. R., & Meeuse, B. J. (1952). X-ray diagrams of Euglena-paramylon, of the acid-insoluble glucan of yeast cell walls and of laminarin. *Biochimica et Biophysica Acta*, 9(6), 699.

Kurabayashi, T., Shuhama, H., Yodokawa, S., & Kosaka, S. (2017). Identification of cellulosic fibers and determination of their blend ratio using terahertz spectroscopy. *Infrared Physics and Technology*, *80*, 153–157.

Kutteruf, M. R., Brown, C. M., Iwaki, L. K., Campbell, M. B., Korter, T. M., & Heilweil, E. J. (2003). Terahertz spectroscopy of short-chain polypeptides. *Chemical Physics Letters*, 375(3-4), 337-343.

Lee, K., Jeoung, K., Lee, D. K., Ji, Y. B., Seo, M., Huh, Y. M., ... & Oh, S. J. (2018). Study of molecular structure change of d- and l-glucose by proton irradiation using terahertz spectroscopy. *Infrared Physics & Technology*, 93, 154-157.

Lee, R. E. (2018). *Phycology*. Cambridge University Press.

Lee, S. J., Choi, W. S., Park, G. H., Kim, T. H., Oh, C., Heo, S. J., & Kang, D. H. (2018). Flocculation Effect of Alkaline Electrolyzed Water (AEW) on Harvesting of Marine Microalga Tetraselmis sp. *Journal of Microbiology and Biotechnology*, 28(3), 432-438.

Lee, Y. S. (2009). *Principles of terahertz science and technology* (Vol. 170). Springer Science & Business Media.

Liang, C. Y., & Marchessault, R. H. (1959). Infrared spectra of crystalline polysaccharides. I. Hydrogen bonds in native celluloses. *Journal of Polymer Science*, 37(132), 385-395.

Low, T., & Avouris, P. (2014). Graphene plasmonics for terahertz to mid-infrared applications. *ACS Nano*, 8(2), 1086-1101.

Marchessault, R. H. & Deslandes, Y. (1979). Fine structure of (1→3)-β-D-glucans: curdlan and paramylon. *Carbohydrate Research, 75*, 231–242.

Markou, G., Vandamme, D., & Muylaert, K. (2014). Microalgal and cyanobacterial cultivation: the supply of nutrients. *Water Research*, 65, 186-202.

Marruzzo, A., Schirmacher, W., Fratalocchi, A., & Ruocco, G. (2013). Heterogeneous shear elasticity of glasses: the origin of the boson peak. *Scientific Reports*, 3, 1407.

Matic, A., Masciovecchio, C., Engberg, D., Monaco, G., Börjesson, L., Santucci, S. C., & Verbeni, R. (2004). Crystal-like nature of acoustic excitations in glassy ethanol. *Physical Review Letters*, *93*(14), 145502.

松田裕. (2010). Structural relaxation and vibrational dynamics of alkali borate glasses (Doctoral dissertation, 筑波大学).

Melis, A. (2009). Solar energy conversion efficiencies in photosynthesis: minimizing the chlorophyll antennae to maximize efficiency. *Plant Science*, 177(4), 272-280.

Milkus, R., Ness, C., Palyulin, V. V., Weber, J., Lapkin, A., & Zaccone, A. (2018). Interpretation of the vibrational spectra of glassy polymers using coarse-grained simulations. *Macromolecules*, *51*(4), 1559–1572.

Mittleman, D. M., Jacobsen, R. H., Neelamani, R., Baraniuk, R. G., & Nuss, M. C. (1998). Gas sensing using terahertz time-domain spectroscopy. *Applied Physics B*, 67(3), 379-390.

Mori, T., Jiang, Y., Fujii, Y., Kitani, S., Mizuno, H., Koreeda, A., ... & Kojima, S. (2019). Detection of boson peak and fractal dynamics of disordered system using terahertz spectroscopy. arXiv preprint arXiv:1910.04400.

De Morais, M. G., & Costa, J. A. V. (2007). Biofixation of carbon dioxide by Spirulina sp. and Scenedesmus obliquus cultivated in a three-stage serial tubular photobioreactor. *Journal of Biotechnology*, 129(3), 439-445.

Nakajima, S., Shiraga, K., Suzuki, T., Kondo, N., & Ogawa, Y. (2019). Quantification of starch content in germinating mung bean seedlings by terahertz spectroscopy. *Food Chemistry*, 294, 203-208.

Ngai, K. L. (2011). *Relaxation and Diffusion in Complex Systems* (pp. 64-65). New York: Springer Science & Business Media (Chapter 2).

Odlare, M., Nehrenheim, E., Ribé, V., Thorin, E., Gavare, M., & Grube, M. (2011). Cultivation of algae with indigenous species–potentials for regional biofuel production. *Applied Energy*, 88(10), 3280-3285.

O"Shea, & P., G. . (2001). Free-electron lasers: status and applications. *Science*, 292(5523), 1853-1858.

Ozyuzer, L., Koshelev, A. E., Kurter, C., Gopalsami, N., Li, Q., Tachiki, M., ... & Tachiki, T. (2007). Emission of coherent THz radiation from superconductors. *Science*, 318(5854), 1291-1293.

Parshin, D. A., Schober, H. R., & Gurevich, V. L. (2007). Vibrational instability, two-level systems, and the boson peak in glasses. *Physical Review B*, 76(6), 064206.

Pawar, A. Y., Sonawane, D. D., Erande, K. B., & Derle, D. V. (2013). Terahertz technology and its applications. *Drug Invention Today*, 5(2), 157-163.

Pearson, F. G., Marchessault, R. H., & Liang, C. Y. (1960). Infrared spectra of crystalline polysaccharides. V. Chitin. *Journal of Polymer Science*, 43(141), 101-116.

Peccianti, M., Fastampa, R., Conte, A. M., Pulci, O., Violante, C., Łojewska, J., Clerici, M., Morandotti, R., & Missori, M. (2017). Terahertz absorption by cellulose: Application to ancient paper artifacts. *Physical Review Applied*, *7*(6), 064019.

Penttilä, P. (2013). Structural characterization of cellulosic materials using x-ray and neutron scattering. Dissertation, University of Helsinki Helsinki, Finland.

Peydecastaing, J., Vaca-Garcia, C., & Borredon, E. (2011). Bi-acylation of cellulose: determining the relative reactivities of the acetyl and fatty-acyl moieties. *Cellulose*, 18(4), 1015-1021.

Pickwell, E., & Wallace, V. P. (2006). Biomedical applications of terahertz technology. *Journal of Physics D: Applied Physics*, 39(17), R301.

Rawat, I., Kumar, R. R., Mutanda, T., & Bux, F. (2011). Dual role of microalgae: phycoremediation of domestic wastewater and biomass production for sustainable biofuels production. *Applied Energy*, 88(10), 3411-3424.

Redwood, M. D., Dhillon, R., Orozco, R. L., Zhang, X., Binks, D. J., Dickinson, M., & Macaskie, L. E. (2012). Enhanced photosynthetic output via dichroic beam-sharing. *Biotechnology Letters*, 34(12), 2229-2234.

Rosati, G., Verni, F., Barsanti, L., Passarelli, V., & Gualtieri, P. (1991). Ultrastructure of the apical zone of Euglena gracilis: photoreceptors and motor apparatus. *Electron Microscopy Reviews*, 4(2), 319-342.

Roth, C., Peppel, T., Fumino, K., Köckerling, M., & Ludwig, R. (2010). The importance of hydrogen bonds for the structure of ionic liquids: single-crystal X-ray diffraction and transmission and attenuated total reflection spectroscopy in the terahertz region. *Angewandte Chemie International Edition*, 49(52), 10221-10224.

Rungsawang, R., Ueno, Y., Tomita, I., & Ajito, K. (2006). Angle-dependent terahertz time-domain spectroscopy of amino acid single crystals. *The Journal of Physical Chemistry B*, *110*(42), 21259-21263.

Ruzicka, B., Scopigno, T., Caponi, S., Fontana, A., Pilla, O., Giura, P., Monaco, G., Pontecorvo, E., Ruocco, G., & Sette, F. (2004). Evidence of anomalous dispersion of the generalized sound velocity in glasses. *Physical Review B*, *69*(10), 100201.

Saikan, S., Kishida, T., Kanematsu, Y., Aota, H., Harada, A., & Kamachi, M. (1990). Polymer dependence of boson peak frequency studied by hole burning and Raman spectroscopies. *Chemical Physics Letters*, *166*(4), 358–362.

Saito, S., Inerbaev, T. M., Mizuseki, H., Igarashi, N., Note, R., & Kawazoe, Y. (2006). First principles calculation of terahertz vibrational modes of a disaccharide monohydrate crystal of lactose. *Japanese Journal of Applied Physics*, *45*(11L), L1156.

Schaechter M (2012): *Eukaryotic microbes*. In Eukaryotic microbiology 59 (6), 654. DOI: 10.1111/j.1550-7408.2012.00637.x

Sevilla, M., & Fuertes, A. B. (2009). Chemical and structural properties of carbonaceous products obtained by hydrothermal carbonization of saccharides. *Chemistry-A European Journal*, 15(16), 4195-4203.

Shen, Y. C. , Upadhya, P. C. , Beere, H. E. , Linfield, E. H. , Davies, A. G. , & Gregory, I. S. , et al. (2004). Generation and detection of ultrabroadband terahertz radiation using photoconductive emitters and receivers. *Applied Physics Letters*, 85(2), 164.

Shibakami, M., Sohma, M., & Hayashi, M. (2012). Fabrication of doughnut-shaped particles from spheroidal paramylon granules of Euglena gracilis using acetylation reaction. *Carbohydrate Polymers*, 87(1), 452-456.

Shibata, T., Mori, T., & Kojima, S. (2015). Low-frequency vibrational properties of crystalline and glassy indomethacin probed by terahertz time-domain spectroscopy and low-frequency Raman scattering. *Spectrochimica Acta Part A: Molecular and Biomolecular Spectroscopy*, *150*, 207–211.

Shintani, H., & Tanaka, H. (2008). Universal link between the boson peak and transverse phonons in glass. *Nature Materials*, 7(11), 870.

柴田知彦.（2015). 薬剤インドメタシンの広帯域分光（Master's dissertation, 筑波大学).

Sirtori, C. (2002). Applied physics: Bridge for the terahertz gap. *Nature*, 417(6885), 132.

Singh, R. N., & Sharma, S. (2012). Development of suitable photobioreactor for algae production–A review. *Renewable and Sustainable Energy Reviews*, 16(4), 2347-2353.

Singh, A. , Pal, S. , Surdi, H. , Prabhu, S. S. , Mathimalar, S. , & Nanal, V. , et al. (2015). Carbon irradiated semi insulating gaas for photoconductive terahertz pulse detection. *Optics Express*, 23(5), 6656.

Song, C., Fan, W. H., Ding, L., Chen, X., Chen, Z. Y., & Wang, K. (2018). Terahertz and infrared characteristic absorption spectra of aqueous glucose and fructose

solutions. *Scientific Reports*, 8(1), 8964.

Spolaore, P., Joannis-Cassan, C., Duran, E., Isambert, A. (2006). Commercial applications of microalgae. *Journal of Bioscience and Bioengineering*, 101:87–96.

Surovtsev, N. V. & Sokolov, A. P. (2002). Frequency behavior of Raman coupling coefficient in glasses. *Physical Review B, 66*(5), 054205.

Taday, P. F. (2003a). Applications of terahertz spectroscopy to pharmaceutical sciences. *Philosophical Transactions of the Royal Society of London. Series A: Mathematical, Physical and Engineering Sciences*, *362*(1815), 351–364.

Taday, P. F., Bradley, I. V., Arnone, D. D., & Pepper, M. (2003b). Using terahertz pulse spectroscopy to study the crystalline structure of a drug: A case study of the polymorphs of ranitidine hydrochloride. *Journal of Pharmaceutical Sciences*, *92*(4), 831–838.

Takahashi, M. (2014). Terahertz vibrations and hydrogen-bonded networks in crystals. *Crystals*, *4*(2), 74-103.

Takahashi, M., Okamura, N., Fan, X., Shirakawa, H., & Minamide, H. (2017). Temperature dependence in the terahertz spectrum of nicotinamide: anharmonicity and hydrogen-bonded network. *The Journal of Physical Chemistry A*, 121(13), 2558-2564.

Tani, M. , Hirota, Y. , Que, C. T. , Tanaka, S. , Hattori, R. , & Yamaguchi, M. , et al. (2006). Novel terahertz photoconductive antennas. *International Journal of Infrared and Millimeter Waves*, 27(4), 531-546.

Taraskin, S. N., Simdyankin, S. I., Elliott, S. R., Neilson, J. R., & Lo, T. (2006). Universal features of terahertz absorption in disordered materials. *Physical Review Letters*, *97*(5), 055504.

Terao, W., Mori, T., Fujii, Y., Koreeda, A., Kabeya, M., & Kojima, S. (2018). Boson peak dynamics of natural polymer starch investigated by terahertz time-domain spectroscopy and low-frequency Raman scattering. *Spectrochimica Acta Part A: Molecular and Biomolecular Spectroscopy*, *192*, 446–450.

寺尾　和香奈, デンプンおよびデンプングリコール酸ナトリウムのテラヘルツ分光研究, Master's thesis, 2019.

Tomoshige, N., Mizuno, H., Mori, T., Kim, K., & Matubayasi, N. (2019). Boson peak, elasticity, and glass transition temperature in polymer glasses: Effects of rigidity of chain bending. *Scientific Reports*, *9*, 19514.

Upadhya, P. C., Shen, Y. C., Davies, A. G., & Linfield, E. H. (2003). Terahertz time-domain spectroscopy of glucose and uric acid. *Journal of Biological Physics*, 29(2-3), 117-121.

Upadhya, P. C., Shen, Y. C., Davies, A. G., & Linfield, E. H. (2004). Far-infrared vibrational modes of polycrystalline saccharides. *Vibrational Spectroscopy*, 35(1-2), 139-143.

Van der Merwe, L. (2007). UDP-glucose: β-(1-3)-glucan (paramylon) synthase from Euglena gracilis (Doctoral dissertation, Stellenbosch: University of Stellenbosch).

Vicario, C., Ovchinnikov, A. V., Ashitkov, S. I., Agranat, M. B., Fortov, V. E., & Hauri, C. P. (2014). Generation of 0.9-mJ THz pulses in DSTMS pumped by a Cr: Mg 2 SiO 4 laser. *Optics Letters*, 39(23), 6632-6635.

Vieira, F. S., & Pasquini, C. (2014). Determination of cellulose crystallinity by terahertz-time domain spectroscopy. *Analytical Chemistry*, *86*(8), 3780-3786.

Violini, N., Orecchini, A., Paciaroni, A., Petrillo, C., & Sacchetti, F. (2012). Neutron scattering investigation of high-frequency dynamics in glassy glucose. *Physical Review B*, *85*(13), 134204.

Vitiello, M. S. , Scalari, G. , Williams, B. , & Natale, P. D. . (2015). Quantum cascade lasers: 20 years of challenges. *Optics Express*, 23(4).

Wang, W., Sun, P., Liu, W., & Xie, Y. (2016, November). Vibrational spectral investigation of anhydrous glucose in the terahertz range. *In Infrared, Millimeter-Wave, and Terahertz Technologies IV* (Vol. 10030, p. 1003026). International Society for Optics and Photonics.

Walther, M., Fischer, B. M., & Jepsen, P. U. (2003). Noncovalent intermolecular forces in polycrystalline and amorphous saccharides in the far infrared. *Chemical Physics*, 288(2-3), 261-268.

Walther, M. , Fischer, B. M. , Ortner, A. , Bitzer, A. , Thoman, A. , & Helm, H. . (2010). Chemical sensing and imaging with pulsed terahertz radiation. *Analytical and Bioanalytical Chemistry*, 397(3), 1009-1017.

Williams, B. S. (2007). Terahertz quantum-cascade lasers. *Nature Photonics*, 1(9), 517.

Zhang, J. , Hong, Y. , Braunstein, S. L. , & Shore, K. A. (2004). Terahertz pulse generation and detection with lt-gaas photoconductive antenna. *IEE Proceedings-Optoelectronics*, 151(2), 98-0.

Zeiler, K. G., Heacox, D. A., Toon, S. T., Kadam, K. L., & Brown, L. M. (1995). The use of microalgae for assimilation and utilization of carbon dioxide from fossil fuel-fired power plant flue gas. *Energy Conversion and Management*, 36(6-9), 707-712.

Zheng, Z. P., Fan, W. H., Liang, Y. Q., & Yan, H. (2012). Application of terahertz spectroscopy and molecular modeling in isomers investigation: Glucose and fructose. *Optics Communications*, 285(7), 1868-1871.

Zheng, Z. P., Fan, W. H., Li, H., & Tang, J. (2014). Terahertz spectral investigation of

anhydrous and monohydrated glucose using terahertz spectroscopy and solid-state theory. *Journal of Molecular Spectroscopy*, 296, 9-13.

Zhong, J., Mori, T., Fujii, Y., Kashiwagi, T., Terao, W., Yamashiro, M., ... & Ito, J. (2020). Molecular vibration and Boson peak analysis of glucose polymers and ester via terahertz spectroscopy. *Carbohydrate Polymers*, 232, 115789.